https://lib.uliege.be https://matheo.uliege.be

Travail de Fin d'Etudes : Optical and electrical properties of metallic nanostructures as electrode material for wide bandgap semiconducting junctions

Auteur : Halbach, Chloé
Promoteur(s) : Nguyen, Ngoc Duy; Vanderheyden, Benoit
Faculté : Faculté des Sciences appliquées
Diplôme : Master en ingénieur civil physicien, à finalité approfondie
Année académique : 2019-2020
URI/URL : http://hdl.handle.net/2268.2/9018

Avertissement à l'attention des usagers :

Tous les documents placés en accès ouvert sur le site le site MatheO sont protégés par le droit d'auteur. Conformément aux principes énoncés par la "Budapest Open Access Initiative"(BOAI, 2002), l'utilisateur du site peut lire, télécharger, copier, transmettre, imprimer, chercher ou faire un lien vers le texte intégral de ces documents, les disséquer pour les indexer, s'en servir de données pour un logiciel, ou s'en servir à toute autre fin légale (ou prévue par la réglementation relative au droit d'auteur). Toute utilisation du document à des fins commerciales est strictement interdite.

Par ailleurs, l'utilisateur s'engage à respecter les droits moraux de l'auteur, principalement le droit à l'intégrité de l'oeuvre et le droit de paternité et ce dans toute utilisation que l'utilisateur entreprend. Ainsi, à titre d'exemple, lorsqu'il reproduira un document par extrait ou dans son intégralité, l'utilisateur citera de manière complète les sources telles que mentionnées ci-dessus. Toute utilisation non explicitement autorisée ci-avant (telle que par exemple, la modification du document ou son résumé) nécessite l'autorisation préalable et expresse des auteurs ou de leurs ayants droit.

MASTER THESIS

Optical and Electrical Properties of Metallic Nanostructures as Electrode Material for Wide Band Gap Semiconducting Junctions

---

AUTHOR: Chloé HALBACH
ACADEMIC ADVISOR: Ngoc Duy NGUYEN
ACADEMIC CO-ADVISOR: Benoît VANDERHEYDEN

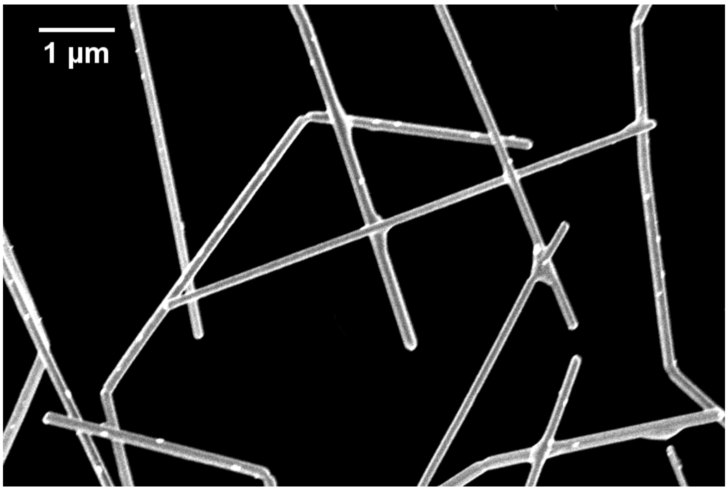

MASTER THESIS PRESENTED IN PARTIAL FULFILMENT OF THE REQUIREMENTS FOR THE MASTER OF SCIENCE DEGREE IN ENGINEERING PHYSICS

ACADEMIC YEAR 2019 - 2020

FACULTY OF APPLIED SCIENCES - UNIVERSITY OF LIÈGE

“Measure what can be measured,
and make measureable what cannot be measured.”

Galileo GALILEI

Acknowledgements

This year spent at the SPIN Lab allowed me to meet unforgettable people. Each of them contributed to this master thesis with their advice, their scientific knowledge, their technical skills, and their friendship.

First of all, I would like to express my deepest appreciation to my supervisor Ngoc Duy Nguyen for his valuable advice, unwavering guidance, and profound belief in my work. I am also grateful to my co-supervisor Benoît Vanderheyden for his constructive criticism.

I would like to thank the other members of the jury, Philippe Vanderbemden, Jean-Yves Raty, and Jean-Michel Redouté, for accepting to review this manuscript.

Many thanks to all the people from the SPIN and EPNM research groups for their friendliness and for being always available for discussions. In particular, I would like to extend my sincere thanks to Sunil Kumar Channam for his assistance and advice on the spin coating of silver nanowire networks and for the numerous discussions about surprising results. I would also like to extend my gratitude to Thomas Ratz for the deposition of cuprous oxide and for all the suggestions he provided to collect experimental data. Besides, I would like to thank both Sunil and Thomas for their help in the optical characterization of the samples.

Thanks should also go to Sunil and Sylvain Blanco Alvarez for their contribution to the acquisition of SEM images. Special thanks to Sylvain who explained me the different types of detectors. I also had great pleasure of working with Emile Fourneau, who gave me an introduction to the AFM and various deposition methods. Thanks also to François Balty, Valentin Froidart, Naama Sliti, and Bob Vermeulen for sharing their findings while working at the SPIN Lab.

A big thank you to my parents and sister for their support and patience that allowed me to get this far.

Last but not least, my deepest thanks to Thibaud, for his listening, unfailing support, and for all the attentions he gave me since we met.

Contents

List of Figures

List of Tables

Acronyms

AC Alternating Current. 46
AgNW Silver Nanowires. 4, 27–29, 31, 40, 108, 111, 112
APCVD Atmospheric-Pressure Chemical Vapor Deposition. 22
AZO Aluminum doped Zinc Oxide. 17, 22, 110

BSE Backscattered Electrons. 62

CVD Chemical Vapor Deposition. 46, 48, 109

DC Direct Current. 46, 56, 64
DFT Density Functional Theory. 17, 18

EG Ethylene Glycol. 32

FoM Figure of Merit. 13–15, 36, 84, 85
FTO Fluorine doped Tin Oxide. 17, 22, 27, 110

ITO Indium Tin Oxide. 2, 22, 27, 28, 110

LED Light Emitting Diodes. 28, 29

MNW Metallic Nanowires. 1, 27, 28

OLED Organic Light Emitting Diode. 29

PDLC Polymer-Dispersed Liquid Crystal. 29
PLD Pulsed Laser Deposition. 22
PMT Photomultiplier Tube. 70
PVD Physical Vapor Deposition. 46, 48, 49, 58, 111
PVP Polyvinylpyrrolidone. 32, 40, 44, 45, 75, 93, 101, 111

RF Radio-Frequency. 4, 46, 56, 58, 87, 99, 104, 111

SE Secondary Electrons. 62

SEM Scanning Electron Microscope. 50, 59, 61–63, 71, 72, 78–81, 88, 92

TCM Transparent Conductive Materials. 3, 5

TCO Transparent Conductive Oxides. 1–3, 15–23, 26–30, 103, 110

TFH Transparent Film Heaters. 29

UTMF Ultra Thin Metallic Films. 1, 3, 27

XRD X-ray Diffraction. 62, 95, 102

XRR X-ray Reflectivity. 95, 102

List of Symbols

Symbol	**Physical Quantity**	**Units**
α	Absorption coefficient	$\mathrm{m^{-1}}$
α	Fitting parameter	-
a	Interatomic distance	m
A	Absorptance	-
$\mathcal{A}$	Absorption	-
$\boldsymbol{B}$	Magnetic field	T
c	Speed of light	$3 \times 10^{8}\ \mathrm{cm\,s^{-1}}$
d	distance	m
D_{NW}	Nanowire diameter	m
e	Elementary charge	1.6×10^{-19} J
e	Evaporation rate	$\mathrm{m\,s^{-1}}$
ε_0	Vacuum electrical permittivity	$8.854 \times 10^{-12}\ \mathrm{F\,m^{-1}}$
ε_r	Relative electrical permittivity	-
$\boldsymbol{E}$	Electric field	$\mathrm{V\,m^{-1}}$
E	Energy	eV
E_c	Conduction band	eV
E_F	Fermi level	eV
E_g	Band gap	eV
E_g^{MB}	Burstein-Moss shift	eV
E_g^{opt}	Optical band gap	eV
E_u	Urbach energy	eV
E_v	Valence band	eV
η	Dynamic viscosity	Pa s

Symbol	**Physical Quantity**	**Units**
f	Fraction	-
$\boldsymbol{F}$	Force	N
$\mathrm{FoM_H}$	Haacke's figure of merit	Ω^{-1}
$\mathrm{FoM_J}$	Jain's figure of merit	Ω^{-1}
φ	Nanowire-substrate angle	-
φ_0	Incident intensity	$\mathrm{W\,m^{-2}}$
φ_B	Energy barrier	eV
φ_R	Reflected intensity	$\mathrm{W\,m^{-2}}$
φ_T	Transmitted intensity	$\mathrm{W\,m^{-2}}$
γ	Conductivity exponent	-
γ	Surface tension	$\mathrm{N\,m^{-1}}$
γ_s	Surface energy	$\mathrm{J\,m^{-2}}$
h	Plank's constant	$6.626 \times 10^{-34}\ \mathrm{J\,s}$
I	Current	A
J	Current density	$\mathrm{A\,m^{-2}}$
k	Stiffness	$\mathrm{N\,m^{-1}}$
$\boldsymbol{k}$	Wave vector	$\mathrm{m^{-1}}$
k_B	Boltzmann constant	$1.38 \times 10^{-23}\ \mathrm{J\,K^{-1}}$
L	Length	m
L	Molar latent heat	$\mathrm{J\,mol^{-1}}$
L_{NW}	Nanowire length	m
l_b	Bulk mean free path	m
λ	Wavelength	m
λ_p	Plasma wavelength	m
m	Mass	kg
m_e^*	Electron effective mass	kg
m_h^*	Hole effective mass	kg
μ_e	Electron mobility	$\mathrm{m^2\,V^{-1}\,s^{-1}}$
μ_h	Hole mobility	$\mathrm{m^2\,V^{-1}\,s^{-1}}$
ν	Frequency	$\mathrm{s^{-1}}$

Symbol	**Physical Quantity**	**Units**
n	Refractive index	-
n	Electron concentration	m^{-3}
n	Network density	m^{-2}
n_c	Critical network density	m^{-2}
ω	Angular velocity	s^{-1}
ω_{mec}	Mechanical resonant frequency	s^{-1}
ω_p	Plasma frequency	s^{-1}
p	Hole concentration	m^{-3}
p	Momentum	$\mathrm{kg\,m\,s}^{-1}$
P	Probability	-
P	Pressure	Pa
r	Distance	m
R	Electrical resistance	Ω
R	Reflectance	-
R	Radius	m
R_s	Sheet resistance	Ω/sq
ρ	Radius of the meniscus	m
ρ	Fluid density	$\mathrm{kg\,m}^{-3}$
ρ	Electrical resistivity	$\Omega\,\mathrm{m}$
ρ_b	Bulk electrical resistivity	$\Omega\,\mathrm{m}$
S	Cross section	m^2
σ	Electrical conductivity	$\Omega^{-1}\,\mathrm{m}^{-1}$
t	Time	s
t	Thickness	m
T	Temperature	K
T	Transmittance	-
T_m	Melting temperature	K
T_m^b	Bulk melting temperature	K
$T_{R_{\mathrm{min}}}$	Minimum resistance temperature	K
T_{sph}	Spheroidization temperature	K

Symbol	**Physical Quantity**	**Units**
τ_e	Electron relaxation time	s
τ_h	Hole relaxation time	s
τ_b	Bulk relaxation time	s
θ_1	Liquid-substrate contact angle	-
θ_2	Liquid-nanowire contact angle	-
v	Velocity	$\mathrm{m\,s^{-1}}$
V	Voltage	V
V	Volume	$\mathrm{m^3}$
V_B	Breakdown voltage	V
V_s^b	Molar volume	$\mathrm{m^3\,mol^{-1}}$
W	Width	m

Introduction

To improve the standard of living in our modern society, research can be devoted to transparent conducting materials. They are relevant in many sectors, such as health, safety, communication, energy, comfort, and entertainment. One prominent example of technological applications are smart windows, which become smart by adding electronic features to glass. Some applications are windows with variable light transmission, involving on demand or automatic switching from clear to dark, automobile windshields that project a virtual image containing important road information, automobile windshields containing transparent heaters, and windows incorporating photovoltaic cells for electric energy production [1]. Furthermore, the increasing demand for foldable and wearable electronics has led to a need for flexible optoelectronic components. Some applications include skin sensors for healthcare, foldable screens for smartphones, rollable electronic papers, and large-sized curved screens to improve side vision. Other important characteristics for the production of optoelectronic devices are raw material and production costs, scalability of the fabrication method, stability and environmental friendliness of materials.

Independently of the targeted optoelectronic device, a common crucial component in all examples cited above is a transparent electrode; allowing light to enter or leave the device, while ensuring a good electrical conductivity between the active layers and the external circuit. The real challenge is to combine optical transparency and electrical conductivity in the same device, since highly optically transparent materials (glass, plastic) are insulating, while highly electrically conducting materials (silver, gold) are opaque.

Optoelectronic components are made of active layers sandwiched between two electrodes. To ensure a good transmission in the visible spectral range while ensuring a sufficient electrical conductivity, two approaches are possible to replace the usually opaque electrode at the top of the device. The first possibility is to strongly dope highly transparent semiconductors, which are called Transparent Conductive Oxides (TCO). The other solution is to start from highly conductive metals and to make them transparent by reducing their dimensions. Examples belonging to this second approach are Ultra Thin Metallic Films (UTMF) and Metallic Nanowires (MNW). The bar graph displayed in Figure 1 shows the annual publications involving the keywords “Transparent electrode” between 2010 and 2019. The increasing data, reported by Scopus citation database, show that transparent electrode is a current research topic.

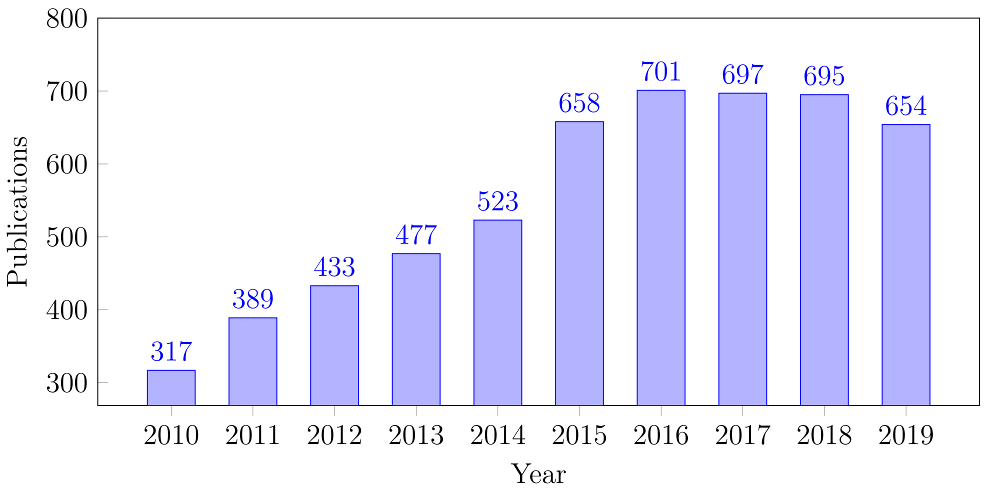

Figure 1: Number of publications concerning the keywords “Transparent electrode” reported by Scopus citation database.

The active layers sandwiched between the electrodes can be either made of organic or inorganic semiconductors. Inorganic semiconductors have been extensively studied and implemented in optoelectronic devices thanks to their long lifetime, brightness, efficiency, and color purity, but present a rigid character [2]. Organic semiconductors, like conductive polymers, recently emerged due to the increasing demand for flexible devices. In addition to being flexible, organic materials are low cost and compatible with large-scale manufacturing. Nevertheless, they suffer from oxidation and temperature-induced degradation. Another approach to meet the flexibility requirements, is to grow ultra-thin inorganic semiconducting layers by epitaxy and to transfer them on flexible substrates.

In view of transparent electronic components, the semiconducting active layers must also transmit a high percentage of the incident light. In the category of n-type inorganic semiconductors, TCO present the best compromise between good conductivity and transparency. Unfortunately, the lack of p-type TCO, delays the emergence of transparent inorganic optoelectronic components based on pn-junctions [3].

An interesting combination of p-type and n-type inorganic semiconductors that is currently studied is the Cu_2O-ZnO pn-junction, made of transparent aluminum doped zinc oxide and yellowish magnesium doped cuprous oxide [4]. These materials exhibit a good transmittance thanks to their wide gap compared to other inorganic semiconductors. Their conductivity is enhanced by substitutional doping. This pn-junction can, for example, be used as a solar cell, in which electron-hole pairs are generated to generate a current, or as a light-emitting diode, in which the recombination of electron-hole pairs generates light. A schematic illustration of this type of junction acting as a solar cell is shown in Figure 2. The electrodes, made of a thin metallic copper layer and a transparent conductive material like Indium Tin Oxide (ITO), are fabricated at the top and bottom of the active layer to collect the excess carriers and produce a current in the external circuit.

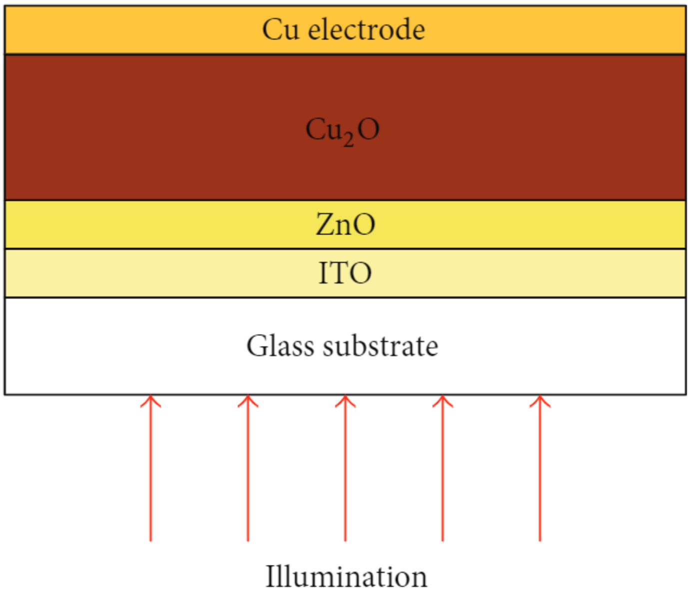

Figure 2: Schematic of the structure of a solar cell [5]. The goal of this thesis is to fabricate the Cu_2O layer by magnetron sputtering and to replace the opaque copper electrode by a transparent network of silver nanowires.

The goal of this thesis is to fabricate the upper part of the solar cell displayed in Figure 2. While the Cu_2O layer will be deposited on the glass substrate by magnetron sputtering, the upper electrode will be made of a spin coated transparent network of silver nanowires. The advantage of a silver nanowire network, compared to other types of transparent electrodes like UTMF or TCO, is its possibility to be integrated in flexible devices.

At first, the silver nanowire networks and the Cu_2O films will be treated independently. The parameters chosen during the deposition processes are the keys to achieve good quality layers. Their optical and electrical properties will be measured and compared to results found in the literature. Finally, both layers will be assembled in order to better understand the physical mechanisms occurring at the interface between the electrode and the semiconductor.

In the introductory chapter, we give an overview of Transparent Conductive Materials (TCM) that can be used as transparent electrodes. Firstly, we describe the physical principles that are responsible for the electrical and optical properties of metals and semiconductors. Then, we discuss how to assess the performances of a transparent electrodes and thin films, since a compromise must be made between optical transparency and electrical conductivity. Specific attention is devoted to the influence of doping on the electrical and optical properties of TCO, which can be used both as transparent electrodes and active layers. The impact of the metallic film thickness on the optoelectric properties of UTMF is also discussed. Finally, the advantages and drawbacks of a silver nanowire network are compared to TCO and UTMF. A wide range of applications of silver nanowire electrodes is presented to show that they are promising candidates to replace TCO and UTMF in view of flexible transparent optoelectronic devices.

The second chapter presents the state of the art of silver nanowire networks. We start by explaining how to synthesize long-aspect ratio silver nanowires and how to fabricate a silver nanowire network by spin coating. Understanding the spin coating process is important, since the fabrication process affects the quality of the resulting network. After that, we give a brief introduction to percolation theory, in order to define the percolation threshold. This threshold is crucial, since it determines whether the network will be conductive or not, hence whether the network can be used as an electrode. The main parameters affecting the electrical and optical properties of the network are the nanowire network density and the nanowire size. A theoretical study is performed to predict which nanowire network density should provide the best compromise between optical transparency and electrical conductivity. We end this chapter by explaining how to improve the conductivity of the silver nanowire network by post-deposition thermal annealing.

In the third chapter, we compare various physical vapor deposition methods for the fabrication of thin films. Several methods are presented in detail to justify the choice of Radio-Frequency (RF) magnetron sputtering of Cu_2O. Specific attention is devoted the sputtering parameters and conditions, as they greatly influence the structural, optical, and electrical properties of the thin film.

The fourth chapter deals with geometrical, electrical and optical characterization techniques that will be used in this work to assess the properties of the Silver Nanowires (AgNW) networks and the Cu_2O films. To better understand the working principle of the scanning electron microscope, which will, for example, be employed to compute the network density of the silver nanowire networks, we address the electron-matter interactions and the choice of secondary electron detector. For the electrical characterization using a 4-point measurement and the optical characterization employing a spectrophotometer, we explain on which physical principles the method is based.

The experiments carried out in the framework of this thesis are presented and discussed in the last two chapters. In Chapter 5, the silver nanowire networks have been spin coated on glass to optimize the deposition process and to test the post-deposition annealing technique. An optical, electrical, and morphological characterization of the networks is performed using the methods described in Chapter 4. SEM images allow to make the link between the theory described in Chapter 2 and the optical and electrical properties of the networks.

In Chapter 6, we justify the choice of the sputtering parameters to fabricate the Cu_2O films based on the theoretical considerations presented in Chapter 3. The spin coating process yielding the best compromise between optical transparency and electrical conductivity on glass is then applied to these undoped Cu_2O films. SEM images are exploited to better understand the interdependence between the nanowires and the underlying substrate, and their impact on the optical and electrical properties of the network. In the second part of this chapter, silver nanowires are spin coated on Cu_2O:Mg. Both film types have been tested, because the wetting properties, the roughness, the chemical composition, and the conductivity of the virgin films also influence the properties of the network. To conclude, we look back on the advantages and drawbacks of fabricating a silver nanowire network by spin coating and thermal annealing to give direction on how to improve the quality of the network.

Chapter 1

Topical background

In this introductory chapter, we discuss the electrical and optical properties of materials from a macroscopic and a microscopic point of view. We make the link between these properties and the materials electronic band structure, and explain how to compare the performances of various TCM. Then, for each type of TCM, fundamental principles, advantages and drawbacks are discussed. We end this chapter by mentioning their implementation in technological applications, such as light emitting diodes, solar cells, transparent heaters, and smart windows.

Contents

1.1 Characterization of materials

Materials can be divided into three categories: conductors, insulators and semiconductors. By contrast to conductors, insulators exhibit a poor conductivity. Furthermore, whereas conductors such as silver and gold are opaque, most famous insulators like glass and plastic are transparent. Semiconductors exhibit properties in between conductors and insulators. To better understand the origin of these properties, we can make use of band theory.

A simplified version of the electronic band structure of conductors, semiconductors and insulators is presented in Figure 1.1. Two scenarios are possible for conductors: the valence band is partly filled and the conduction band is empty, or the valence band is entirely filled and overlaps with the conduction band. The second scenario is illustrated in Figure 1.1. In both cases, electrons are free to move when the material is subjected to an electric field. These free electrons are responsible for the high conductivity of metals. In insulators, electrons cannot move because the valence band is completely filled. The conduction band is empty since the band gap between both bands is much larger than external energy that could promote an electron form the valence band into the conduction band. Therefore, insulators exhibit a low electrical conductivity. Finally, semiconductors have a smaller bandgap than insulators. This allows an electron in the valence band to be thermally, electrically, or optically excited in the conduction band, while leaving a hole in the valence band. In the end, both charge carriers enhance the conductivity of the semiconductor.

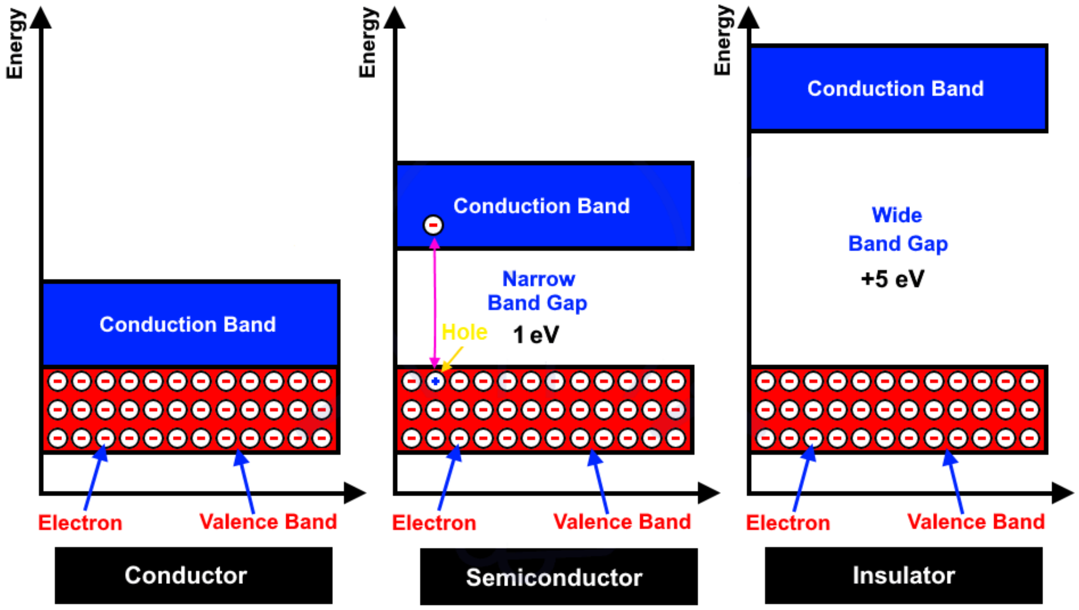

Figure 1.1: Difference in band structure between a conductor, a semiconductor and an insulator. Illustrations found on `www.electricaltechnology.org`.

Electrons must respect the Pauli exclusion principle, stating that two electrons can never be in the same quantum state. The probability that a particular state of energy E is occupied by an electron is given by the Fermi-Dirac distribution function

$$f(E) = \frac{1}{1 + \exp\left(\dfrac{E - E_F}{k_B T}\right)}, \tag{1.1}$$

where E_F [eV] is the Fermi level, k_B [$\mathrm{m^2\,kg\,s^{-2}\,K^{-1}}$] is the Boltzmann constant, and T [K] is the temperature. At 0 K, $f(E) = 1$ for $E < E_F$ and $f(E) = 0$ for $E > E_F$, meaning that all states having energies less than the Fermi level are occupied, whereas states higher than the Fermi level are empty. In conductors the Fermi level is located in the conduction band, while in insulators it is located somewhere within the band gap, where no electronic states are available. In an undoped, intrinsic semiconductor, the Fermi level is located approximately in the middle of the band gap.

Because the electronic band structure depends on the interatomic distance, band theory is also able to explain the optical properties of materials. When light strikes a material, photons are absorbed if they have enough energy to promote an electron from a lower to a higher energy state. Hence, photons with energies greater than the band gap are absorbed, while the others are transmitted as if the lattice were transparent. This explains why wide band gap materials such as insulators appear transparent, whereas conductors look opaque. In a metal, electrons can be excited from many different filled levels and decay back to many empty levels. Hence, light of varying wavelengths is absorbed and emitted, resulting in the shiny appearance of metals.

1.1.1 Electrical properties

Ohm's law states that when a voltage difference V [V] is applied across a conductor of length L [m], it creates an electric field E [$\mathrm{V\,m^{-1}}$] and a current density J [$\mathrm{A\,m^{-2}}$] that is proportional to the voltage difference, i.e.

$$J = \sigma E = \sigma \frac{V}{L}, \tag{1.2}$$

where σ [$\Omega^{-1}\mathrm{m}^{-1}$] is called the electrical conductivity [6]. Because the current density is $J = I/S$, where I [A] is the current and S [$\mathrm{m^2}$] is the cross section of the conductor, the voltage difference writes

$$V = \frac{L}{\sigma\, S} I = RI, \tag{1.3}$$

where

$$R = \frac{V}{I} = \frac{L}{\sigma\, S} = \frac{\rho\, L}{S} \tag{1.4}$$

is Pouillet's law. The quantity R [Ω] is called the electrical resistance and $\rho = 1/\sigma$ [$\Omega\,\mathrm{m}$] is termed the electrical resistivity.

Like the electrical resistance, the electrical resistivity is used to quantify the opposition of the current flow. However, while the resistance depends on the dimensions of the material, the *bulk* resistivity is an intrinsic property independent of the geometry. We stress out the word bulk because the electrical resistivity of nanosized materials (thin films, nanowires, and nanoparticles) depends on dimensions due to increased surface scattering effects with respect to bulk scattering effects.

Electrical conductivity In terms of microscopic quantities, the electrical conductivity σ of an isotropic semiconductor is given by

$$\sigma = ne\mu_e + pe\mu_p, \tag{1.5}$$

where e [C] is the elementary charge, n and p [m^{-3}] are the electron and hole concentrations, and μ_e and μ_p [$\mathrm{m}^2\,\mathrm{V}^{-1}\,\mathrm{s}^{-1}$] are the electron and hole mobilities. The mobility reflects the easiness for charge carriers to move within the material. It can be expressed as

$$\mu_e = \frac{e\tau_e}{m_e^*} \quad \text{and} \quad \mu_h = \frac{e\tau_h}{m_h^*}, \tag{1.6}$$

where τ_e or τ_h [s] is the average time between collisions (also called the carrier relaxation time), and m_e^* and m_h^* [kg] are the effective electron and hole masses to take the effect of the lattice on the electron dynamics into account.

From an energetic point of view, the effective mass is inversely proportional to the energy curvature in the three-dimensional reciprocal $\boldsymbol{k}$ space[1]. Indeed, for energy bands centered at $\boldsymbol{k} = 0$, the energy of an electron near the conduction band minimum E_c [eV] and the energy of a hole near the valence band maximum E_v [eV] are respectively given by

$$E(\boldsymbol{k}) \simeq E_c + \frac{\hbar \boldsymbol{k}^2}{2m_e^*}, \tag{1.7}$$

$$E(\boldsymbol{k}) \simeq E_v - \frac{\hbar \boldsymbol{k}^2}{2m_h^*}, \tag{1.8}$$

where $\hbar = h/2\pi$ and h [J s] is Planck's constant. Hence, the curvatures of the conduction and valence bands are respectively

$$\frac{d^2E(\boldsymbol{k})}{d\boldsymbol{k}^2} = \frac{\hbar}{m_e^*} \quad \text{and} \quad \frac{d^2E(\boldsymbol{k})}{d\boldsymbol{k}^2} = \frac{\hbar}{m_h^*}. \tag{1.9}$$

The last relationship indicates that energy bands with a high curvature correspond to low effective masses, which in turn results in a higher mobility. Generally, electrons are more mobile than holes because the curvature of the conduction band is larger than the curvature of the valence band.

---

[1] The reciprocal lattice space represents the Fourier transform of the real/physical lattice space. It is commonly used in solid-state physics because each wave vector $\boldsymbol{k}$ [m^{-1}] describing the electronic wave function associated to an electron is a point in the reciprocal space.

Carrier mobility The overall mobility of electrons depends on several scattering mechanisms such as lattice vibration/phonon scattering, ionized impurity scattering, grain boundary scattering, and lateral surface scattering. The scattering probability dP [-] of an electron over a time interval dt [s] can be written as

$$dP(t, t+dt) = \sum_i \frac{dt}{\tau_i}, \tag{1.10}$$

where τ_i [s] is the average time an electron can travel without being scattered by a mechanism of type i. The average time between the scattering by any of the above mentioned mechanisms is thus given by

$$\frac{1}{\tau_e} = \sum_i \frac{1}{\tau_i}. \tag{1.11}$$

Hence, because μ_e is directly proportional to τ_e, the overall mobility of electrons writes

$$\frac{1}{\mu_e} = \sum_i \frac{1}{\mu_i}, \tag{1.12}$$

where μ_i denotes the mobility of electrons associated to a specific type of scattering.

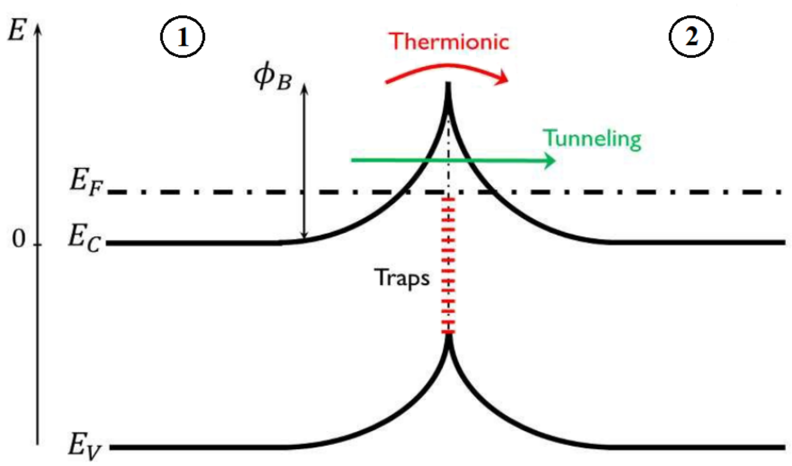

Figure 1.2: Schematic of the band energy of an n-type degenerate semiconductor at the vicinity of a grain boundary. [7]

Grain boundaries are regions where the crystal lattice is disrupted. Electronic defects at the grain boundaries act as electron traps. Due to the accumulation of trapped electrons, a space charge appears on both sides of the grain boundary and results in a potential barrier, as shown in Figure 1.2. Consequently, the carriers can only cross the grain boundary by thermionic emission, if they have enough energy to go over the potential barrier ϕ_B [eV], or by electron tunneling. This makes the transition of electrons between neighboring grains difficult and thus reduces their mobility.

1.1.2 Optical properties

As already mentioned, a photon is absorbed by the material if it carries enough energy to excite an electron from a lower to a higher energy state. The best-known transition is the direct excitation of an electron from the conduction band to the valence band. However, other transitions involving higher energy bands, impurity states, or phonons[2] are also possible. Consequently, based on a microscopic approach, the absorption coefficient α $[\mathrm{m}^{-1}]$ is defined as follows:

$$\alpha(h\nu) \sim \sum P_{if}\, n_i\, n_f, \tag{1.13}$$

where the sum is performed over all possible transitions between states separated by an energy $h\nu$ [eV], n_i $[\mathrm{m}^{-3}]$ is the electron density in the occupied initial states, n_f is the density of empty final states $[\mathrm{m}^{-3}]$, and P_{if} [-] is the transition probability [8].

Aside from the need of having an occupied state at lower energy and an empty state at higher energy, absorption phenomena are governed by energy conservation and momentum conservation laws. Nevertheless, we may consider the momentum of the photon negligible with respect to that of the electron since

$$\begin{aligned} p = \hbar k &= \frac{h}{2\pi}\frac{2\pi}{\lambda} = \frac{h}{\lambda} \quad \text{with} \quad \lambda > 100\,\mathrm{nm} \quad \text{for photons,} \\ p = \hbar k &= \frac{h}{2\pi}\frac{2\pi}{a} = \frac{h}{a} \quad \text{with} \quad a \sim 5 \qquad\quad \text{for electrons,} \end{aligned}$$

where a [m] is the atomic spacing.

If the conduction band minimum and valence band maximum occur at the same wave vector $\boldsymbol{k}$, the smallest energy-transition can be performed by an electron without a change in $\boldsymbol{k}$. An electron can go from the valence band to the conduction band or vice versa by absorbing or emitting a photon of energy $h\nu \geq E_g$. We say that the semiconductor has a direct band gap (Figure 1.3 on the left).

By contrast, if the conduction band minimum is at a different $\boldsymbol{k}$ value than the valence band maximum, the transition from the smallest energy-transition requires a change in $\boldsymbol{k}$, i.e. a change in momentum, and a change in energy for the electron [9]. This type of semiconductor is called an indirect semiconductor, since the transition of an electron between the valence band and the conduction band is indirect (Figure 1.3 on the right).

For example, in addition to emitting a photon, the electron can transfer momentum to the crystal lattice in the form of a phonon, or the electron can go through a defect state within the band gap. In general, the energy of the electron is given up as heat to the lattice rather than emitted as a photon. Therefore, optoelectronic devices generally prefer the use of direct semiconductors.

---

[2] A phonon is a quantum of vibrational energy in a crystalline solid.

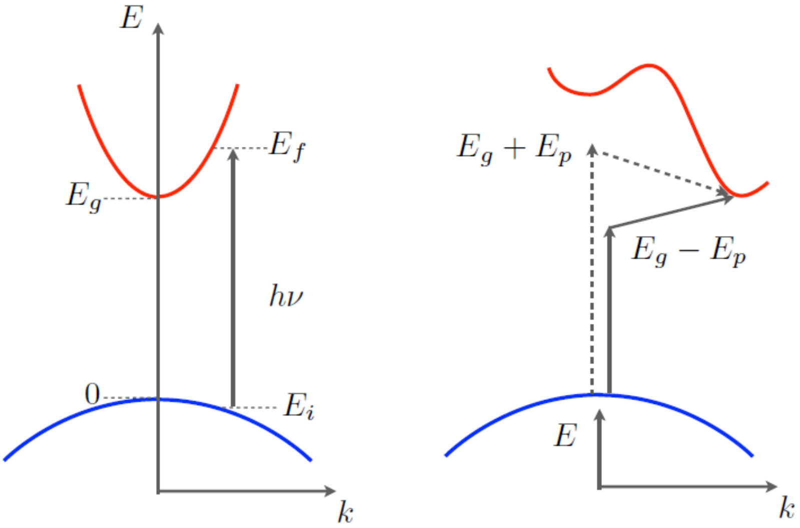

Figure 1.3: Band diagram of a direct band gap material on the left, and an indirect band gap material on the right. [8]

Band gap measurement Once the absorption coefficient is known for a certain range of wavelengths, the band gap of the material can be determined. The method to compute this band gap depends on whether the material has a direct or indirect band gap.

It can be shown [10] that, for a direct band gap material, the absorption coefficient α features a square root dependence on the photon energy $h\nu$ for photons with an energy larger than the band gap E_g [eV]:

$$\alpha(h\nu) = A\sqrt{h\nu - E_g}, \tag{1.14}$$

with A a constant depending on the properties of the material. Therefore, as shown in Figure 1.4, α^2 depends linearly on $h\nu$ for energies above the band gap. Photons with an energy lower than the band gap are not absorbed because there are no available energy states between the valence band and the conduction band, provided that there are no defects states within the band gap. In a perfect crystal, the absorption coefficient is thus zero below the band gap energy.

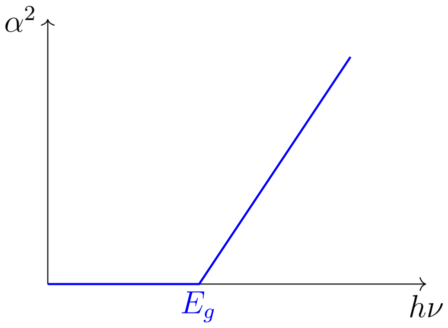

Figure 1.4: Illustration of the squared absorption coefficient as a function of the incident photon energy depending on the band gap of the direct semiconductor.

For an indirect band gap, the method to determine the band gap is similar, but the absorption coefficient has a squared dependence on the photon energy and the involvement of a phonon in the transition requires particular attention. We will not detail this case since the semiconductor that will be studied in this work (Cu_2O) exhibits a direct band gap. The interested reader may refer to J. Pankhove's book on "Optical processes in semiconductors" [10].

In practice, structural and interface defects have an influence on the band structure of the semiconductor. The more disorder in a crystal, the shorter the interaction distance between atoms, and the more the electronic wave functions can overlap. The merging of a band of defect states with the conduction band leads to a quasi continuum of energy states, called band tails [10], extending in the band gap. Dislocations, around which the atoms of the crystal lattice are misaligned, and grain boundaries are at the origin of localized quantum wells and potential barriers which can trap free carriers [11]. This accumulation of charges also contributes to the band tails.

As a consequence, extra low-energy states become available, enabling the absorption of photons with an energy lower than the band gap. This is why, experimentally, an exponentially increasing absorption edge is measured instead of the theoretical sharp absorption drawn in Figure 1.4. The value of the band gap E_g can be recovered from the experimental data by plotting α^2 as a function of $h\nu$ and performing a linear regression on the linear part of this curve. The band gap is then given by extrapolating the linear regression to the x axis intercept.

The width of the band tails extending in the band gap, also called the Urbach energy E_u [eV], can be estimated from the following relationship:

$$\alpha = \alpha_0 + \exp\left(\frac{E}{E_u}\right), \tag{1.15}$$

where α is the absorption coefficient, α_0 is a constant, and $E = h\nu$ is the photon energy [12]. When plotting $\ln \alpha$ against $h\nu$, the reciprocal of the linear fit below the band gap gives the value of the Urbach energy E_u. Since the Urbach energy increases with increasing structural disorder, it gives an idea about the quality of the semiconductor (e.g. crystallinity, amount of defects, lattice strain).

Experimental measurement of the absorption coefficient Experimentally, the absorption coefficient is obtained by measuring the intensity of light that is transmitted through the material. Let us consider a material illuminated by a beam of intensity Φ_0 [$\mathrm{W\,m^{-2}}$]. A first part of the initial intensity will be reflected at the interface, a second part will be transmitted, and a third part will be absorbed. These fractions of the initial light beam are respectively called reflectance $R = \Phi_R/\Phi_0$ [-], transmittance $T = \Phi_T/\Phi_0$ [-], and absorptance $A = \Phi_A/\Phi_0$ [-].

Relying on conservation of energy leads thus to the following relationship:

$$\begin{aligned} \Phi_0 &= \Phi_T + \Phi_R + \Phi_A \\ \iff 1 &= T + R + A. \end{aligned} \tag{1.16}$$

The reflectance is obtained by applying Fresnel equations for a normal incident light beam:

$$R = \left(\frac{n - n_0}{n + n_0}\right)^2, \tag{1.17}$$

where n [-] is the refractive index of the material and $n_0 = 1$ is the refractive index of air. Absorption $\mathcal{A}$ [-], not to be confused with absorptance A, is defined as the ratio of light intensity entering the material $\Phi_0 - \Phi_R$ $[\mathrm{W\,m^{-2}}]$ with respect to transmitted light Φ_T $[\mathrm{W\,m^{-2}}]$:

$$\mathcal{A} = \log_{10}\left(\frac{\Phi_0 - \Phi_R}{\Phi_T}\right) = \log_{10}\left(\frac{1 - R}{T}\right). \tag{1.18}$$

When light is transmitted through a sample, some energy is lost due to the interaction of photons with matter. According to the Beer-Lambert law, when a light beam of intensity $\Phi_0 - \Phi_R$ penetrates a sample of thickness t [m], the transmitted intensity is given by

$$\Phi_T = (\Phi_0 - \Phi_R)\exp\left(-\alpha t\right), \tag{1.19}$$

where α is the absorption coefficient.

By combining (1.18) and (1.19), an expression for the absorption coefficient as a function of reflectance and transmittance can be deduced:

$$\alpha(\lambda) = \frac{1}{\log_{10}(e)\,t}\log_{10}\left(\frac{1 - R}{T(\lambda)}\right). \tag{1.20}$$

1.2 Performance of transparent electrodes

To assess the electrical resistance of 2D thin film materials regardless of the sample size, we introduce the notion of sheet resistance R_s. By definition, the sheet resistance[3] of a material of uniform thickness t is expressed in $[\Omega/\mathrm{sq}]$ and given by

$$R_s = \frac{\rho}{t} = \sigma t, \tag{1.21}$$

where ρ is the electrical resistivity and σ is the electrical conductivity, which, as we will see later, can also depend on the film thickness. In the particular case of square samples of size L and thickness t, the bulk resistance

$$R = \frac{\rho L}{Lt} = \frac{\rho}{t} = R_s$$

coincides with the sheet resistance.

To find the best compromise between electrical conductivity and optical transparency of transparent electrodes, we can rely on Haacke's Figure of Merit (FoM) $[\Omega^{-1}]$

$$\mathrm{FoM_H} = \frac{T^{10}}{R_s}, \tag{1.22}$$

---

[3] The sheet resistance $R_s = \rho/t$ is expressed in $[\Omega/\mathrm{sq}]$ in order to avoid confusion with the bulk resistance $R = \rho L/Wt$, where W is the width of the cross section, expressed in $[\Omega]$.

with T the optical transmittance at 550 nm and R_s the sheet resistance. The larger the FoM, the better the optoelectrical properties. Transmission at 550 nm is often taken as reference because this is the wavelength to which the human eye is the most sensitive. However, regarding the solar irradiance spectrum at the Earth's surface (Figure 1.5), taking the average the transmission over a given wavelength range is more representative for photovoltaic applications.

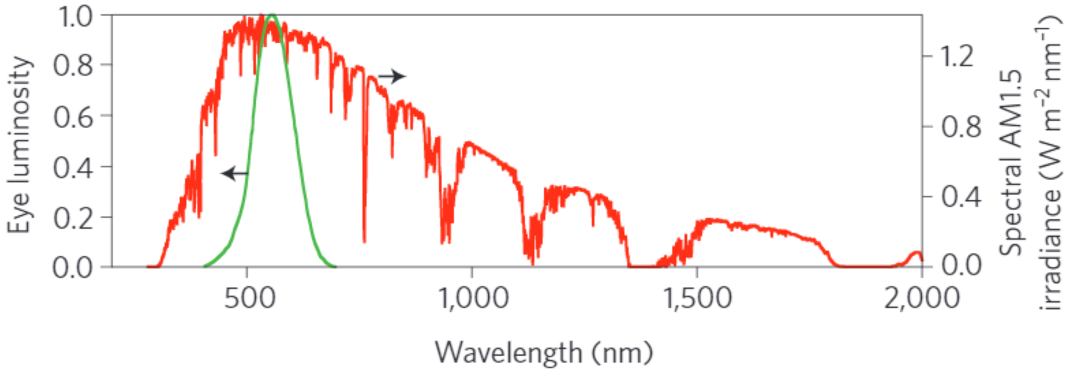

Figure 1.5: Phototopic luminosity function, i.e. spectral sensitivity of the human eye for everyday light levels in green, and solar irradiance spectrum at the Earth's surface in red. Adapted from [13].

.

The main advantage of Haacke's FoM is that R_s and T are easily measured. The problem is its dependency on film thickness, making the comparison between different transparent electrodes more difficult. Furthermore, the exponent 10 is chosen to better balance optical transparency and electrical conductivity [14], but limits the maximum transmittance to 90%. Indeed, using Beer-Lambert law, the film thickness t which maximizes

$$\mathrm{FoM_H} = \frac{T^{10}}{R_s} = \left(\frac{\varphi_0 - \varphi_R}{\varphi_0}\right)^{10} \sigma t\ \exp\left(-10\,\alpha t\right), \tag{1.23}$$

is given by

$$\begin{aligned} \frac{\mathrm{dFoM_H}}{\mathrm{d}t} &= \left(\frac{\varphi_0 - \varphi_R}{\varphi_0}\right)^{10} \sigma \exp\left(-10\,\alpha t\right)\left(1 - 10\alpha t\right) = 0 \\ \Leftrightarrow t_{\max} &= \frac{1}{10\alpha}. \end{aligned} \tag{1.24}$$

By consequence, neglecting any reflection, the maximum transmittance that can be achieved is

$$T_{\max} = \exp\left(-\alpha\, t_{\max}\right) = 90\%. \tag{1.25}$$

In other words, if the transmission of the transparent electrode is larger than 90%, the FoM-value will provide non-representative values. The existence of this upper limit is the reason why transmittance spectra of transparent electrodes should include absorption and reflection losses from the substrate. In practice, transparent electrodes rarely exceed 90% since bare glass already limits the transmittance to 92 %.

For materials with a very high transmittance (e.g. very thin nanowire networks), or when the absorbance and reflectance of the substrate has been subtracted, another FoM, introduced by Jain et al. [15], can be used. This new figure of merit involves only the optical absorption coefficient α and the electrical conductivity σ:

$$\mathrm{FoM_J} = \frac{\sigma}{\alpha}. \tag{1.26}$$

Like for Haacke's FoM, a larger value of $\mathrm{FOM_J}$ $[Omega^{-1}]$ indicates a better transparent electrode performance. Because Jain's FoM does not explicitly depend on the film thickness, it describes a material property rather than a film property [16]. Nevertheless, at the nanoscale, σ and α do depend on the film thickness.

1.3 Transparent conductive oxides

The wide band gaps of binary oxides (e.g. ZnO, SnO_2, and In_2O_3), larger than the maximum energy carried by a photon in the visible range

$$E_{ph}(\lambda = 400\,\mathrm{nm}) = h\nu = \frac{hc}{\lambda} = 3.1\,\mathrm{eV}, \tag{1.27}$$

with c [m s^{-1}] the speed of light and h Planck's constant, offer the high transparency required for transparent electrodes. Indeed, only photons with an energy larger than the band gap are absorbed through electronic transitions from the valence band to the conduction band. Unfortunately, at room temperature, undoped wide band gap semiconductors exhibit low electrical conductivities. The reason for these low conductivities is the absence of free charge carriers in the conduction and/or valence band.

1.3.1 Doping semiconductors

In order to exhibit a high conductivity, TCO should have a large concentration of free charge carriers. This can be achieved by doping. Substitutional doping consists in replacing an atom of the crystal lattice by a foreign atom, called a dopant or an impurity. While a donor is defined as an impurity atom that can donate electrons to the conduction band, an acceptor is an impurity atom that can accept electrons from the valence band while generating holes. We say that a semiconductor is n-doped when most impurities are donors, and that it is p-doped when most impurities are acceptors.

An example of n-type and p-type doping is given in Figure 1.6. On the right hand side, a silicon atom with 4 valence electrons (type IV) is replaced by a phosphorous atom with 5 valence electrons (type V). Hence, phosphorous provides an electron in excess and is called a donor. On the left hand side, a silicon atom is replaced by a boron atom with 3 valence electrons (type III). The acceptor generates an electron vacancy, known as a hole.

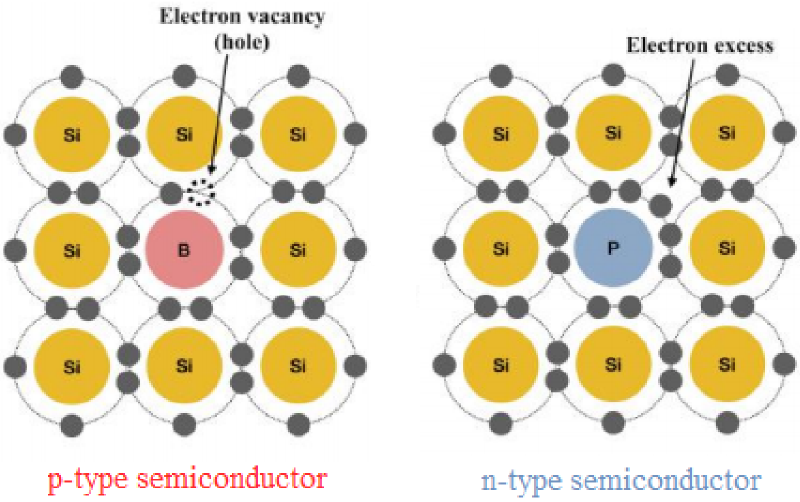

Figure 1.6: After p-type doping electrons are lacking and holes are the majority carriers, whereas after n-type doping electrons in excess are the majority carriers. [17]

Substitutional doping is the most widely used approach to generate free carriers in TCO. Compared to interstitial doping, which involves adding a foreign atom in addition to those already present in the crystal lattice, it offers a better control of resulting optical and transport properties. The main challenge in doping semiconductors is to achieve a good compatibility between the dopants and the host crystal, so that the lattice and electronic structure of the crystal are not deteriorated by defects.

Impurities with a larger radius will induce compressive strains, bringing the atoms closer to each other. Due to the increased overlaps of the valence orbitals, the curvature of the conduction band is increased and the conduction band minimum is lowered (Figure 1.7). By consequence, the electron effective mass is reduced, and the carrier mobility increased, but the band gap is reduced [18].

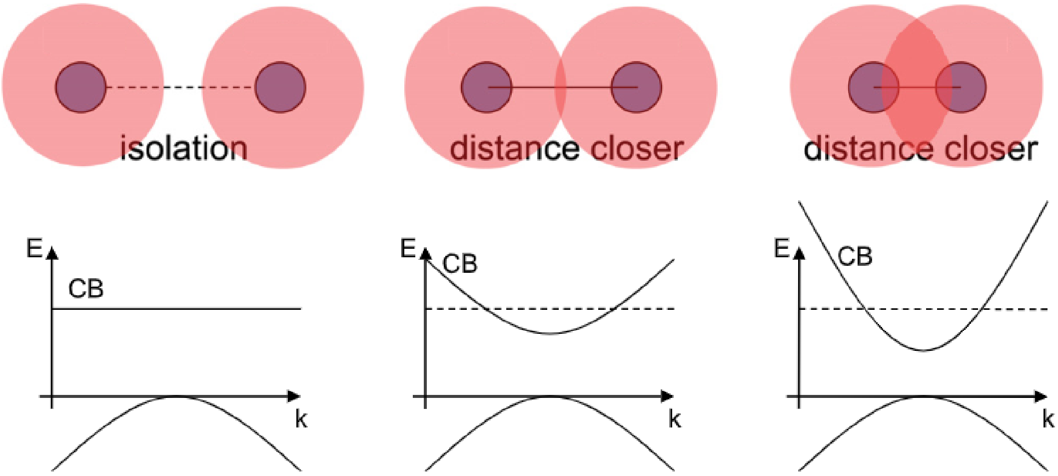

Figure 1.7: When the interatomic distance is reduced, the increased overlaps of the valence orbitals increases the curvature of the conduction band. By consequence, the conduction band minimum is lowered and the electron effective mass is reduced. Schematic diagram adapted from [18].

Nowadays, computational modeling, such as Density Functional Theory (DFT), is used to predict the band structures of various TCO depending on their composition, type of dopant, and doping concentration. This allows to narrow the experimental search of the best combination between host crystal and dopant. A computational study performed by G. Hautier et al. demonstrated that, among 4577 screened oxides, n-type TCO such as ZnO, SnO_2, and In_2O_3 are the oxides with the lowest effective masses [19], hence the best mobilities.

It is therefore not a coincidence if the most widely used n-type transparent conductive oxides are ZnO:Al, In_2O_3:Sn, and SnO_2:F. In the first example, Zn atoms (type II) are replaced by Al atoms (type III), in the second example In atoms (type III) are replaced by Sn atoms (type IV), and in the last example O atoms (type VI) are replaced by F atoms (type VII). For simplicity, these TCO are called Aluminum doped Zinc Oxide (AZO), Indium doped Tin Oxide (ITO), and Fluorine doped Tin Oxide (FTO) respectively.

The above mentioned TCO present good electrical and optical properties thanks to a good ionic radius matching between the host crystal and the dopant, and an excellent cation-oxygen overlap at the conduction band minimum [19]. While O (r=1.5Å) and F (r=1.3Å), and In (r=0.79Å) and Sn (r=0.69Å) have almost the same ionic radii, the difference is more pronounced for Zn (r=0.60Å) and Al (r=0.39Å). This is why researchers tried to replace Zn by Ga (r=0.47Å) instead [20]. However, the affordability and natural abundance of Al compared to the supply risk of Ga makes Al more competitive for industrial applications.

P-type TCO are less common in technological applications because the mobility of holes is much lower compared to that of electrons. Furthermore, p-type doping in TCO is less effective than n-type doping since the doping mechanism is more complex than substitutional doping. For example, when Cu_2O is doped with Mg, the dopant is not directly responsible for a new vacancy. Hence, Cu_2O:Mg with 17% per weight of Mg will generate a much lower number than a 17% increase of charge carriers.

The increase in conductivity of Cu_2O upon Mg doping can be explained by considering two types of vacancies occurring naturally in Cu_2O: simple vacancies and split vacancies. A simple vacancy is a simple vacant copper site; it is created by the removal of a single Cu atom and leaves the rest of the lattice unchanged. By contrast, the split vacancy is a configuration in which a nearby Cu atom distorts the lattice to partly fill a simple vacancy [21]. Schematics presenting the structure of Cu_2O are presented in Figure 1.8 for the normal, simple vacancy, split vacancy, and Mg doped configurations.

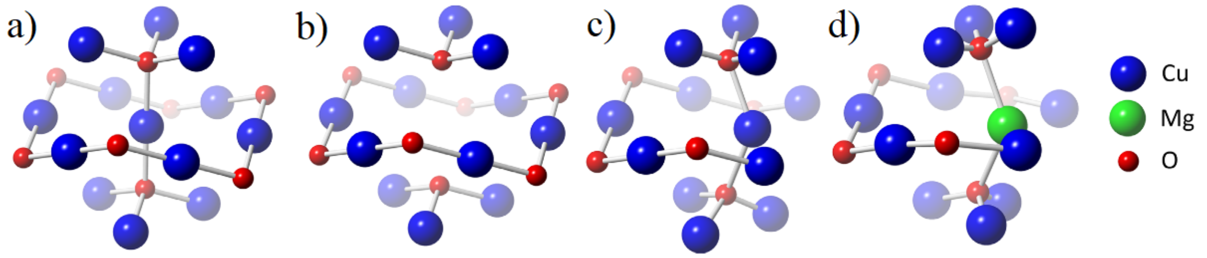

Figure 1.8: Schematic structure of (a) Cu_2O, (b) copper simple vacancy, (c) copper split vacancy, (d) magnesium split vacancy. [21]

Regarding the electronic structure, the simple vacancy acts as a delocalized hole with states close to the Fermi level, whereas the split vacancy acts as a localized hole with a trap state 0.57 eV above the Fermi level [22]. Consequently, split vacancies are more likely to trap minority carriers (electrons), limiting conductivity. Doping Cu_2O with Mg prevents the formation of copper split vacancies, avoiding the formation of trap states within the band gap and resulting in an improved conductivity.

According to Nolan [23], there are two necessary conditions to increase the band gap of Cu_2O by substitutional doping. The first condition is that the dopant distorts the local structure around the dopant site by elongating Cu-Cu distances. The second condition is avoiding misalignment of dopant electronic states with the valence band or conduction band of Cu_2O, i.e. avoiding defect states in the band gap. Using DFT simulations, Nolan demonstrated that it should be possible to increase the band gap of Cu_2O by substitutional doping with magnesium. The advantage of Mg^{2+} is that its ionic radius ($r = 0.72$ Å) is close to the ionic radius of Cu^+ ($r = 0.77$ Å), avoiding distortion of the crystal lattice in the far field. Moreover, since magnesium is non-toxic and abundant, it is an excellent candidate to dope cuprous oxide [21].

1.3.2 Impact of doping on the carrier mobility

In doped TCO, the decrease in mobility is due to the increasing importance of ionized impurity scattering. As an example, in SnO_2 and ZnO the mobility is about 250 $cm^2V^{-1}s^{-1}$ for low doping concentrations ($n \sim 10^{16}\,cm^{-3}$), but less than 70 $cm^2V^{-1}s^{-1}$ for high doping levels ($n > 10^{20}\,cm^{-3}$) [24]. The mobility is lowered further by lateral surface scattering and grain boundary scattering present in polycrystalline thin films.

At first, increasing the doping concentration provides a larger density of electrons and increases the Fermi level, which in turn reduces the potential barrier drawn in Figure 1.2 and increases the mobility. However, by further increasing the carrier concentration, ionized impurity scattering becomes the dominant scattering mechanism and leads to a decrease in mobility. Therefore, a trade-off must be found between the density of free charge carriers and their mobility.

The larger the trap density at the grain boundaries, the more electrons can be trapped, the higher the potential barrier, and thus the lower the electron mobility. In n-type TCO, the electron traps are mainly attributed to oxygen atoms adsorbed on grain boundaries. This explains why high vacuum deposition techniques are able to provide TCO films with a better conductivity than deposition methods performed in atmospheric conditions with a higher oxygen concentration [7]. The fabrication method of thin film TCO plays thus a crucial role to achieve high carrier mobilities.

1.3.3 Impact of doping on the electronic band structure

Due to the introduction of dopants, we observe a shift in the position of the Fermi level. If the semiconductor is n-doped, the electron concentration is increased, and the Fermi level is shifted towards the conduction band. By contrast, if the semiconductor is p-doped, the hole concentration is increased, and the Fermi level is shifted towards the valence band. As long as the doping is moderate, the Fermi level lies within the band gap $E_g = E_c - E_v$ and the semiconductor is said to be non-degenerate[4]. Nevertheless, to obtain functional TCO, the number of charge carriers is increased so much (10^{20} to $10^{21}\,\text{cm}^{-3}$) that the Fermi level E_F is now located above the conduction band minimum CBM or below the valence band minimum VBM as shown in Figure 1.9. In what follows, we will distinguish the fundamental band gap E_g, referring to the energy difference between the conduction band minimum and the valence band maximum, from the optical band gap E_g^{opt} [eV], defined as the lowest-energy allowed optical transition.

The upwards shift of the Fermi level upon doping increases the optical band gap E_g^{opt} by an energy E_g^{MB} [eV] called the Burstein-Moss shift. In an n-type semiconductor, Pauli's exclusion principle forbids excitation from the valence band to the conduction band into conduction band states below E_F that are already occupied. In a p-type semiconductor, the energy increase to have an optical transition from the valence band to the conduction is due to the absence of electrons between the valence band maximum and E_F, as the Fermi level lies within the valence band. However, the shift is significantly higher in n-type than in p-type semiconductors, since the Burstein-Moss shift is inversely proportional to the effective mass of the majority carriers [25].

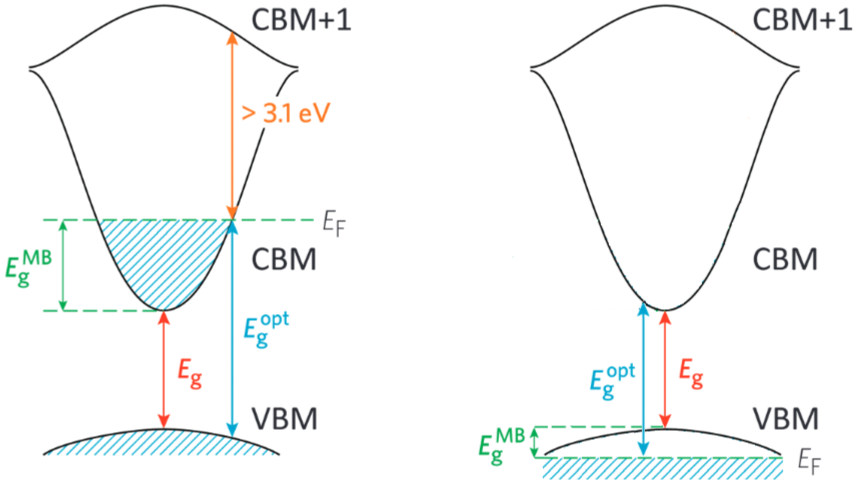

Figure 1.9: Illustration of the Burstein-Moss shift in a degenerate n-type semiconductor (left) and in a degenerate p-type semiconductor (right). CBM and VBM refer to the conduction and valence band minimum respectively. The hatched zones correspond to occupied states. Diagrams adapted from [21].

---

[4] The energy difference between the conduction band minimum and the Fermi level, or between the Fermi level and the valence band maximum, should be larger than $3k_BT$, with k_B Boltzmann constant and T the temperature.

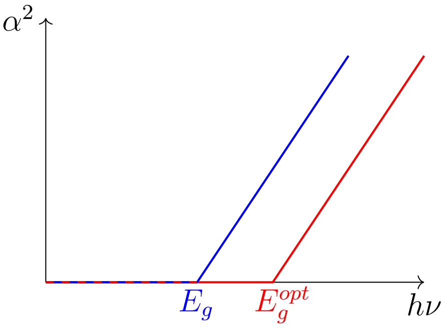

Figure 1.10: The Burstein-Moss shift moves the absorption edge ($\alpha \neq 0$) towards higher photon energies $h\nu$.

Regarding the absorption spectrum as a function of the incident photon energy for a direct band gap material (Equation 1.14 and Figure 1.10), the absorption edge E_g is moved towards higher energies $E_g^{opt} = E_g + E_g^{MB}$ due to the Burstein-Moss shift. Besides the absorption of electrons from the valence band to the conduction band, other transitions, involving different energy states, are possible. For example, the Burstein-Moss shift also gives rise to intra-band transitions within the conduction band and inter-band transitions from the conduction band to the next electronic energy level (CBM+1). The former transitions are associated to an increased absorption at lower energies (longer wavelengths in the IR region), while the latter are associated to an increased absorption at higher energies (shorter wavelengths in the UV region). Therefore, in a good TCO, the energy gap between the Fermi level and CBM+1 should be larger than 3.1 eV, as specified in Figure 1.9.

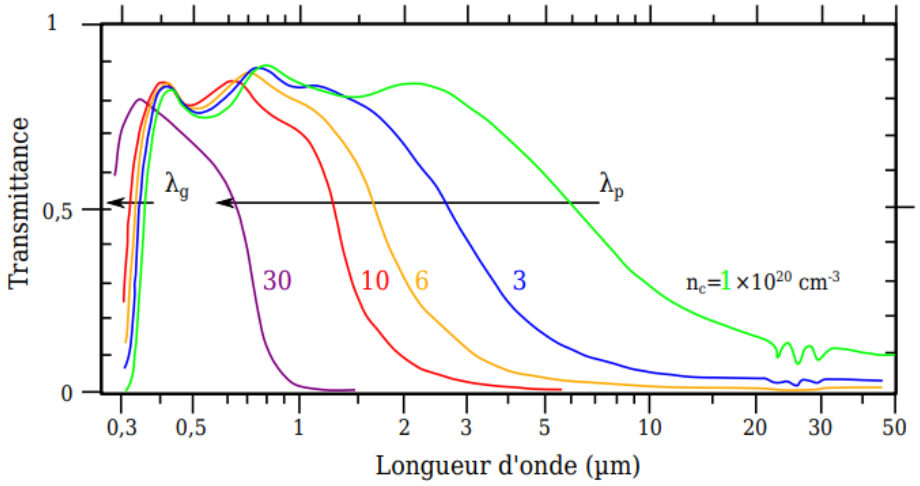

Figure 1.11: Evolution of the transmittance spectrum of ITO as a function of the density of free charge carriers. [26]

1.3.4 Impact of doping on the transmittance spectrum

The increased carrier concentration upon doping enhances the electrical conductivity and the optical transparency of TCO in the short-wavelength region of the visible spectrum. Thanks to the increased optical band gap (Burstein-Moss shift), the wavelength λ_g [m] associated to photons that are absorbed is shorter. As shown in Figure 1.11, the transparency window at short wavelengths is increased upon doping.

The limit of the transparency window at higher wavelengths is set by the plasma wavelength λ_p [m] At low wavelengths, the TCO behaves like a dielectric, i.e. an electrical insulator that can be polarized by an electric field, and is transparent. By contrast, at high wavelengths, it behaves like a metal by reflecting incident light [26]. The transition between these two regimes occurs at the plasma wavelength λ_p, or the plasma frequency ω_p [s^{-1}] given by

$$\omega_p = \frac{2\pi c}{\lambda_p}, \tag{1.28}$$

where c [$\mathrm{m\,s^{-1}}$] is the velocity of light.

In metals (and highly doped TCO), free carriers oscillate collectively at the plasma frequency. These oscillations can be understood by considering an electrically neutral plasma, consisting of a gas of negatively charged electrons and positively charged ions. If a group of lightweight electrons moves away from the heavy ions, the Coulomb force will pull the electrons back to their initial position. Like the vibrational modes of ions in a crystal are quantified by phonons, free carrier oscillations are quantified by plasmons [10].

The expression of the plasma frequency can be deduced from classical Drude theory [27] and writes

$$\omega_p = \sqrt{\frac{ne^2}{\varepsilon_r \varepsilon_0 m^*}}, \tag{1.29}$$

where $\varepsilon_r \varepsilon_0$ [$\mathrm{F\,m^{-1}}$] is the permittivity of the material at high frequency and m^* is the effective mass of the carriers. Light, which is an electromagnetic wave, is able to pass trough the material only if its frequency is larger than the plasma frequency ω_p or if its wavelength is shorter than the plasma wavelength λ_p. Hence, when TCO are highly doped, λ_p is moved towards shorter wavelengths, reducing the transparency in the infrared region. This phenomenon is illustrated in Figure 1.11.

In conclusion, TCO exhibit a band gap larger than 3.1 eV resulting in the absorption of photons with wavelengths shorter than $\lambda_g = 400$ nm, and a plasma wavelength of the order of $\lambda_p = 1$ μm above which most of the light is reflected. Hence, the transparency window of a TCO, lying between λ_g and λ_p, is able to cover the near UV, visible and near IR region. The exact range depends on the material properties and its doping concentration.

1.3.5 Advantages and drawbacks of conductive oxides

TCO suitable for transparent electrodes should have a wide band gap ($>$ 3 eV), a degenerate but not excessive carrier density (10^{20} to $2 \times 10^{21}\,\text{cm}^{-3}$), and a good mobility ($> 50\ \text{cm}^2\text{V}^{-1}\text{s}^{-1}$) to achieve an optical transmittance of 90% and an electrical resistivity $\rho < 10^{-3}\ \Omega\text{cm}$ [20]. Nevertheless, besides the figure of merit which takes transparency and conductivity into account, other factors influence the choice of transparent conducting material. This is why Gordon [24] listed important criteria such as thermal stability, chemical and mechanical durability, toxicity and production cost. For each criterion, he specified the best suited material. It is interesting to notice that In_2O_3:Sn provides the highest conductivity, but that other materials, such as SnO_2:F, are better candidates to satisfy other requirements in view of technological applications.

Due to their large bandgap, In_2O_3 (3.7 eV), SnO_2 (3.6 eV), and ZnO (3.37 eV) thin films are transparent to visible light [28], [29], [30]. Moreover, they are all able to form a degenerate semiconductor upon donor doping with little effect on transparency. The large gap between the Fermi level and the next electronic energy level prevents absorption in the visible range [29].

Currently, ITO (In_2O_3:Sn) is the most commonly used material in optoelectronic applications because of its low electrical resistivity and high optical transparency. However, scarcity and high cost of indium, and the massive demand for ITO are prompting to search for alternative materials. It turns out that when we buy a smartphone, we pay more for the display than for other components such as memory, battery or camera.

FTO (SnO_2:F) and AZO (ZnO:Al) are good candidates to replace ITO, even if their optoelectronic properties are less performing. Both consist of non-toxic and earth-abundant elements, rendering the raw materials less expensive than for ITO. Some electrical resistivities and optical transmittances achieved with different deposition techniques are presented in Table 1.1. They show that FTO and AZO are indeed able to compete with ITO. Moreover, we notice that the best electrical properties are obtained using Pulsed Laser Deposition (PLD). However, PLD is not easily scalable for industrial large-area deposition and is therefore mainly used to demonstrate the upper limits of a particular TCO. By contrast, magnetron sputtering and Atmospheric-Pressure Chemical Vapor Deposition (APCVD) are scalable methods suited for industrial production.

The main drawback of the above cited TCO is their brittleness, which precludes their deposition on flexible substrates and their application in flexible electronics. Another struggling point is their need to be processed at high temperatures, limiting their compatibility with plastic substrates. Finally, when TCO are integrated in optoelectronic devices as transparent electrodes, their lifetime is limited by the diffusion of indium or zinc ions in the active layer [31].

TCO	Technique	ρ [$\Omega\,$cm]	T [%]	Source
ITO	PLD	7.7×10^{-5}	85	[32]
ITO	DC-MS	1.5×10^{-4}	92	[33]
FTO	APCVD	2.2×10^{-4}	79	[34]
AZO	PLD	8.5×10^{-5}	88	[35]
AZO	RF-MS	2×10^{-4}	80	[36]

Table 1.1: Electrical resistivity ρ and optical transmittance T for various TCO depending on the deposition technique. PLD stands for Pulsed Laser Deposition, APCVD for Atmospheric Pressure Chemical Vapor Deposition, DC-MS for Direct Current Magnetron Sputtering, and RF-MS for Radio Frequency Magnetron Sputtering.

1.4 Ultra thin metallic films

Another approach to develop transparent conducting electrodes is to deposit ultra thin metallic films. Metals exhibit an excellent conductivity. Thanks to the absence of a band gap, a lot of electrons can be promoted from the valence band to the conduction band at room temperature, resulting in a large density of free carriers. However, due to the very high electron concentrations ($> 5 \times 10^{22}\,\mathrm{cm}^{-3}$), the plasma wavelengths of metals lie in the deep-ultraviolet spectral range ($\lambda_p < 200$ nm), resulting in a poor transmittance in the visible range [13]. Consequently, bulk metals appear opaque.

By shrinking the size of materials, their mechanical, thermodynamic, electrical, and optical properties can be modified. For example, ultra thin metal films with a thickness below 10 nm become transparent, but the electrical resistivity increases as the film thickness is sharply decreased. Hence, like for TCO, a compromise between sufficient transparency and conductivity must be found for the fabrication of ultra thin metallic electrodes.

1.4.1 Impact of film thickness on transparency

The reason why ultra thin films become transparent is related to Beer-Lambert's law, which as already mentioned previously writes

$$\Phi_T = (\Phi_0 - \Phi_R) \exp(-\alpha t), \tag{1.30}$$

where $\Phi_0 - \Phi_R$ is the intensity of the light beam penetrating the sample of thickness t, α is the absorption coefficient, and Φ_T is the transmitted intensity. This equation indicates that for a fixed absorption coefficient, which is an intrinsic property of the material, the only solution to increase Φ_T is to reduce the sample thickness t.

To achieve more than 70% transmittance in the visible range, the thickness of silver or gold films should be of the order of the nanometer [37]. However, island growth during the deposition of ultra-thin metal films degrades their electrical conductivity. A critical thickness, known as the percolation threshold, must therefore be achieved, but in turn limits the transparency. The challenge for depositing continuous and flat nanosized metal films comes from the Ostwald ripening effect [38]. As illustrated on the left in Figure 1.12, metal molecules tend to form isolated islands on the substrate because larger particles are more energetically favorable than smaller ones. This phenomenon, called Ostwald ripening, is driven by the difference in Laplace pressure between the metal particles with different radii. Because particles with a smaller radius exhibit a larger internal pressure, molecular diffusion occurs from the small sized particles towards the larger ones.

Liu et al. developed a simple multi-layer and passivation deposition method to prevent the Ostwald ripening effect. This is shown on the right-hand side in Figure 1.12. After each layer deposition by vacuum magnetron sputtering, the film is exposed to air or oxygen gas to form a thin oxide coating which is able to stop the further growth of larger particles. This method allows the production of smooth conducting films of very small thickness. The impact of the oxide coating on the conductivity is said to be negligible since it is only a few atomic layers thick, so that electrons are able to tunnel through the grain boundaries. For example, Liu et al. were able to fabricate 8.4 nm thick silver films that exhibited a transparency of 87.5% at 330 nm and a sheet resistance of 15 Ω/sq using three layers of 2.8 nm.

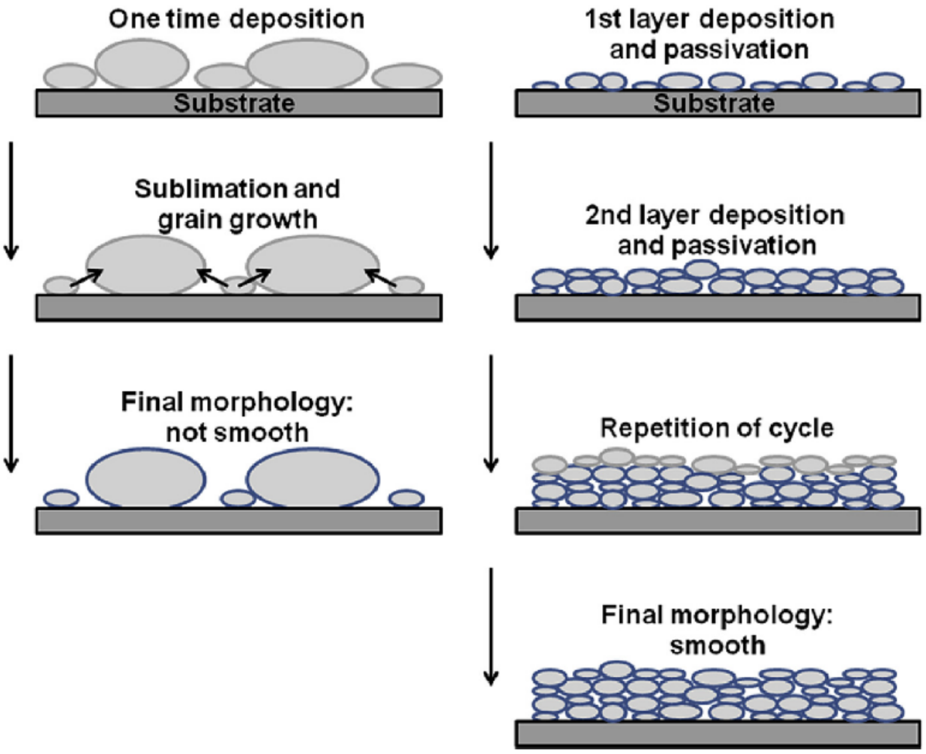

Figure 1.12: Illustration of the Ostwald ripening effect during ultra-thin metal film deposition and a new multi-layer deposition strategy to prevent its negative impact on conductivity. [38]

1.4.2 Impact of film thickness on resistivity

When the film thickness is of the order of the bulk mean free path of electrons, reported in Table 1.2, the number of collisions between the boundary of the film and electrons becomes comparable or even higher than the number of collisions originating from carrier–phonon scattering in the bulk. Because surface scattering reduces the electron mobility, we measure a higher electrical resistivity for thin films than for bulk materials. This phenomenon is called the ordinary size effect [39]. To gain a better insight into the physics responsible for the change in electrical property, we will discuss the theoretical resistivity-film thickness model established by Fred Lacy [40].

Element	Symbol	ρ_b [$\mu\Omega$cm]	τ_b [fs]	l_b [nm]
Silver	Ag	1.587	36.8	53.3
Copper	Cu	1.678	36.0	39.9
Gold	Au	2.214	27.3	37.7

Table 1.2: Bulk room-temperature resistivity ρ_b, carrier relaxation time τ_b, and mean free path l_b of the three most conductive elemental metals. [41]

When the film thickness is at least two times smaller than the bulk mean free path of electrons, i.e. $t < 2\,l_b$ [m], the increase in electrical resistivity ρ due to surface scattering can be modeled by

$$\rho = \frac{\rho_b}{\kappa(1 - \ln\kappa)} \quad \text{with} \quad 0 < \kappa = \frac{t}{2\,l_b} < 1, \tag{1.31}$$

where ρ_b [Ω m] denotes the bulk resistivity.

In addition to surface scattering, scattering from grain boundaries, impurities and rough surfaces are responsible for a further reduction of the mean free path, and thus an increase in resistivity. The importance of these effects depends on the thin film fabrication process. Ineluctably, lattice defects, impurities, and grains of different sizes will appear throughout the material during fabrication. Therefore, a scaling factor $c \geq 1$ [-] is introduced to take additional scattering effects due to impurities into account. Scattering from grain boundaries and rough surfaces is modeled by a reduced effective thickness $t - \eta$ with η [m] a reduction factor.

Finally, when considering all scattering mechanisms, the resistivity ρ of a thin film of thickness $t < 2\,l_b$ is given by

$$\rho = \frac{c\,\rho_b}{\kappa(1 - \ln\kappa)} \quad \text{with} \quad 0 < \kappa = \frac{t - \eta}{2\,l_b} < 1, \tag{1.32}$$

where c and η are adjustable parameters to ensure a good matching between experimental data and the theoretical model. Materials with c close to 1 and η close to 0 indicate that the fabrication process produces a more ideal, almost perfectly crystalline material. A comparison of experimental and theoretical resistivities for silver as a function of film thickness is shown in Figure 1.13. We notice that below 100 nm, the resistivity increases sharply.

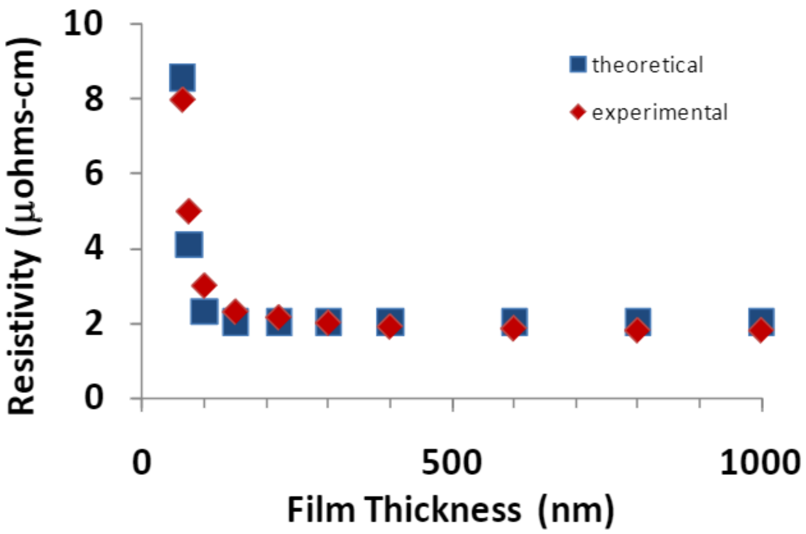

Figure 1.13: Comparison of experimental and theoretical resistivities for silver as a function of film thickness. [40]

1.4.3 Advantages and drawbacks of ultra thin metallic films

The main advantages of metals such as Ag, Cu and Au are their non-toxicity and excellent conductivity. Moreover, ultra thin metal films are interesting because of their stability and reproducibility. Vacuum thermal evaporation and sputtering are well-established, simple and affordable fabrication processes that can be performed on a substrate at room temperature. However, poor transparency limits their application as transparent electrodes. Metallic films are prone to fracture and are therefore, like TCO, not suited for flexible devices. Furthermore, gold and silver are expensive precious metals.

1.5 Metallic nanowire networks

To exploit the excellent conductivity of metals without raising their electrical resistance due to ordinary size effects in ultra-thin metallic films, one solution is to use conductive nanostructures which exhibit a high transparency. In the past few years, new kinds of transparent conducting materials, such as carbon nanotubes, graphene, and metallic nanostructures, have been thoroughly explored. The physics and parameters influencing the optoelectrical properties of silver nanowire networks will be explained in Chapter 2. The advantages, drawbacks, and possible applications of silver nanowire networks are discussed here below.

1.5.1 Advantages and drawbacks of metallic nanowire networks

MNW networks appear to be promising candidates to be integrated as transparent electrodes, since they are able to combine high electrical conductivity and high optical transparency. Up to now, silver nanowires have been the most commonly studied MNW networks thanks to their excellent conductivity (Table 1.2) and ease of synthesis compared to other metals.

Figure 1.14a compares the optical transmittance for bare glass, ITO, FTO, and AgNW networks with similar sheet resistances (about 15 Ω/sq). The three types of transparent electrode exhibit similar averaged transmission in the visible range. The oscillations for ITO and FTO in this region are due to constructive and destructive interferences associated to the continuous nature of the thin film. In the near infra-red region, ITO and FTO exhibit a much lower transmittance since their plasma wavelength is larger than 1000 nm [24]. Although the plasma wavelength of silver is 400 nm, the transmittance losses are much lower because the gaps between the nanowires are transparent. The fact that researchers managed to produce silver nanowire networks with a sheet resistance less than 10 Ω/sq and an optical transmittance of 90%, when the glass substrate contribution is subtracted [42], shows that MNW networks are already able to compete with ITO and FTO as transparent electrode.

Another asset of MNW networks compared to TCO and UTMF is their mechanical flexibility. Figure 1.14b compares the relative electrical resistance of ITO, FTO, and AgNW networks under repeated bending cycles with a radius of curvature of 5 mm. We notice that the relative electrical resistance of ITO is multiplied by a factor 20 after only 3 bending cycles, while the relative electrical resistance of the AgNW network is only increased by a few percent after 60 bending cycles [43]. Moreover, thanks to their percolating mechanism, MNW networks consume a significantly lower quantity of raw material than thin films to reach the same optoelectronic performances. Finally, MNW fabrication does not require high-temperature process steps or vacuum deposition methods, and can be extended to large area deposition methods.

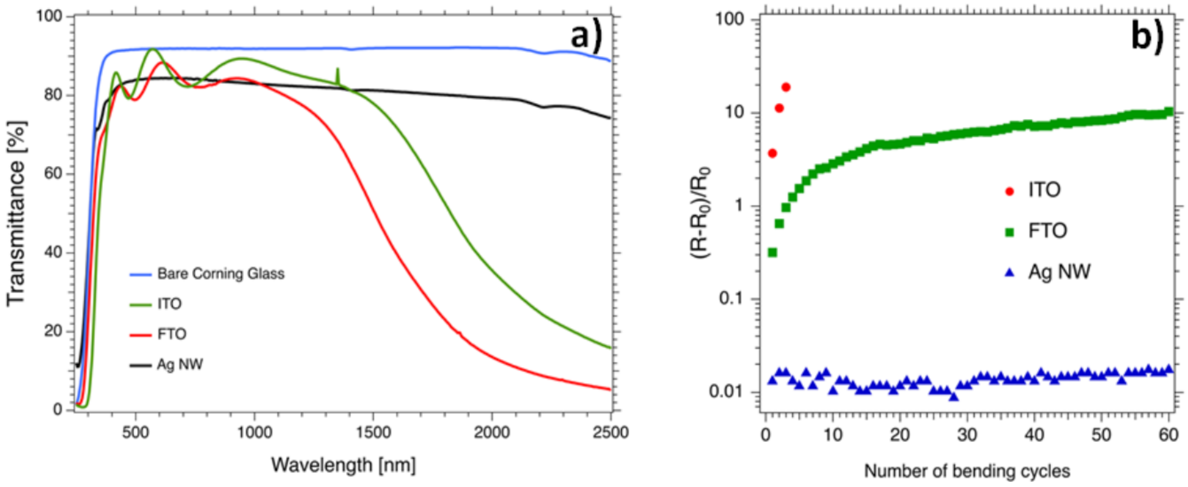

Figure 1.14: Comparison of the optical transmittance (a) and the relative electrical resistance under mechanical bending (b) of ITO, FTO, and AgNW. [43]

Although transparent electrodes based on silver nanowire networks exhibit excellent electrical and optical properties, extensive investigations devoted to MNW should still be performed. Their main drawbacks seem to be a lack of reproducibility and stability, which may stem from a too high temperature treatment, electrical failure, ageing, or a bad adhesion between the nanowires and the underlying substrate. Furthermore, the roughness of MNW may be at the origin of short circuits in systems made of multiple layers. From an economical point of view, it could be interesting to replace silver by a cheaper metal such as copper.

1.5.2 Technological applications

Regarding the integration of MNW networks in technological applications, we can firstly mention rollable touch screens. The working principle is the same as for capactive sensors: changes in capacitance when fingers interact with the electrode are converted into an electrical signal. MNW may also be used as transparent and flexible electrode in strain sensors or thin film transistors. Other devices, such as photovoltaic applications, light emitting diodes, transparent film heaters, and smart windows have attracted more attention in the literature and are therefore discussed below in more details.

Photovoltaic applications Photovoltaics is intensively studied to offer a sustainable green alternative to fossil fuel energy. The new trend is to develop cost-effective flexible transparent solar cells with abundant materials. As light must enter the solar cell, while photo-generated excess carriers must be collected by a conductive contact, transparent electrodes are a key component in solar cells. To meet the requirements, silver nanowires networks are serious candidates to compete with ITO. Several researches showed that AgNW can be integrated as top electrode is organic solar cells, while offering high transparency, low electrical resistance, a good energy conversion efficiency, and excellent bending capacities [44], [45], [46].

Another property of AgNW which must be taken into account is haziness. The haze factor, or simply haziness, refers to the degree of incident light scattered forward towards the active layers [47]. The presence of a silver nanowire network increases haziness and the photon absorption probability. This explains why AgNW-based solar cells offer good conversion performances compared to TCO. Nevertheless, AgNW are also at the origin of diffused reflection. People sitting next to a window equipped with this type of solar cells may feel a little discomfort due to light scattering if the haze factor is too large.

Light emitting diodes The architecture of Light Emitting Diodes (LED) is very similar to that of solar cells: the active layer is sandwiched between two electrodes. The challenge in LED is to supply charges in the active layer, while allowing light to escape the device when electron-hole pairs recombine. Generally, the top or the bottom electrode is transparent so that light is either emitted from the top surface (top-emitting LED) or through the bottom substrate (bottom-emitting LED). For transparent LED, both electrodes should be transparent.

Owing to their flexible properties, the majority of AgNW electrodes are integrated in Organic Light Emitting Diode (OLED). Like for solar cells, AgNW are often embedded in a polymer (polyvinyl alcohol, polyacrylate, PMMA, polyimide, etc.) to decrease surface roughness, prevent leakage currents, enhance adhesion with underlying layers, and increase mechanical stability [48], [49], [50].

Nevertheless, despite their cost-efficient, light-weight, and bio-compatible properties, organic devices have a much shorter lifetime than inorganic devices. Chemical, thermal, and electrical instabilities, which are for example due to oxidation, thermal crystallization of organic molecules, or diffusion of metallic ions in the sandwich structures of OLED, can lead to irreversible degradation of the device. Moreover, in comparison to inorganic light emitting diodes, OLED offer a relatively low luminance which in addition decreases with aging [2].

By contrast, inorganic light emitting diodes provide high brightness and a long life span, but they are mechanically rigid and brittle. Hence, the solution to make flexible devices using inorganic semiconductors is to deposit thin film layers, so that bending becomes possible. For instance, Jeong et al. [51] managed to deposit AgNW on GaN-based LED by a spin-coating method. This conclusive experiment indicates that AgNW are a promising alternative to TCO, even if they are not implemented on flexible substrates.

Transparent film heaters Historically, Transparent Film Heaters (TFH) were one of the first applications of TCO. During World War II, they were used to defrost aircraft windscreens, enabling the aircraft to fly at much higher altitudes [52]. Nowadays, TFH are used for defrosting and defogging vehicle windows, mirrors, and outdoor panel displays. By virtue of their flexibility, scalability, limited fabrication cost, and possibility for heating at low voltage, AgNW are among the most promising materials for TFH applications [53],[54]. They are able to heat the film uniformly with limited power consumption and provide a fast thermal response. Their flexibility, eventually enhanced by embedding in a polymer, allows them to be integrated on surfaces with complex shapes, such as windscreens and helmet visors [55], [56], [57]. Polymer composite AgNW are used to improve the adhesion, thermal and electrical stability of silver nanowires. Like for photovoltaic applications in windows, the large haze factor of AgNW can be a problem for automobile windscreens. Uncontrolled scattered light may dazzle the conductor.

Smart windows Smart windows also make use of transparent electrodes. By regulating incident - sometimes dazzling - sunlight, they help improve energy efficiency, safety and comfort in buildings and vehicles. Electrochromic windows rely on electrochromic materials which can change their oxidation states, hence their transmittance properties, when subjected to electrical fields. Polymer-Dispersed Liquid Crystal (PDLC) devices make use of electric fields to align liquid crystals droplets so that the device is in its transparent configuration; otherwise light is scattered by the random dispersion of the droplets and the window turns opaque. Again, AgNW embedded in a polymer have been successfully integrated as transparent electrodes to provide the electric field required for modifying the window transparency [58], [59].

Closing remarks

The challenge in developing transparent optoelectronic devices is that a compromise must be made between optical transparency and electrical conductivity, since transparent materials are insulating in nature, while conductive materials appear opaque. The key point discussed in this chapter was the influence of the electronic band structure on the optical and electrical properties of materials.

Wide band gap materials exhibit a good transparency in the visible range, but a poor electrical conductivity. The solution to improve their conductivity is substitutional doping. This principle will be used in Chapter 6 to enhance the conductivity Cu_2O. The lack of p-type TCO is a good motivation to investigate the physical properties of this promising material.

The absence of a band gap in conductors is responsible for their good electrical conductivity, but restricts their optical transparency. To sidestep this conundrum, we will investigate how silver nanowire networks can combine both properties. Nowadays, TCO are the main transparent electrodes implemented in optoelectronic devices. However, the increasing demand for flexible electronics makes silver nanowire networks a topical subject.

Chapter 2

State of the art of AgNW networks

In view of applications, AgNW-based transparent electrodes should exhibit a sheet resistance below 100 Ω/sq and a transmittance above 90%. Therefore, a trade-off in nanowire density must be found to achieve a high conductivity without loosing transparency. Moreover, as for ultra-thin metallic films, the thinner the nanowires, the larger the electrical resistivity, but the better the transparency of the overall network. Finally, post-deposition thermal annealing has been shown to reduce the electrical resistance of silver nanowires networks without affecting their transparency.

This chapter aims to briefly present the influence of nanowire size, network density and thermal annealing on the optoelectrical properties of silver nanowire networks. Before addressing these topics, we explain how silver nanowires are fabricated by polyol synthesis and how random nanowire networks are obtained by spin coating. We also give a brief introduction to percolation theory.

Contents

2.1 Polyol synthesis of silver nanowires

By definition, silver nanowires are nanostructures with an aspect ratio greater than 10. The dimensions of commercially available silver nanowires generally range from 50 nm to 200 nm in diameter and from 5 μm to 50 μm in length. Silver nanowires are composed of silver atoms, but the crystal form can vary from one fabrication method to another. They may be composed of a single silver crystal, or of multiply twinned crystals.

During the 21st century, numerous techniques - such as UV light irradiation methods, hard template methods, and soft template methods - have been developed to synthesize silver nanowires [60]. As its name suggests, the UV light irradiation method relies on the photodecomposition of silver nitrate ($AgNO_3$) under UV irradiation [61]. The difference between the hard and soft template method is that nanowires formed by soft templates are dispersed in solution, whereas nanowires prepared with prefabricated hard templates are immobilized in an ordered solid structure. In other words, the size of the nanowires prepared with hard templates can be varied by controlling the pore size of the solid material, while the dimension of nanowires synthesized by a soft template method depends on the reaction rate in solution.

The problem with UV light irradiation and hard template is that these methods are not scalable, limiting their industrial applicability. Moreover, due to the complex procedure to extract nanowires from the hard template, the latter method is not suited for the production of nanowires with high aspect ratios [62]. Among other silver nanowire production techniques, solution-based polyol synthesis seems to be the most promising method regarding its simplicity, reproducibility and morphological controllability. Moreover, this method is time-saving, low-cost, environmental friendly, and adaptive to mass production.

Polyol synthesis of silver nanowires can be obtained by injecting silver nitrite ($AgNO_3$) dropwise in a Polyvinylpyrrolidone (PVP)-Ethylene Glycol (EG) solution. Whereas $AgNO_3$ dissolved in EG provides a source of silver atoms, PVP ensures growth control of silver nanowires. Selecting an appropriate concentration of $AgNO_3$ and PVP, injection rate, and reaction temperature are the key factors to achieve silver nanowires with a long aspect ratio [60]. These parameters should ensure the formation of 5-fold multiply twinned silver particles (decahedral shape) and avoid the appearance of spherical or cubic nanoparticles. In the case of spherical and cubic nanoparticles, PVP is homogeneously distributed over all surfaces, so that each reduced silver atom can be deposited randomly on any part of the surface. The growth is thus isotropic because there is no preferential configuration to minimize the surface energy. By contrast, as depicted in Figure 2.1b, 5-fold twinned particles grow preferentially in the longitudinal direction since PVP chains interact more strongly with the crystallographic $\{1\ 0\ 0\}$ planes than the $\{1\ 1\ 1\}$ planes, resulting in the inhibition of the lateral growth and the formation of nanowires [63].

When the nanowires are exposed to electron beam for a longer time, we observe a bright ring around their pentagonal cross section. This is caused by charge accumulation on the surface and indicates that the nanowires are surrounded by an insulating PVP layer. Besides preventing lateral growth by passivating the side surfaces, the role of the PVP layer is to prevent agglomeration of silver nanowires after their synthesis.

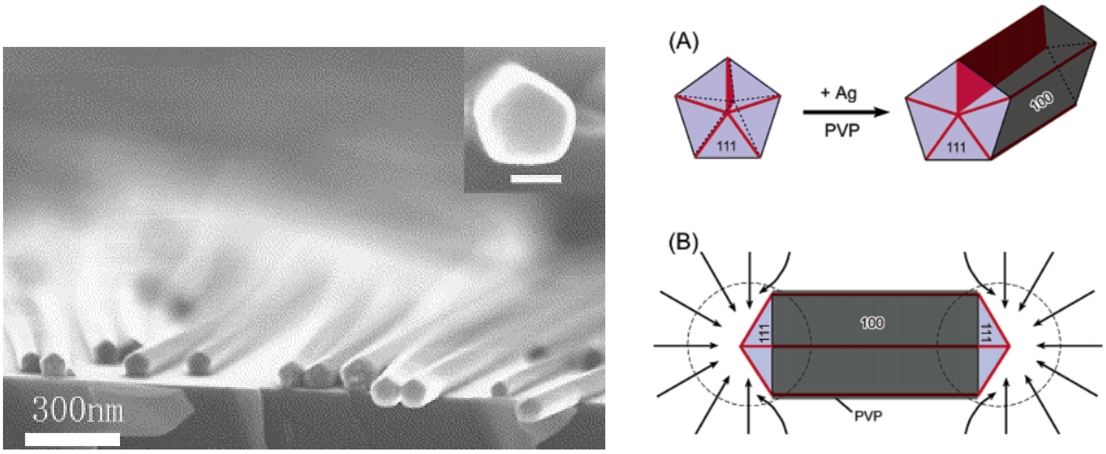

(a) SEM image (b) Schematic illustration

Figure 2.1: The SEM image on the left-hand side shows the pentagonal cross section shape of silver nanowires [64]. The scale bar in the inset is 60 nm. The schematic illustration on the right-hand side shows the growth directions of multiply twinned nanoparticles [63]. The {1 0 0} planes covered by PVP are displayed in dark gray. They prevent lateral growth. The arrows indicate the migration of silver atoms towards the {1 1 1} end-planes shown in light gray.

2.2 Spin coating of silver nanowires

Spin coating has been used for decades to deposit thin films. Its process, which exploits the centrifugal force to spread the solution radially on the substrate, is illustrated in Figure 2.2. Firstly, a controlled amount of solution is dispensed on a static or spinning substrate. Then, as soon as the substrate is rotating, excess solution is thrown off. Finally, the rotation is prolonged at a constant speed to ensure a homogeneous film thickness. Further thinning of the film is still possible due to evaporation of the solvent.

During the constant speed rotation, a thin film remains on the substrate when the viscous force counterbalances the centrifugal force. From the balance between viscous and centrifugal forces in the rotating frame, we can model the spin coating process [65]. The thinning of a Newtonian fluid on a rotating disk is then given by:

$$\frac{dh}{dt} = -\frac{2\rho\omega^2 h^3}{3\eta} - e, \tag{2.1}$$

where $h\,[\mathrm{m}]$ is the current film thickness, $\omega\,[\mathrm{s}^{-1}]$ is the angular velocity of the disk, $\rho\,[\mathrm{kg\,m^{-3}}]$ is the fluid density, $\eta\,[\mathrm{Pa\,s}]$ is the fluid dynamic viscosity, and $e\,[\mathrm{m\,s^{-1}}]$ is the evaporation rate. From (2.1), we observe that the main parameters affecting the final thickness of the film are the spin time, spin speed, viscosity, and amount of dispensed solution. External factors which come into play are temperature, pressure, and humidity, since they influence the evaporation rate of the solvent. Because subtle changes in these parameters can result in drastic variations of the coated film, repeatability is the most challenging task when using spin coating as thin film deposition method.

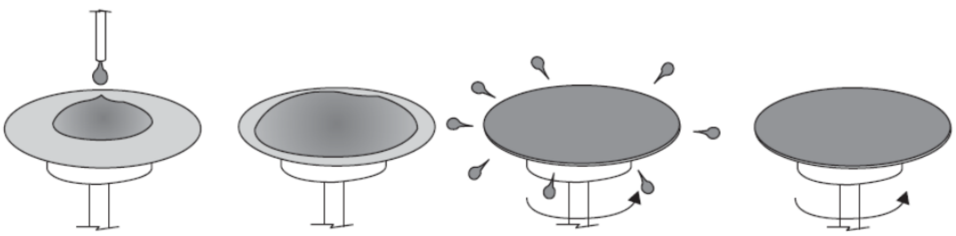

(a) Static

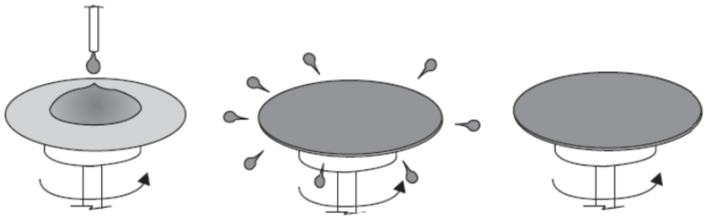

(b) Dynamic

Figure 2.2: Illustration of static and dynamic spin coating. In the static method, the solution is dispensed on a fixed substrate, whereas in the dynamic method the solution is deposited on a rotating substrate.

Even though a solution of silver nanowires can be considered a Newtonian fluid under sufficiently dilute conditions, spin coating an ink of nanowires is more complex than a homogeneous solution. Besides the spin speed and volume of dispensed solution, the drying time and drying conditions are critical to achieve a uniform and random dispersion of nanowires. For solvents like isopropanol, a spin coating time of 30 seconds generally suffices until the film is fully dry. By consequence, the time between dispensing the solution and the start of spinning can drastically influence the film quality.

To ensure a random dispersion of silver nanowires, the rotation speed should be relatively low; otherwise, nanowires tend to orientate radially due to the centrifugal force. Furthermore, the larger the rotation speed, the more solution is wasted due to radial ejection, especially for solutions with a low viscosity such as isopropanol. However, the rotation speed has to be high enough to spread the solution on the whole substrate before the solvent is lost due to evaporation. Therefore, a compromise must be made between nanowires random orientation and full coverage of the substrate.

The most important parameter that affects the quality of the silver nanowire network is probably the spin coating method used to dispense the solution. In the static deposition method, the ink is dispensed droplet by droplet while the substrate is stationary (Figure 2.2a). Once the desired volume has been deposited, the substrate is brought into rotation. The acceleration and final rotation speed can be tuned by the user to control the film thickness. In the dynamic deposition method, the substrate is already spinning at the desired rotation speed when the solution is dispensed (Figure 2.2b). Physical parameters that influence the choice of a static or dynamic spin coating method to achieve the best film quality are the viscosity and evaporation rate of the solvent, and the wettability of the substrate. A dynamic method should be preferred for solutions with a high viscosity, a high evaporation rate, and substrates with a hydrophobic character.

In terms of advantages, spin coating is a rapid, simple, and cheap method. Besides, it can be performed at room temperature and under atmospheric pressure. Nonetheless, the main problem of this method is that it is not suited to large scale production: only one substrate is treated at a time. Furthermore, 95% of the coating material is flung off the substrate during spinning [65]. Yet, at laboratory scale, spin coating is an efficient way to deposit coating material.

Alternatives to spin coating to fabricate silver nanowire networks are drop casting, spray coating, dip coating, and Meyer rod coating. Drop casting consists in dropping a solution onto a flat surface and waiting until the solvent evaporates. Like dip coating, this method is simple and fast, but makes it difficult to achieve a uniform coating with a controlled thickness. As its name suggests, spray coating relies on spraying a solution onto a substrate. This technique is cheap, fast, scalable, and applicable to curved surfaces, but does not allow to deposit nanowires with a long aspect ratio as they tend to break in the ultrasound nozzle or become stuck and clog the spray [52]. Finally, in Meyer rod coating, a rod is rolled over the drops to spread the solution evenly over the substrate, allowing a precise control of the film thickness. This method can be scaled up to a roll-to-roll process.

2.3 Percolation theory

To better understand the properties of silver nanowire networks, we firstly introduce the basic principles of percolation theory. Percolation can be defined as the formation of pathways through a system with as goal to connect one extremity of the system to another. Simple examples of percolation in everyday life are forest fire spreading and water infiltration into porous rocks. A percolating system consists of open and closed pathways. For instance, when silver nanowires are deposited on a surface, the open pathways are the air gaps and the closed pathways are the nanowires. Once enough silver nanowires have been deposited, a sufficient amount of closed pathways are connected together and the surface becomes conductive. The goal of percolation theory is to determine the threshold at which this phase transition occurs.

Percolation theory of nanowire networks is a complex topic because the nanowires are deposited randomly. By contrast to site percolation and bond percolation, where the positions of the sites that can be occupied are discrete (Figure 2.3), the possibilities to occupy sites in continuum percolation - e.g. in nanowire networks - are infinite. Moreover, while the number of neighbors in site percolation is finite; the coordination number in continuum percolation is infinite.

In the case of bond percolation in a unit square lattice, it is possible to show mathematically [67] that the critical density to have a continuous percolating pathway from one end of the lattice to the other is $n_c = 0.5$. For site percolation, Monte Carlo simulation programs [68] showed that the critical density was $n_c = 0.5927$. The percolation threshold of bond percolation is always lower than the percolation threshold of site percolation. Indeed, to create a pathway one bond but two neighboring sites are needed. Therefore, using nanowires instead of nanoparticles is more efficient, since less material is needed to obtain a percolating network.

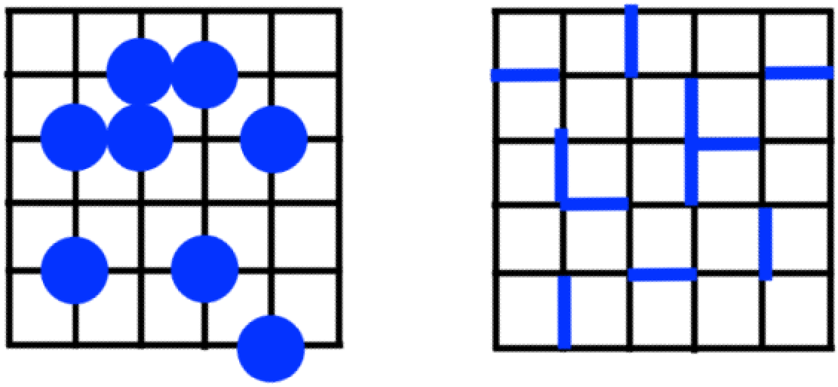

(a) Site percolation ($n_c = 0.5927$) (b) Bond percolation (n_c=0.5)

Figure 2.3: Illustration of site and bond percolation in a square lattice. In this example, the critical density of site percolation is an approximation and the critical density of bond percolation is exact. [66]

Due to the increased degrees of freedom in continuum percolation, numerical methods are required to approximate the critical density. It has been shown that the percolation threshold is decreased by increasing the degree of randomness in the system [69]. More precisely, allowing random orientations and different sizes of nanowires is expected do decrease the critical density. Li and Zang [70] developed an algorithm for Monte Carlo simulations to study the continuum percolation of randomly oriented nanowires of length L_{NW}. They showed that the critical density n_c [m^{-2}] for a 2D network of such nanowires is given by

$$n_c \simeq \frac{5.64}{L_{\mathrm{NW}}^2}, \tag{2.2}$$

provided the system size is at least 32 times larger than the nanowire length L_{NW} [m]. This equation already indicates that longer nanowires will provide a better FoM, because doubling the nanowire length divides the nanowire density required for percolation by a factor of four. The origin of this phenomenon is linked to the increased probability for longer nanowires to overlap, and therefore to create new conducting pathways.

2.4 Morphological properties of nanowire networks

Electrical and optical properties of nanowire-based transparent electrodes depend on the morphological properties of the network, i.e. on the nanowire network density and on the size of the nanowires. A sparse network is very transparent, but has a high electrical resistance; while a dense network is very conductive, but appears opaque. Similarly, nanowires with a large diameter are more conductive, but obstruct incident light. Therefore, a trade-off has to be considered for the fabrication of silver nanowire networks.

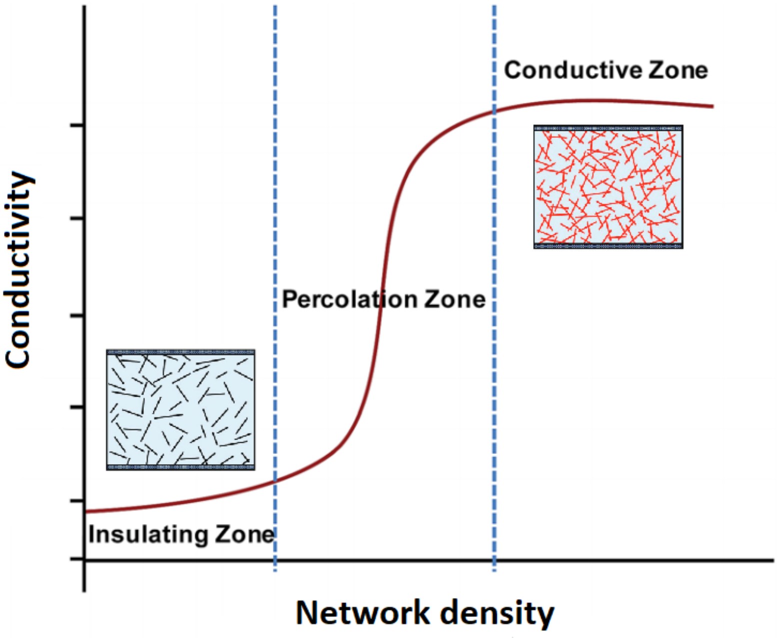

Figure 2.4: Illustration of the evolution of conductivity as a function of the nanowire network density. The transition between the insulating zone and the percolation zone depends on the critical density. Image adapted from [71].

2.4.1 Nanowire network density

As shown in Figure 2.4, the dependence of the electrical conductivity on the network density can be divided into three regimes. Below the critical density, the electrical resistivity of the network is considered as infinite; the network density is too small to create a continuous conduction path between both extremities of the network. For network densities $n \geq n_c$ (but still close to n_c to stay in the percolative regime) the electrical conductivity is given by the following scaling law

$$\sigma \propto (n - n_c)^{\gamma}, \tag{2.3}$$

where γ [-] is the conductivity exponent[1] reflecting the dimensionality of the system. For 2D continuum percolation systems, the universal conductivity exponent is $4/3$. It is not clear to which extend (2.3) is valid, but Bergin et al. [73] obtained a good fit to their experimental data up to $n = 12n_c$. As the network density is increased further, more conduction paths are formed; the conductivity of the network increases rapidly until a constant conductivity value is reached. However, increasing the network density lowers the optical transmittance. It has been shown experimentally that the relationship between the optical transmittance T and the nanowire network density n is linear [73]:

$$T \propto 1 - \alpha \frac{n}{n_c}, \tag{2.4}$$

where α [-] is a fitting parameter that accounts for the dimensions of the nanowires. Lagrange et al. [42] proposed a theoretical approach to predict the value of α.

---

[1] In practice, the experimental conductivity exponent deviates from the universal value due to a larger junction resistance compared to the bulk resistance of the nanowires. In that case, γ may be seen as a fitting parameter and a fundamental property of the network [72].

If f_{NW} [-] denotes the fraction of the substrate covered by nanowires, the transmittance of the nanowire network T can be written as:

$$\begin{aligned} T &= f_{\mathrm{NW}}\,(1-R_{\mathrm{sub}})\,T_{\mathrm{sub}}\,(1-R_{\mathrm{NW}})\,T_{\mathrm{NW}} + (1-f_{\mathrm{NW}})\,(1-R_{\mathrm{sub}})\,T_{\mathrm{sub}} \\ &= (1-R_{\mathrm{sub}})\,T_{\mathrm{sub}}\Big(f_{\mathrm{NW}}\,(1-R_{\mathrm{NW}})\,T_{\mathrm{NW}} + (1-f_{\mathrm{NW}})\Big) \\ &= (1-R_{\mathrm{sub}})\,T_{\mathrm{sub}}\Big(1-f_{\mathrm{NW}}\,(1-(1-R_{\mathrm{NW}})T_{\mathrm{NW}})\Big), \end{aligned} \tag{2.5}$$

where R_{NW} and T_{NW} are the average reflectance and transmittance of a single nanowire, and R_{sub} and T_{sub} are the reflectance and transmittance of the barge glass substrate. To simplify (2.5), the transmittance of the substrate can be written as a reference transmittance T_0 and the reflectance of a single silver nanowire R_{NW} can be assumed to be close to unity like for bulk silver. Injecting

$$T_0 = (1-R_{\mathrm{sub}})\,T_{\mathrm{sub}} \quad \text{and} \quad R_{\mathrm{NW}} = 1, \tag{2.6}$$

in (2.5) yields

$$T = T_0(1-f_{\mathrm{NW}}). \tag{2.7}$$

Using the average nanowire diameter D_{NW} [m] and length L_{NW}, the network density n, and the critical density n_c given by (2.2), the fraction of the substrate covered by nanowires can be written as:

$$\begin{aligned} f_{\mathrm{NW}} &= n\,D_{\mathrm{NW}}\,L_{\mathrm{NW}} \\ &= 5.64\frac{D_{\mathrm{NW}}}{L_{\mathrm{NW}}}\frac{n}{n_c}. \end{aligned} \tag{2.8}$$

Hence, (2.7) becomes

$$T \propto 1 - 5.64\frac{D_{\mathrm{NW}}}{L_{\mathrm{NW}}}\frac{n}{n_c}, \tag{2.9}$$

and by comparing this relationship with (2.4), we identify a theoretical expression for the fitting parameter

$$\alpha = 5.64\frac{D_{\mathrm{NW}}}{L_{\mathrm{NW}}}. \tag{2.10}$$

To find the best compromise between electrical conductivity and optical transmittance, we have to determine the network density n_{max} that will maximize Haacke's figure of merit. Since the sheet resistance is inversely proportional to the electrical conductivity, we have

$$R_s \propto \left(\frac{n}{n_c}-1\right)^{-4/3}. \tag{2.11}$$

Injecting (2.4) and (2.11) in (1.22), yields

$$\mathrm{FoM_H} \propto \left(1-\alpha\,\frac{n}{n_c}\right)^{10}\left(\frac{n}{n_c}-1\right)^{4/3}, \tag{2.12}$$

such that the network density $n_{\max}$ that maximizes $\mathrm{FoM_H}$ is given by

$$\begin{aligned}
\frac{\mathrm{dFoM_H}}{dn} &\propto \cancel{\left(1-\alpha\frac{n}{n_c}\right)^9}\cancel{\left(\frac{n}{n_c}-1\right)^{1/3}}\left(-10\,\alpha\left(\frac{n}{n_c}-1\right)+\frac{4}{3}\left(1-\alpha\frac{n}{n_c}\right)\right)=0\\
&\Longleftrightarrow -\frac{2}{3}\left(17\,\alpha\frac{n}{n_c}-15\,\alpha-2\right)=0\\
&\Longleftrightarrow n_{\max}=\frac{1}{17}\left(\frac{2}{\alpha}+15\right)n_c,
\end{aligned} \tag{2.13}$$

after rejecting the values that would give a zero optical transmittance and an infinite electrical sheet resistance.

2.4.2 Nanowire size

The critical density n_c reported in (2.2) only depends on the nanowire length because the diameter is secondary to the formation of percolation pathways. Nevertheless, the nanowire diameter D_{NW} does influence the electrical conductivity when the diameter approaches the mean free path of conduction electrons l_{b}. As shown by Bid et al. [74], the electrical resistivity of a single silver nanowire ρ_{NW} can be written as a function of the bulk resistivity of silver ρ_{b}:

$$\rho_{\mathrm{NW}}=\rho_{\mathrm{b}}\left(1+\frac{l_{\mathrm{b}}}{2D_{\mathrm{NW}}}\right), \tag{2.14}$$

where $l_{\mathrm{b}} \sim 50$ nm is the bulk mean free path of electrons in silver. Like for ultra-thin metallic films, when the diameter of the nanowire approaches the mean free path of the conduction electrons, surface scattering becomes important with respect to bulk scattering. Therefore, the thinner the nanowires, the larger the electrical resistivity.

By contrast, (2.9) indicates that thinner nanowires offer a better transmittance. Indeed, for a fixed nanowire density, the area covered by silver nanowires, which blocks incident light, increases with increasing diameter. Moreover, for a given area fraction covered by silver nanowires, decreasing the nanowire diameter allows to increase the number of nanowires, and the increased number of connections between nanowires offers a better conductivity. This is depicted in Figure 2.5. Consequently, as we had to find a trade-off for the nanowire density, we also have to make a compromise for the nanowire diameter.

Finally, both (2.3) and (2.9) predict that longer nanowires will offer a better conductivity and a better transmittance for a fixed nanowire network density. Indeed, we saw in (2.2) that doubling the length of the nanowires decreases the critical density required for percolation by a factor of four. Furthermore, a network of longer nanowires presents fewer junctions and thus a lower junction resistance than a network of short nanowires. This is the reason why a particular attention is devoted to the synthesis of ultra-long silver nanowires [75], [76]. Factors limiting the nanowire length are fabrication and deposition processes, flexibility, and the size of the substrates.

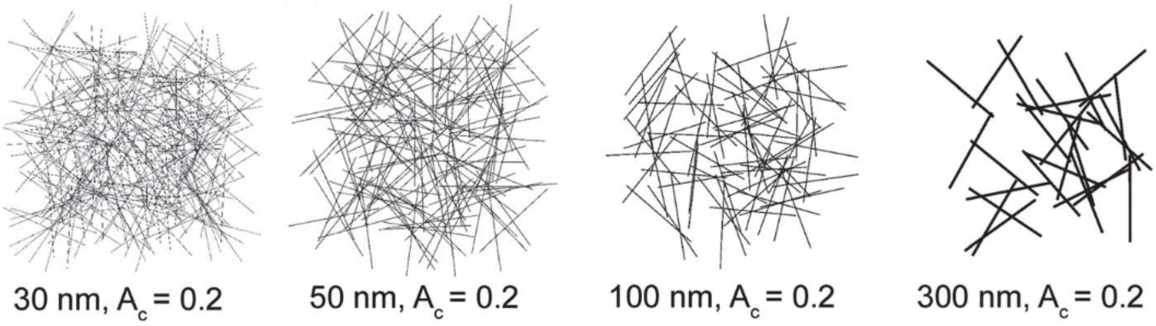

Figure 2.5: For a given area fraction A_c covered by silver nanowires, decreasing the nanowire diameter allows to increase the number of nanowires, the number of connections between nanowires, and thus the conductivity. [73]

2.5 Thermal annealing

Although the deposition of silver nanowire networks by spin coating is easy and cheap, it has a serious drawback that has not been detailed yet. To prevent aggregation of silver nanowires, they are encapsulated in PVP, a polymer used as a capping agent during the nanowire synthesis, and stored in isopropanol. Unfortunately, once the nanowires have been deposited by spin coating on the substrate, both compounds act as an insulating layer between the nanowires, causing bad electrical conductivity of the network. The resistance of two identical nanowires connected in series is not given by $R = R_1 + R_1$, as shown in Figure 2.6a, but by $R = R_1 + R_i + R_1$, where R_i is the contact resistance due to the presence of the insulating PVP layer (Figure 2.6b). When the nanowires are not in contact ($d > 0$), the contact resistance is considered to be infinite (Figure 2.6c).

In order to decrease the electrical resistance of silver nanowires networks without affecting their optical transmittance, post-deposition thermal annealing can be performed. This treatment has been extensively studied by M. Lagrange [42] and D. Langley [77] and will be discussed in this section. Other post-deposition methods that can be used to decrease the junction resistance are mechanical pressing [52], intense light treatment [78] [79], laser treatment, capillary-force induced cold welding [80], and gold coating [81]. In addition to improving the overall resistance of the network, junction welding also enhances their mechanical stability. Being able to withstand higher mechanical stresses upon bending is crucial for the implementation of AgNW-based electrodes in flexible optoelectronic devices.

2.5.1 Minimum resistance

M. Lagrange and D. Langley measured the electrical resistance of a silver nanowire network as a function of temperature from room temperature to 380°C with a continuous thermal ramp of 15°C/min. The results are shown graphically in Figure 2.7 and indicate that the resistance can be decreased by several orders of magnitude as long as the annealing temperature does not exceed a certain limit.

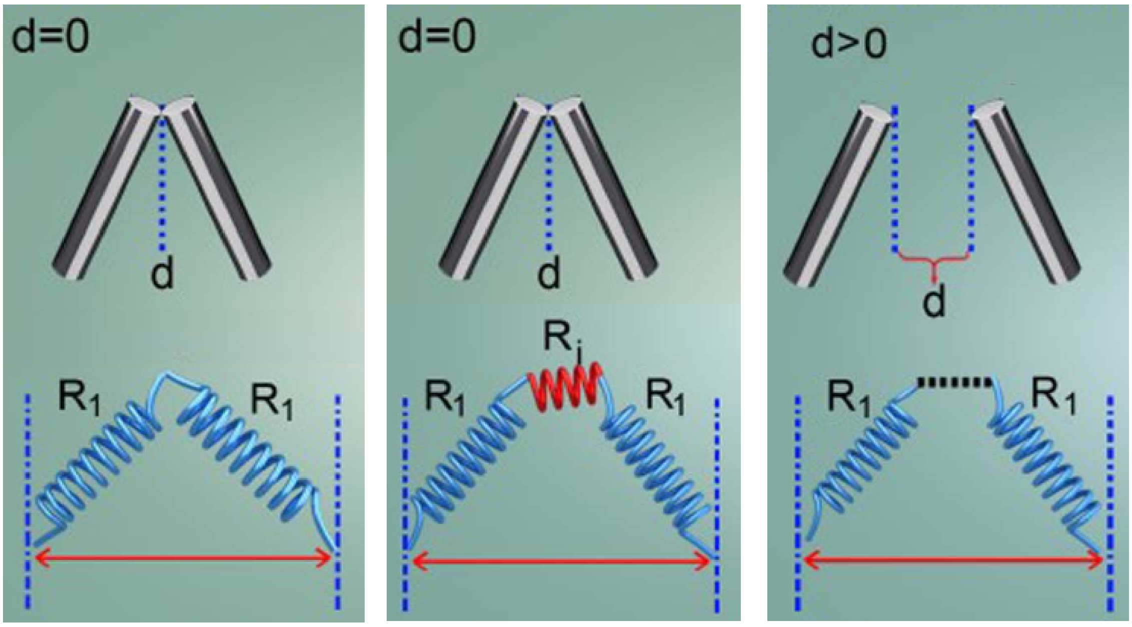

(a) $R = R_1 + R_1$ (b) $R = R_1 + R_i + R_1$ (c) $R = \infty$

Figure 2.6: Schematic illustration of the contact resistance between two nanowires. Ideally, when two nanowires are in contact ($d = 0$), the resistance of two identical nanowires in series is $R = R_1 + R_1$ (a). However, because the silver nanowires are encapsulated in an insulating PVP layer, the contact resistance R_i comes into play and increases the resistance of the nanowires in series (b). Finally, when the nanowires are further away from each other ($d > 0$), the electrical circuit is broken and the contact resistance is assumed to be infinite. Illustrations adapted from [82].

The effect of temperature on silver nanowires can be divided into three main stages. When silver nanowire networks are heated from room temperature to 200°C (a-c), the resistance decreases due to thermal desorption of isopropanol and PVP. Steplike drops in the resistance (b) highlight that the formation of new connection paths is a random process: the drop in resistance becomes visible when clusters of nanowires are connected together, allowing effective percolation through the network. Between 170°C and 270°C, the rate of reduction in electrical resistance is smaller because the concentration, hence the desorption rate of isopropanol and PVP has diminished.

A second phenomenon starts at 200°C (c): welding or local sintering at nanowire junctions can be observed in SEM images. This allows to decrease the contact resistance further, even after complete degradation of isopropanol and PVP. A minimum in resistance is observed between 300°C and 320°C (d), when sintering of all junctions is fulfilled.

Above 320°C (e), the resistance rises sharply. The network is deteriorated by morphological instabilities: the network looses its percolative nature due to the transformation of silver nanowires into droplets. This phenomenon is called spheroidization and is a result of the Plateau-Rayleigh instability, which will be discussed later.

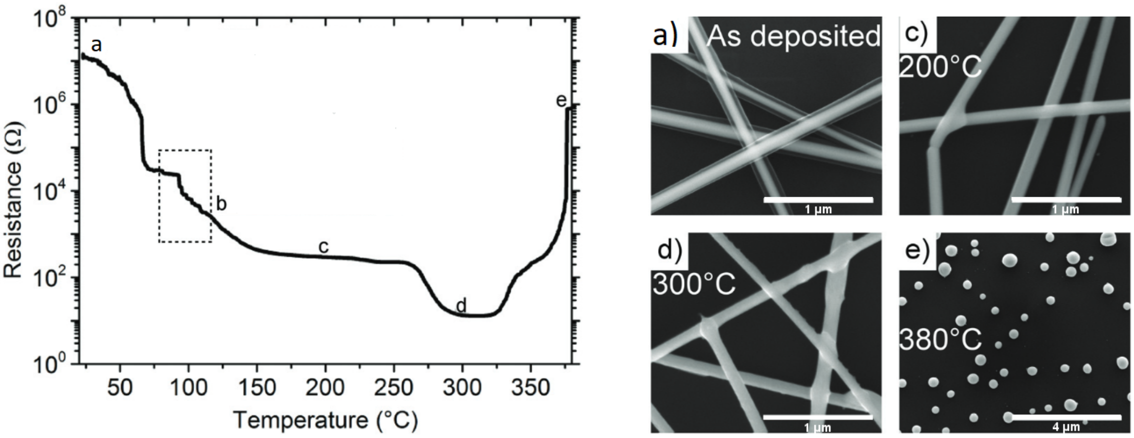

Figure 2.7: Electrical resistance and SEM images of silver nanowires during a continuous thermal ramp of 15°C/min from room temperature to 380°C. The average wire diameter is 105 nm and the average wire length is 37.3 μm. [77]

Instead of starting the continuous ramp anneal at room temperature, the silver nanowire network can first be subjected to an isothermal anneal (e.g. 100°C), and then subjected to a continuous thermal ramp up to 300°C. Whereas the first annealing mainly serves for the evaporation of isopropanol and PVP, the second annealing should allow welding of nanowires. Since both thermal desorption and local sintering provide a more intimate contact between nanowires, the conductivity of the network is enhanced. The advantage of this second method is that the minimum in resistance can be reached at lower temperatures than 300°C. For example, by pre-annealing a silver nanowire network at 200°C for 2 hours, there is no need to increase the temperature anymore since the sintering process has already reached completion [77].

2.5.2 Spheroidization temperature

Above a certain temperature, silver nanowires tend to spheroidize, but the resultant nanospheres are still aligned at the original position of the silver nanowires (Figure 2.7e). This morphological instability results from the tendency of any system with a larger surface to volume ratio to minimize its surface area in order to reduce its surface energy.

By analogy to silver nanowires, let us consider a liquid cylinder of average radius r_0 subjected to a sinusoidal perturbation of amplitude ε, such that the radius of the cylinder along its axis is given by

$$r(x) = r_0 + \varepsilon \sin\left(\frac{2\pi x}{\lambda}\right). \tag{2.15}$$

According to Plateau-Rayleigh instability, perturbations with wavelengths $\lambda > 2\pi r_0$ will grow in amplitude and lead to the fragmentation of the cylinder into spheres. The onset of instability is faster for cylinders with a smaller diameter, since atoms need to be transported over smaller distances before spheroidization occurs. A similar trend is observed for solid nanowires: nanowires with a smaller diameter exhibit a lower spheroidization temperature [77]. This is shown on the left in Figure 2.8, where the sharp increase in resistance appears at lower temperature for nanowires with a smaller diameter.

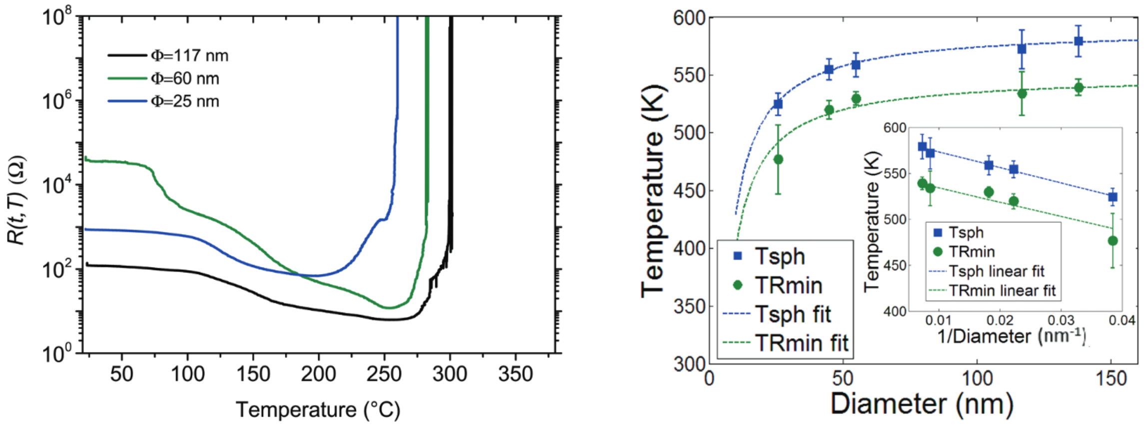

Figure 2.8: Impact of the diameter of silver nanowires on the temperature $T_{R_{\text{min}}}$ at which the minimum resistance occurs and on the spheroidization temperature T_{sph} at which a sharp increase in resistance is observed. The dashed fitting curves were obtained by using the Gibbs-Thomson model. [77]

2.5.3 Nanowire size and thermal annealing effects

The melting temperature of bulk silver is 962°C, but decreases dramatically for nanoparticles. This phenomenon is known as the Gibbs-Thomson effect. The deviation of the melting point from the bulk one is linked to the large surface to volume ratio of objects at small scales. As an example, for a sphere of radius R [m], the surface to volume ratio writes

$$\frac{S}{V} = \frac{4\pi R^2}{\frac{4}{3}\pi R^3} \propto \frac{1}{R}. \tag{2.16}$$

For a cylindrical nanowire, the surface to volume ratio is also inversely proportional to its radius R:

$$\frac{S}{V} = \frac{2\pi R L}{\pi R^2 L} \propto \frac{1}{R}, \tag{2.17}$$

where L is the length of the nanowire.

Starting from the equilibrium condition of a system comprising a solid and a liquid phase, it can be shown [83] that the melting temperature T_m [K] of a particle of radius R is given by:

$$T_{\text{m}}(R) = T_{\text{m}}^{\text{b}} \left(1 - \frac{2\, V_{\text{s}}^{\text{b}} \gamma_{\text{s}}}{L R}\right), \tag{2.18}$$

where T_{m}^{b} [K] is the bulk melting temperature, V_{s}^{b} [$\text{m}^3\,\text{mol}^{-1}$] is the molar volume of the solid phase, γ_{s} [$\text{N}\,\text{m}^{-1}$] is the surface energy, and L [$\text{J}\,\text{mol}^{-1}$] is the molar latent heat of melting. This equation is called the Gibbs-Thomson equation and relates the melting temperature of an object to its size.

By analogy to the Gibbs-Thomson effect on the melting point of nanoparticles, Langley et al. [77] showed that the minimum resistance and onset of spheroidization occur at lower temperatures for thinner nanowires. Furthermore, they noticed that the decrease in temperatures $T_{R_{\text{min}}}$ [K] and T_{sph} [K] with respect to the "bulk" values associated with larger diameters exhibits good agreement with the Gibbs-Thomson equation (Figure 2.8).

The same characteristic length

$$l_c = \frac{2\,V_\mathrm{s}^\mathrm{b}\,\gamma_\mathrm{s}}{L} = 1.42\,\mathrm{nm} \tag{2.19}$$

has been used to fit the experimental data since the physical origin of junction sintering and spheroidization is the same; the driving force for both phenomena is atomic diffusion in order to reduce surface energy.

The optimized annealing temperature and duration depend on the nanowire morphology and the nanowire density. The thinner the nanowires, the lower the temperature at which thermal annealing should be performed to avoid spheroidization of the network. However, the temperature should be sufficiently high to ensure thermal desorption of isopropanol and PVP. The presence of the substrate may also influence the thermal stability of the nanowires.

F. Balty, MSc student at SPIN Lab, studied at which temperature the minimum resistance occurred for silver nanowires[2] with an average diameter of 200 nm and a length varying between 0.5 and 100 μm. After a static spin coating of 6 × 5 drops, with a waiting time of 30 seconds between each series of drops, the samples have been pre-annealed at 80°C for 30 minutes. Then, the temperature was increased by steps of 20°C up to 320°C, with a waiting time of 2 minutes at each step. The electrical resistance measured at each temperature step is shown in Figure 2.9. The minimum in resistance (195 Ω) is achieved at 280°C, once solvent desorption and sintering are complete. Because the maximum temperature that can be provided by the hot plate is 350°C, spheroidization of the silver nanowire network leading to a sharp rise in resistance could not be observed.

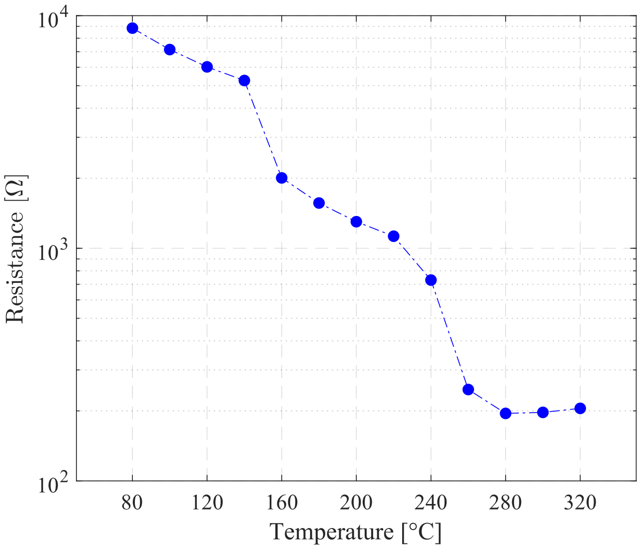

Figure 2.9: Electrical resistance of silver nanowires deposited on glass during a stepwise thermal ramp from 80°C to 320°C, after isothermal annealing at 80°C during 30 min. The minimum in resistance is achieved at 280°C.

---

[2] A solution of silver nanowires with the same dimensions will be used in this work.

Concluding remarks

In this chapter, we saw that the main parameters influencing the optoelectrical properties of silver nanowire networks are the nanowire network density, the nanowire length, and the nanowire diameter. Exploiting Haacke's figure of merit allows to determine which nanowire network density should be used to obtain the best compromise between optical transparency and electrical conductivity.

Once these parameters have been chosen, fabricating the network is the most critical part to achieve randomly dispersed nanowires. In a spin coating process, the rotation speed, volume of dispensed solution, drying time and dispensing method (static/dynamic) are the most important parameters that will affect the quality of the network. We will mainly focus our study on comparing the static and dynamic deposition method in Chapter 5. Another parameter to which more attention should be given is the hydrophilicity or hydrophobicity of the substrate. This topic will be discussed in Chapter 6.

To prevent the aggregation of silver nanowires once they are stored in isopropanol, the nanowires are encapsulated in an insulating PVP layer. A post-deposition treatment is necessary to decrease the junction resistance once the nanowires have been spin coated, otherwise the network does not conduct. Therefore, a post-deposition thermal annealing will be performed, since this is a fast, cheap, and easy method. The hurdle in this process is to sufficiently heat the substrate in order to remove the PVP layer, while not overheating the network, as this may lead to spheroidization and a sharp increase in resistance.

Chapter 3

Thin Film Deposition of Cuprous Oxide

Although perovskite and organic semiconductors receive more and more attention in scientific papers, copper-based semiconductors are far from being obsolete. One of the main reasons why copper oxides are still studied in view of photovoltaic applications is their sustainability: both copper and oxygen are abundant elements. Furthermore, copper oxide is non-toxic and low cost [84]. Besides, copper oxides can be both p-type and n-type semiconductors: cuprous oxide (Cu_2O) is p-type with a bandgap of 2.1 to 2.6 eV [85], whilst cupric oxide (CuO) is n-type with a bandgap of 1.9 to 2.1 eV [86], depending on the fabrication method. As a consequence of this difference in bandgap, CuO absorbs at wavelengths throughout the whole visible spectrum, hence appears brown, while Cu_2O looks more yellowish. In view of developing transparent solar cells or transparent light-emitting diodes, Cu_2O is thus the most suited type of copper oxide. However, despite the study of various fabrication techniques, obtaining a thin film with a single phase of Cu_2O and good optical and electrical properties is still a challenge [86].

In this chapter, we firstly introduce typical thin film deposition methods. We explain how to distinguish Physical Vapor Deposition (PVD) from Chemical Vapor Deposition (CVD) methods. Then, among the PVD techniques, we briefly mention the difference between thermal evaporation, electron-beam (e-beam) evaporation, and sputtering. Particular attention is devoted to RF magnetron sputtering because this method is well suited for the deposition of Cu_2O. To explain this deposition method in detail, we firstly describe the physical phenomena governing Direct Current (DC) and Alternating Current (AC) sputtering. RF magnetron sputtering relies on the same principles but in addition to an electric field, it involves a magnetic field to increase the deposition rate and the thin film quality. To end this chapter, we mention the sputtering parameters than can influence the quality of the deposited Cu_2O film based on a bibliographic research.

Contents

3.1 PVD and CVD methods

A thin film can be defined as a layer with thicknesses less than several microns grown by condensing atoms, ions or molecules one-by-one on a substrate [87]. The properties of thin films, such as film thickness, film roughness, chemical composition, defects, crystal size, and crystal orientation, are governed by the deposition method and the growth conditions. Consequently, the mechanical, electrical, and optical properties of thin films also depend on the deposition conditions. Besides the deposition technique, some parameters which can be tuned to modify the thin film properties are the substrate temperature, the chamber pressure, the process gas and the deposition rate. Additive thin film deposition methods can be divided into several categories: PVD, CVD, and chemical solution-based methods. A non-exhaustive list of typical deposition methods is shown in Figure 3.1.

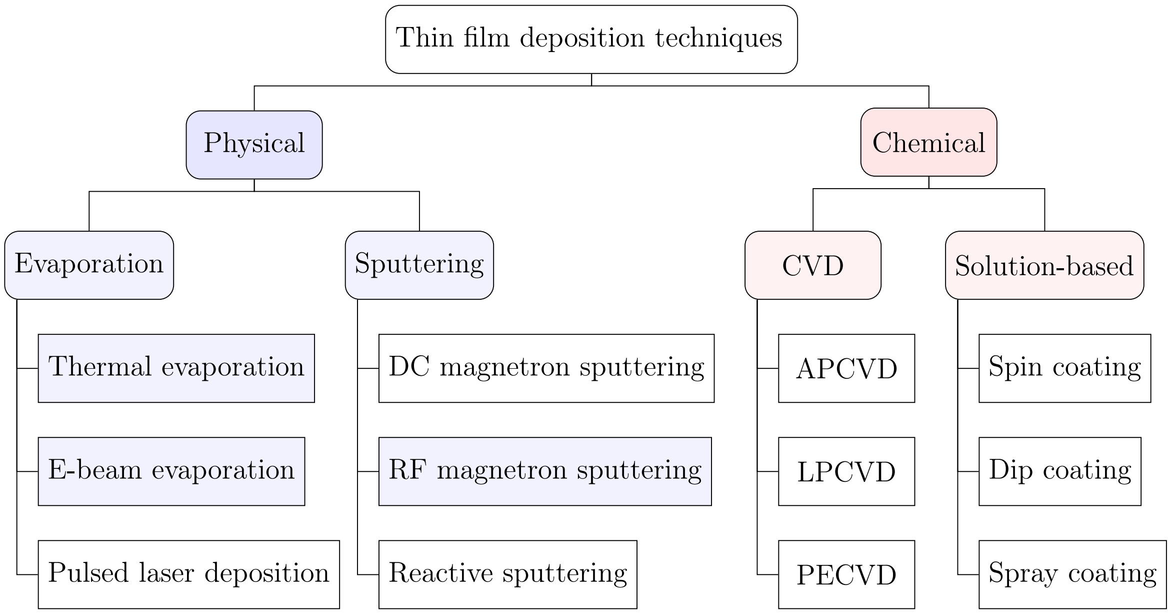

Figure 3.1: Non-exhaustive list of thin film deposition methods. Evaporation and sputtering deposition methods belong to Physical Vapor Deposition (PVD). APCDV, LPCDV, and PECVD stand respectively for Atmospheric Pressure, Low Pressure, and Plasma Enhanced Chemical Vapor Deposition.

Whereas PVD relies on molten or solid sources, CVD makes use of gaseous precursors to initiate chemical reactions in the gas phase and at the substrate surface. Non-volatile products resulting from the reactions deposit on the substrate, while eventual by-products are removed by gas transport through the reaction chamber. Both methods have advantages and drawbacks. CVD does not require a high vacuum environment and the chemical composition of the film is easily varied by monitoring flow rates of precursors [88]. Furthermore, high precursor flow rates allow to reach higher deposition rates than PVD. However, CVD methods require high deposition temperatures (300°C to 1000°C) and specialized precursors. Besides, some precursors and by-products are toxic, corrosive and flammable, making them harder to handle. Keeping in mind the demand for flexible optoelectronic devices, we will focus on PVD techniques which can be performed at lower temperatures and are therefore compatible with flexible substrates like plastic.

PVD processes can be split into vacuum evaporation and sputtering, but the thin film growth method is similar. At first, a chamber is evacuated to high vacuum to minimize the number of potential contaminants (vapor, dust, residues of previous evaporation processes). Then, a source material is either heated above its melting point to achieve evaporation, or subjected to highly energetic particles to dislodge atoms from the surface. Finally, the liberated atoms travel through the vacuum environment and deposit onto a substrate to form a thin film. High vacuum is needed to increase the mean free path of the evaporated atoms and avoid collisions with contaminants. The deposition rate depends on the evaporation rate - which is dictated by the source temperature, the chamber pressure, and the molar mass of the source material - the source geometry, and the position of the source relative to the substrate [89].

In both cases, a quartz balance is used to continuously record the film thickness during the deposition. The source material is deposited simultaneously onto the substrate and onto a quartz crystal placed in a resonant circuit. The additional mass resulting from the deposition process modifies the quartz resonant frequency

$$\omega_{\mathrm{mec}} = \sqrt{\frac{k}{m}}, \tag{3.1}$$

where m [kg] is the mass of the quartz and the deposited layer and k [$\mathrm{N\,m^{-1}}$] is its stiffness. Because any change in the quartz mechanical resonance frequency modifies the electrical resonance frequency of the circuit, the mass of the deposited layer can be deduced by tracking the changes in the electrical signal [90]. Knowing the mass, the density of the deposited material and the area of the crystal exposed to the source, we can deduce the thickness of the deposited thin film.

3.2 Comparison of some PVD methods

The main difference between thermal evaporation, e-beam evaporation and sputtering is linked to how atoms acquire enough kinetic energy to travel from the source material to the substrate where they will form a thin film. In order to initiate thermal evaporation, thermal energy must be supplied to a crucible or boat containing the source material to be deposited. One frequently used method is to pass a high current through a resistive tungsten wire wound around the crucible or to pass the high current directly through the resistive boat, so that thermal energy is generated by Joule heating. Once the atoms of the source material acquire enough energy to evaporate, they travel through the high vacuum chamber to finally condensate on the substrate.

During an e-beam evaporation process, current is passed through a tungsten filament which leads to joule heating and electron emission [91]. These liberated electrons are accelerated by high voltage and focused towards the source material by a strong magnetic field. Upon arrival, the energy of the e-beam is transferred to the source material, causing it to evaporate and eventually deposit onto the substrate after traveling through the vacuum chamber. A schematic of both resistive thermal evaporation and e-beam evaporation is illustrated in Figure 3.1.

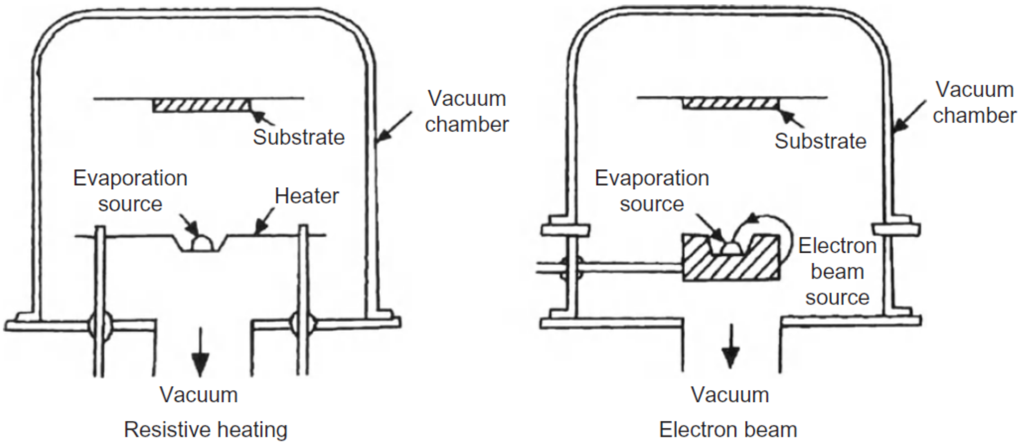

Figure 3.2: Schematic of vacuum evaporation chambers. [87]

Thermal evaporation is commonly used to deposit gold, aluminum, and copper as electrode material in optoelectronic devices [92] because this method is cheaper than electron-beam (e-beam) evaporation. However, the latter shows an important advantage: it allows to evaporate source materials with a much higher melting point, broadening the range of to be deposited materials. Furthermore, problems with resistive thermal evaporation include contamination of the molten source due to harmful reactions occurring between the source material and the heated crucible, making it difficult to deposit thin films with high purity. Finally, thermal evaporation of compounds is only possible if the constituents have similar vapor pressures.

In contrast to evaporation methods, sputtering does not rely on the absorption of thermal energy by the source material, but on the ejection of source atoms by bombarding the source/target with high energy ions. The momentum transfer from the ions to the surface atoms can impart enough energy to liberate/sputter the surface atoms. Once ejected, these atoms can travel to the substrate and deposit as a film.

The disadvantage of evaporation methods is related to the low energy of the evaporated atoms (0.1-0.2 eV), while sputtered atoms typically achieve energies around 10 eV. The energy of the atoms in the gas phase plays an important role in the quality of thin films. 2D ordered monolayers can only form if the incident atoms have enough energy to diffuse along the substrate surface. Atoms with little energy are not able to move over long distances: they lead to the creation of voids and increase surface roughness. By contrast, energetic atoms rearrange themselves during the deposition and improve crystallinity [93]. To better understand why this parameter plays an important role in the quality of thin film, we must study the adsorption processes at play when atoms or molecules in the gas phase interact with the solid surface of the substrate (Section 3.3).

These considerations lead to the conclusion that resistive thermal evaporation is not suited for the deposition of metal oxides, like Cu_2O, because they exhibit a high melting temperature. Furthermore, to obtain high quality films with a good crystallinity it is preferable to use sputtering instead of e-beam evaporation. When we look at Scanning Electron Microscope (SEM) images, isotropic grains, thin grain boundaries and the absence of voids are a proof of good crystallinity. Eventually, improving crystallinity leads to better mechanical, optical, and electrical properties of the thin film.

3.3 Adsorption processes

Even though neutral molecules have a zero net charge, they are attracted to each other by weak electrostatic forces, called van der Waals forces. These attractive interactions can be divided into three categories [6], [83]:

- Keesom forces resulting from the interaction between two permanent electric dipoles, i.e. two polar molecules.
- Debye forces occurring between a permanent electric dipole and an induced dipole. The electric field generated by the polar molecule induces an electric dipole in the non-polar molecule, resulting in an attractive force between both molecules.
- London forces resulting from the attraction between two induced electric dipoles. Because the electron cloud around the positively charged nucleus can be distorted by charge fluctuations, temporary dipoles can be induced in two non-polar molecules brought near each other.

Whatever the type of molecule, London forces, hence van der Waals forces, are always present. Otherwise, compounds would not bond together. However, as the interatomic distance decreases to the order of 1Å, the force between atoms becomes repulsive because electron clouds electrostatically repel each other. Moreover, as electrons must obey the exclusion principle, electrons in overlapping orbitals are forced to occupy higher energy states, leading to an increase in the potential energy of the system.

A common model to describe the potential energy U [eV] for a system of two atoms is the Lennard-Jones potential, depicted in Figure 3.3 and represented by the following expression:

$$U(r) = -\frac{A}{r^n} + \frac{B}{r^m}, \qquad (3.2)$$

where r [m] is the interatomic distance between the two atoms, A, n are parameters associated with the attractive force, and B, m are parameters associated with the repulsive force [6]. Empirically, it is found that $n = 6$ and $m = 12$, so that at small separation distances the net force is repulsive because the second term becomes dominant. At the equilibrium separation distance, the attractive and repulsive forces balance each other. The potential energy is minimum and the system of two atoms is in a stable configuration.

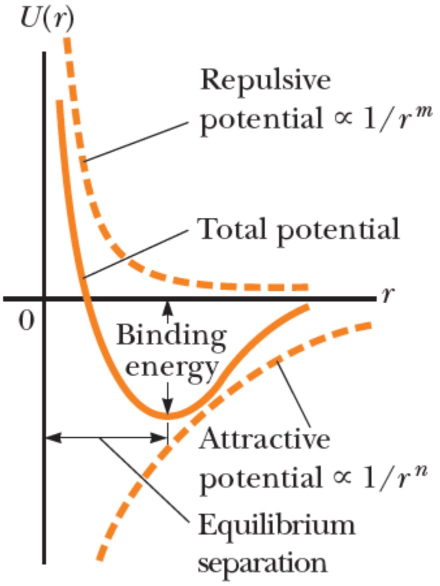

Figure 3.3: Potential energy as a function of the interatomic distance for a system of two atoms. [6]

Similarly, Van der Waals forces are responsible for attractive forces between an atom in the gas phase and the solid surface of the substrate. However, relying on the method of images, it can be shown that the dependence of the attractive potential as a function of the distance between the atom and the solid surface is r^{-3}, instead of r^{-6} for a system of two atoms [93]. Therefore, to avoid confusion, we will call this modified potential the physisorption potential. In general, physisorption potentials are characterized by a low binding energy (10 to 100 meV) and a large equilibrium separation of 3 to 10 Å with respect to the solid surface located at $r = 0$ (Figure 3.3).

Since at room temperature the thermal energy of atoms is $k_B T \sim 25$ meV, the physisorption potential well is not deep enough to strongly bind atoms to the surface. Adsorption of atoms on the substrate surface is explained by the presence of covalent adsorption bonds, similar to covalent bonds between atoms. In a covalent bonding, valence electrons are shared by the two atoms. When the atoms are brought close to each other, electron wave functions overlap, so that the probability to find electrons halfway between the atoms is larger than on the outer regions of the system. On average, the negative charge in between the atoms acts as an attractive force on the positive nuclei. Orbital overlaps in covalent bonds lead to a chemisorption potential characterized by a high binding energy (1 to 10 eV) and a short equilibrium separation of 1 to 3 Å with respect to the substrate surface [93].

Bringing the physisorption potential and the chemisorption potential together, we can draw the energetic landscape seen by an atom in the gas phase when it reaches the substrate surface. This is shown in Figure 3.4. Atoms with enough kinetic energy can surmount the energy barriers and adsorb directly in the chemisorbed states. Less energetic atoms are trapped in the physisorbed states. If the substrate is heated, atoms acquire enough energy to hop from one site to the neighbor site, allowing them to perhaps reach chemisorbed states. However, because the potential wells of physisorbed states are shallow, atoms may re-evaporate.

In conclusion, by hopping from physisorbed to chemisorbed states in quest of energy minima, atoms rearrange themselves during the deposition and improve crystallinity. Hence, by increasing the energy of the incident atoms and increasing the substrate temperature, crystallization of the thin film can be enhanced. Annealing the substrate to higher temperatures after deposition is also a solution to improve crystallinity.

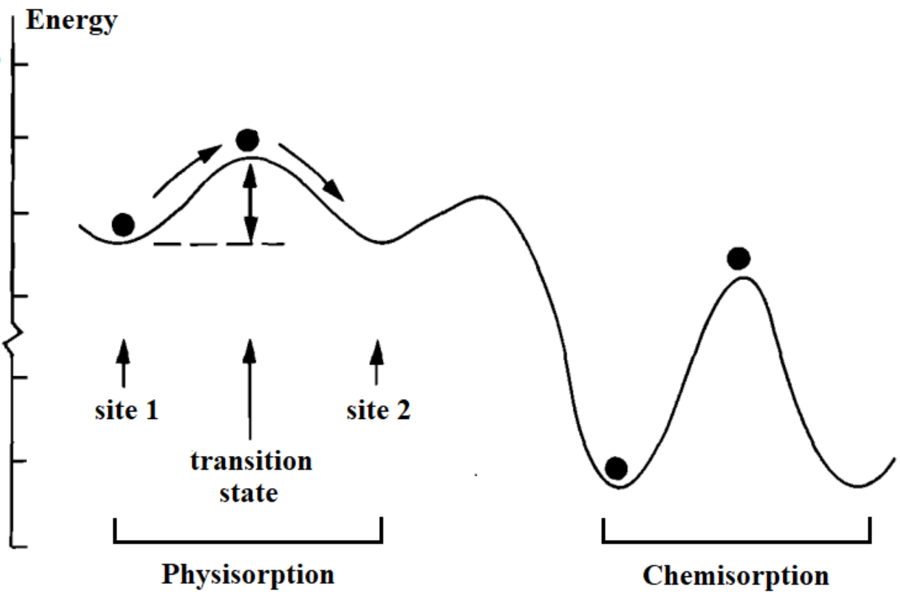

Figure 3.4: Energy landscape seen by a atom in the gas phase reaching the substrate surface. If the incoming atom has enough energy to surmount the energy barriers, it can adsorb directly into the chemisorbed state. If the substrate is heated, atoms can diffuse from one site to another by hopping over the energy barriers. Adapted from [94].

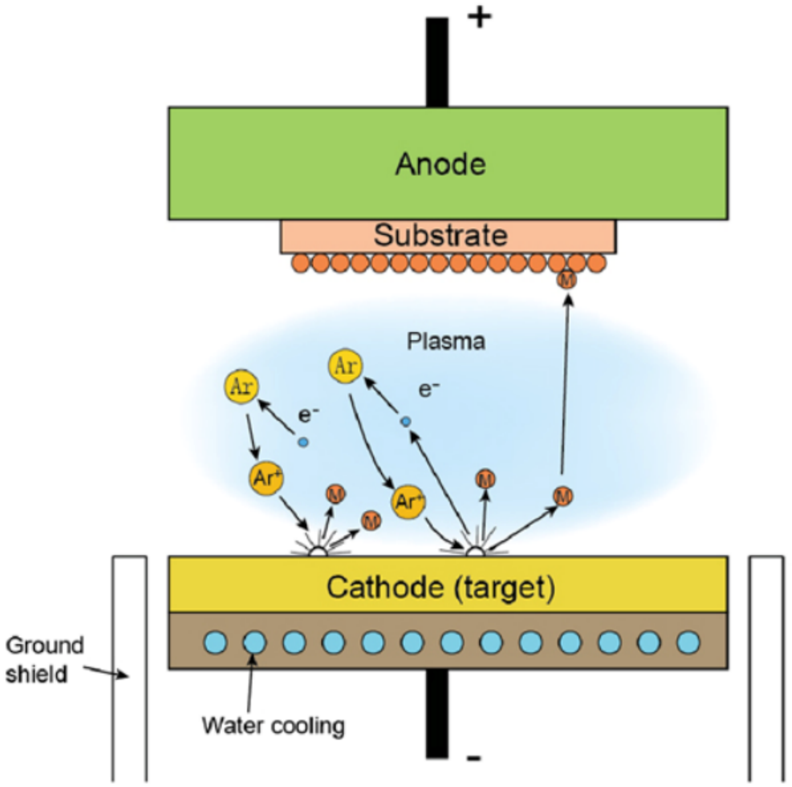

Figure 3.5: Schematic of the sputtering deposition method. [95]

3.4 DC and AC sputtering

As depicted in Figure 3.5, a sputtering chamber consists of a pair of parallel electrodes subjected to several kilovolts. While the source material/target is fixed to the cathode connected to the negative terminal of the power supply, the substrate is attached to the anode connected to the positive terminal. Because high voltage/power generates Joule heating, a cooling system is mounted below the target to avoid melting of the source material. It is also possible to cool or heat the substrate.

After evacuation of the chamber to reach high or ultra high vacuum ($< 10^{-7}$ Torr), a working gas (typically argon) is introduced to initiate and sustain a plasma, i.e. a gas of charged particles (electrons, ions and neutral atoms). Plasma generation starts with the acceleration of a stray electron from the negatively biased cathode to the positively biased anode. If this electron gains sufficient energy, a positively charged ion (Ar^+) will be created when the electron (e^-) collides with a neutral gas atom (Ar):

$$\mathrm{Ar} + \mathrm{e}^- \longrightarrow \mathrm{Ar}^+ + 2\mathrm{e}^-. \tag{3.3}$$

The extra electron is also accelerated and will in turn generate more ions and electrons. This snowball effect causes the gas to breakdown: a small current is able to flow through the initially insulating gas at a critical applied voltage. The breakdown voltage V_B [V] is a function of the chamber pressure P [Pa] and the distance d [m] between the anode and the cathode:

$$V_B(Pd) = \frac{APd}{\ln(Pd) + B}, \tag{3.4}$$

where A and B are constants depending on the nature of the gas. This relationship is called the Paschen's law [89]. At high pressure, above Paschen's minimum, the electrons do not gain enough energy between two collisions to produce ionization. A higher voltage must be applied to reach breakdown voltage. At low pressure, beneath Paschen's minimum, the electrons are very energetic but the probability of hitting atoms is low. Again, a higher voltage is needed to reach breakdown. If the voltage is increased above breakdown voltage, the plasma begins to glow and the current density becomes uniform, meaning that there are enough ions and electrons to sustain the plasma. Because any power supply can only provide a finite amount of energy, controlling the working gas pressure and the distance between the electrodes is important to initiate and sustain the plasma.

Once the plasma has been initiated, positive ions are accelerated towards the negatively biased cathode, located directly behind the target. As soon as ions collide with the target, atoms are ejected with enough kinetic energy to reach the surface of the substrate. Sputtering often utilizes inert gas ions such as Ar^+ to avoid undesirable reactions with contaminants or with the target atoms. Moreover, since argon atoms have a high molecular weight, the probability of ejecting atoms from the target is increased, leading to higher deposition rates. In addition to the constraints to sustain the plasma, the argon pressure should not exceed a certain limit because the kinetic energy of atoms incident on the substrate decreases with increasing argon pressure due to a higher scattering probability.

Several power delivery systems can be used for sputtering; a DC power source is used for conducting targets, whereas an AC power source is used to deposit insulating materials [96]. Sputtering of insulating materials cannot be done with DC power because these materials have a large DC impedance. Consequently, extremely high voltages would be required to maintain a plasma, and the target would be subjected to electrostatic charge build-up. Fortunately, since the impedance of insulating materials varies with the frequency of the applied power, the impedance of the circuit can be regulated with an AC power source, making sputtering possible for insulating targets like Cu_2O.

The fact that ions are considerably less mobile than electrons allows to replace the DC power source by an AC power source, while avoiding the substrate to be bombarded by ions. When an alternating voltage is applied to the cathode, the electrode self-biases to a negative voltage [89]. On the positive cycle, lightweight electrons are quickly attracted by the cathode, hence the cathode becomes negatively biased before the end of the positive cycle[1]. Once the cathode is negatively biased, ions are accelerated towards the target. On the negative cycle, the cathode is still negatively biased so that ion bombardment continues.

3.5 RF Magnetron Sputtering

The main drawback of AC/DC sputtering is the low sputtering efficiency. To cope with this problem, strong magnets are added to the cathode in order to confine the electrons and ions in a gaseous plasma near the target. Due to the superposition of an electric and magnetic field, electrons undergo a helical trajectory. In other words, when an electron encounters a magnetic field, its trajectory is bent by the Lorentz force

$$\boldsymbol{F} = q\boldsymbol{E} - q\boldsymbol{v} \times \boldsymbol{B}, \tag{3.5}$$

where q [C] is the elementary charge, $\boldsymbol{v}$ [m/s] is the velocity of the electron, $\boldsymbol{E}$ [V/m] is the electric field, and $\boldsymbol{B}$ [T] is the magnetic field. Hence, thanks to the magnetic field lines arching over the target surface, electrons cannot move far away from the target. This sputtering variant is called RF magnetron sputtering, because the typical operation frequency is 13.6 MHz.

Trapping electrons near the target increases the ion density near the source material, which in turn increases the sputtering efficiency and the deposition rate. Another important advantage is the possibility to operate at a lower chamber pressure without increasing the applied voltage. According to Paschen's law (3.4), due to an apparent increase in the electrode separation distance d in the presence of a magnetic field, the chamber pressure P can be lowered without modifying the breakdown voltage [97]. A lower operation pressure avoids scattering between sputtered atoms and argon atoms, hence increases the deposition rate. Furthermore, confining the plasma near the target avoids damaging the substrate with impinging ions.

---

[1] Assuming that the period of one cycle is 1 s, the time interval that the cathode is positively charged is estimated to be 1 ms. [89]

In conclusion, among the PVD methods discussed in this chapter, magnetron sputtering seems to be the best suited technique to deposit Cu_2O thin films [98] Besides the deposition method, we should bare in mind that parameters like the chamber pressure, the power dictating the energy of sputtered atoms, the size and position of the source with respect to the substrate, and the substrate temperature can affect the crystallinity and quality of the film. This is an important remark because the microstructure of the thin film also affects its mechanical, optical and electrical properties.

3.6 Influence of deposition parameters

Previous studies about magnetron sputtering of copper oxides showed that the substrate temperature, the sputtering power (applied voltage), the sputtering pressure, and the oxygen flow rate are four important parameters affecting the crystallinity, electrical and optical properties of the deposited thin film. Post-deposition thermal annealing can also improve the film quality. We discuss these bibliographic findings in this section because they helped us to fix the sputtering parameters for the deposition of our Cu_2O layers.

All Cu_2O thin films mentioned below were produced from high purity Cu targets by DC or RF magnetron sputtering. Pure argon and pure oxygen have been used as sputter and reactive gases respectively. The impact of different sputtering parameters has been studied by changing one of the experimental conditions and keeping the other factors constant.

Substrate temperature W. Li found that the crystallization and crystal orientation in Cu_2O thin films mainly depends on the substrate temperature. By increasing the substrate temperature, the lattice mismatch between the Cu_2O film is reduced, stress is relaxed, and the crystallinity is improved. However, at excessive substrate temperatures (750°C), undesired copper phase is identified. This may originate from the inert reaction between oxygen and copper as well as the decomposition of Cu_2O under high temperature [99]. Obtaining a single phase of Cu_2O is thus more challenging when the substrate temperature is increased.

Films synthesized at room temperature are amorphous, because adatoms (i.e. adsorbed atoms) lack thermal energy to diffuse along the substrate surface [100]. Their crystallinity and grain size increases with increasing substrate temperature. The thermal energy supplied by heating the substrate allows to fill the voids between the grains. At high temperature, the film prefers to perpendicularly grow on the substrate in a column-like shape, increasing its roughness. Hall measurements indicate a better carrier mobility for increasing substrate temperature. This is a direct consequence of the improved crystallinity and larger grain size, since grain boundaries act as carrier scattering centers. The slight decrease in carrier concentration with increasing substrate temperature is compensated by a larger increase in mobility, leading to a decrease in electrical resistivity [99].

Increasing the substrate temperature also shifts the absorption edge towards shorter wavelengths. In other words, the bandgap and the transmittance in the visible range increase with increasing substrate temperature [98].

Sputtering power The sputtering power mainly affects the growth rate of the film: the deposition rate increases with increasing sputtering power. This is directly related to the fact that the sputtering rate increases with the sputtering power [101]. Less time is thus required to reach a certain film thickness when the power is increased. Moreover, the sputtering rate also affects the composition of the film when oxygen is used as reactive gas. The ratio of Cu atoms to O_2 molecules determines whether CuO or Cu_2O will be formed. Whereas a single phase of CuO is obtained at low sputtering power when the oxygen content prevails, a pure Cu_2O film can be achieved at higher power. It is thus possible to tune copper oxide films from n-type CuO to p-type Cu_2O by changing the sputtering power [85].

When the sputtering power is increased, the grain size increases as the deposition rate is increased. However, above a certain power value, the grain size decreases. Regarding the surface morphology of the films, the roughness decreases with increasing sputtering power. The high surface roughness at low sputtering power is probably due to the less energetic argon ions bombarding the target. Sputtered atoms must achieve enough kinetic energy to diffuse along the substrate surface and rearrange themselves during growth. A lack of energy affects the uniform film growth, hence the surface roughness [101].

As the grain size increases and the roughness decreases, the electrical resistivity of the film decreases. At even higher sputtering, the electrical resistivity decreases further due to the coexistence of Cu and Cu_2O, even if the grains are smaller and the surface roughness increases. The sputtering power also affects the optical transmittance of the thin films. At low sputtering power, the transmittance is low due to the presence of more opaque CuO. Then, the transmittance increases with increasing sputtering power because the yellowish Cu_2O phase becomes dominant. Nevertheless, when the sputtering power is increased further, the presence of Cu induces a sharp drop in transmittance [101].

Argon pressure As mentioned in Section 3.4, the argon pressure, also called the sputtering pressure, should be large enough to sustain the plasma. However, increasing the argon pressure results in more collisions between sputtered atoms and argon atoms. If the argon pressure is too high, sputtered atoms will loose their kinetic energy due to scattering. Consequently, sputtered atoms reaching the surface substrate will not have enough energy to rearrange themselves and form crystalline monolayers. Reddy et al. noted that the quality of the Cu_2O films changed from polycrystalline to amorphous when the sputtering pressure was increased above a certain threshold. This also lead to a decrease in grain size, an increase in surface roughness, and an increase in electrical resistivity [102].

Oxygen flow rate As stated by W. Li [99], the oxygen gas flow rate affects the valence of the copper ion in the film. Whereas below a certain flow rate, the main component of the film is Cu as the target consists of pure copper; for high flow rates, the chief product is CuO. For intermediate oxygen flow rates, the thin film mainly consists of Cu_2O. Mixed phases of Cu/Cu_2O and Cu_2O/CuO have also been reported when varying the flow rate [100]. P-type Cu_2O and n-type CuO can therefore also been achieved by tuning the amount of oxygen available in the sputtering chamber. Several researchers also noticed that the deposition rate decreases with increasing O_2 content: oxidation of the target reduces the sputtering efficiency [98], [103].

The main charge carriers in Cu_2O are holes created by copper vacancies, while the main charge carriers in CuO are electrons created by oxygen vacancies. When the oxygen content is increased, we firstly observe an increase in resistivity due to the transition from a Cu phase to Cu_2O phase: the concentration and mobility of electrons in Cu is much higher compared to the concentration and mobility of holes in Cu_2O. A further increase in oxygen content results in the transformation of p-type Cu_2O to n-type CuO, hence to a decrease of the electrical resistivity since the concentration of highly mobile electrons increases again [103].

At low oxygen flow rate or partial pressure, the copper oxide thin film appears opaque due to the dominant presence of Cu. With increasing oxygen partial pressure, the optical transmittance is improved because Cu_2O becomes the main thin film component. Nevertheless, as the oxygen content is further increased, the transformation of Cu_2O into CuO results in a decrease in the optical transmittance. This increase (resp. decrease) in transmittance when the Cu_2O (resp.CuO) phase becomes dominant is directly linked to the bandgap of both phases. The lower bandgap of the CuO thin film leads to a greater absorption of visible light compared to the Cu_2O thin film [103].

Post-deposition thermal annealing Liu et al. analyzed the impact of post-deposition thermal annealing on the composition of copper oxide films. By contrast to the studies discussed above, magnetron sputtering from a pure Cu target has been performed in a pure argon environment. The main component of the as-deposited thin film is thus Cu. After deposition, the thin films were annealed in ambient air for 2 hours. As the annealing temperature is increased from 100°C to 500°C, the composition of the films transformed as follows:

$$\mathrm{Cu} \longrightarrow \mathrm{Cu/Cu_2O} \longrightarrow \mathrm{Cu_2O} \longrightarrow \mathrm{Cu_2O/CuO} \longrightarrow \mathrm{CuO}. \tag{3.6}$$

The surface morphology also changed from amorphous to polycrystalline with increasing grain size and a decrease in porosity [104]. Hence, optimizing Cu_2O thin films relies on obtaining the desired phase as pure as possible, as well as obtaining a crystalline film with large grains to ensure a good conductivity (by decreasing grain boundary scattering).

Concluding remarks

Among various PVD thin film deposition methods, we found that RF magnetron sputtering was the best suited method to obtain high quality Cu_2O films of a few hundreds of nanometers. The theoretical considerations discussing the adsorption processes governing the film growth and the working principle of magnetron sputtering should help us in the choice of the appropriate sputtering parameters used in Chapter 6. It is important to understand how these parameters affect the crystallinity of the thin film, since the microstructure directly influences its mechanical, optical and electrical properties.

Chapter 4

Characterization Techniques

Characterization techniques are important tools to assess the quality of thin films and silver nanowire networks. In this chapter, we discuss the physical principles of the characterization methods used during our experimental work. The morphological characterization has been performed using SEM. Specific attention is devoted to electron-matter interactions, because they are the backbone of SEM imaging.

Electrical properties have been determined using a two-point resistance measurement for the silver nanowire networks and a four-point resistance measurement for the cuprous oxide thin films. Because the collinear four-point resistance measurement was not conclusive, we also used the Van der Pauw method. The three methods are explained in detail.

Finally, the optical characterization has been conducted by measuring the transmittance of the samples with a spectrophotometer. The working principle of the spectrophotometer is explained by describing the function of the different components. The need for an integrating sphere, baseline correction, and the choice of software parameters is also addressed. Knowing the transmittance, it is then possible to determine the bandgap of the material, as discussed in Section 1.1.2.

Contents

4.1 Morphological characterization

Since the resolution of an optical microscope is limited by the wavelength of visible light, i.e. a few hundred nanometers, an electron microscope must be used to characterize the surface quality of nanostructured samples. As the wavelength associated to electrons is inversely proportional to their energy, microscope images with a resolution down to 0.1 nm can be achieved by accelerating electrons between a series of electrodes [105]. In addition to an enhanced resolution, electron interactions with matter allow to investigate the chemical composition of the sample.

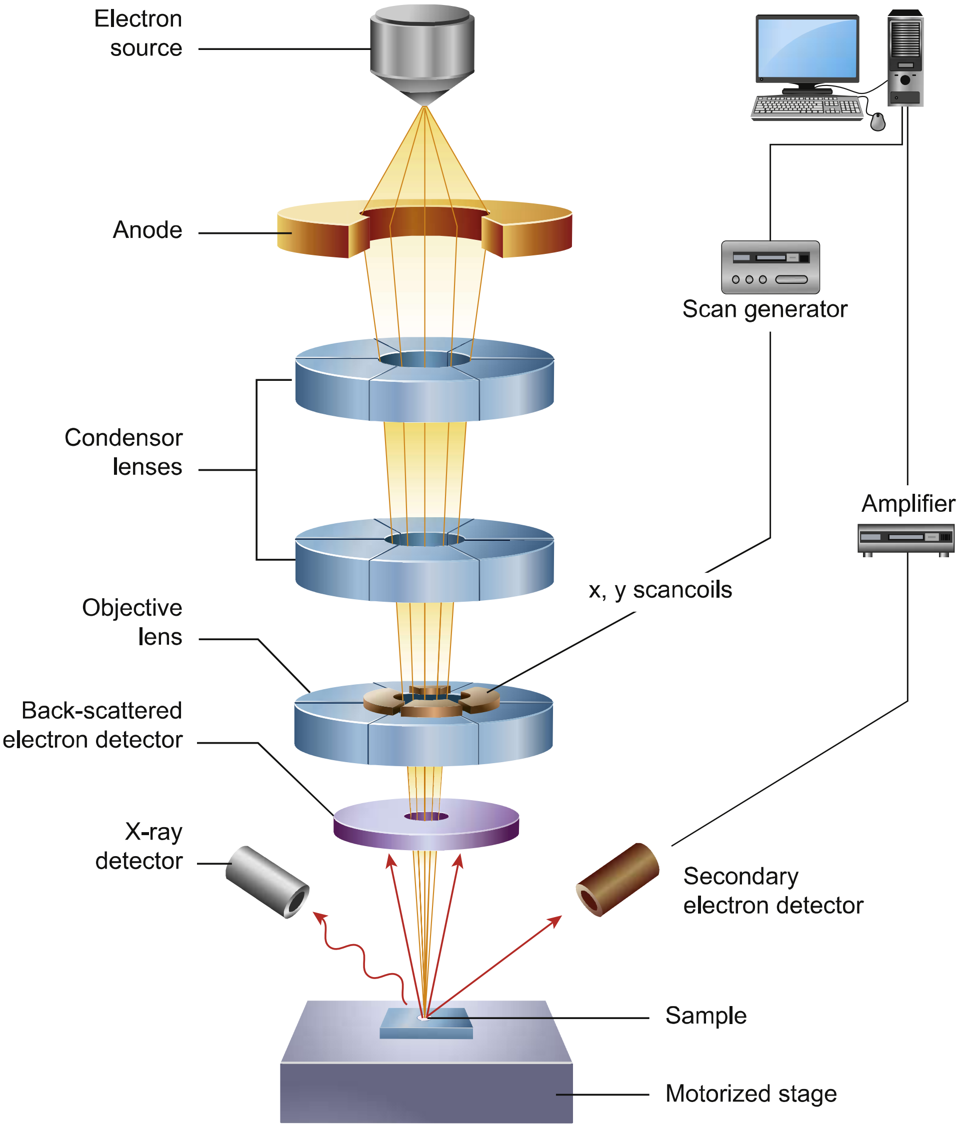

Figure 4.1: Schematic diagram of a scanning electron microscope (SEM). [105]

4.1.1 Scanning Electron Microscopy

Scanning electron microscopy aims at the morphological and structural characterization of a sample by scanning its surface with a highly energetic electron beam. As shown in Figure 4.1, a SEM consists of an electron gun, electromagnetic lenses, a motorized sample holder, and a series of detectors. The electron gun encompasses an electron source and an anode to accelerate the electrons. The electron source is made of a Schottky cathode and an anode: a voltage is applied between the cathode and the anode to facilitate the liberation of electrons by thermionic emission. The electron beam is then concentrated into a small spot by a series of electromagnetic lenses. When the electron beam interacts with the sample, energy is dissipated into different components such as secondary electrons and backscattered electrons. Synchronizing the signals collected by the detectors with the position of the beam allows to reconstruct an image of the sample's surface [105].

4.1.2 Electron-matter interactions

Primary electrons impacting the sample are deviated from their trajectory due to scattering with atoms. The electron-matter interactions can be divided into two main categories: elastic and inelastic collisions. An elastic collision is an energy conserving process which modifies the trajectory of the electron without affecting its wavelength. On the contrary, during an inelastic collision, the electron looses energy; its wavelength is by consequence longer. This energy transfer between electrons and matter is exploited to characterize the material.

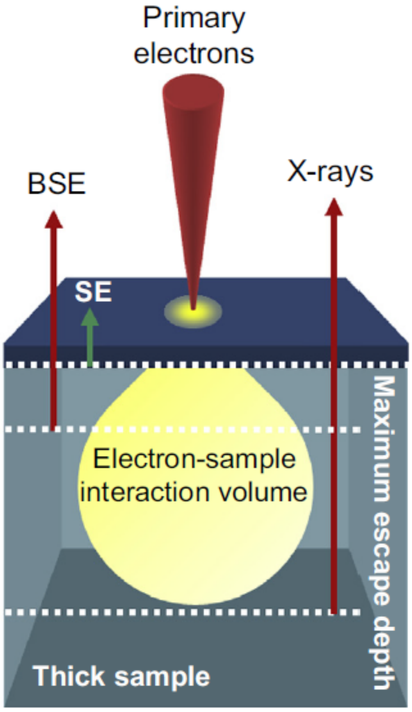

Figure 4.2: Schematic of the interaction types when incoming primary electrons hit the sample.

When the beam of primary electrons hits the sample, the emitted energy is related to Backscattered Electrons (BSE), Secondary Electrons (SE), and X-rays (Figure 4.2). Backscattered electrons are primary electrons which emerge back out of the sample, after suffering elastic or inelastic collisions. Secondary electrons and X-rays are generated by inelastic collisions. The former can be divided into slow SE, fast SE, and Auger electrons. Whereas slow SE are electrons ejected from the atom's valence shell and have little energy (up to 50 eV), fast SE are released from the atom's inner shells and carry energies of the order of the keV. When an electron from a higher energy level falls into a vacancy in an inner shell, energy is often released in the form of a photon. This phenomenon is known as characteristic X-ray emission, because the emitted radiation is specific to the nature of the element. However, the energy transfer can also occur by ejecting an electron, called an Auger electron. X-rays are also generated by Bremsstrahlung. When an electron is deflected from its trajectory by the nucleus of an atom, it loses kinetic energy. This energy is released under the form of electromagnetic radiation.

SEM can be used to analyze the topography, morphology, crystallography and chemistry of a sample. The number of secondary electrons emitted from the sample depends on the angle of incidence of the electron beam: more SE are emitted when the beam is parallel to the sample's surface. Therefore, 3D objects and surface irregularities like grain boundaries are delimited by bright lines in SEM images, allowing the analysis of their size and distribution. The chemical composition of a sample can be deduced from BSE imaging and X-ray spectroscopy. According to Rutherford backscattering, the probability for an electron to be backscattered by an atomic nucleus is proportional to its atomic number. Heavier elements generate therefore more BSE than light elements. By consequence, if a sample consists of two phases, regions of lower average atomic number will appear darker than regions of higher average atomic number. Matching the characteristic X-rays emitted by the sample with elemental standards is a second technique to determine the composition of the sample by SEM imaging. However, this method is not as accurate as X-ray Diffraction (XRD) analysis, since the range of possibly emitted X-rays depends on the energy and orientation of the incident electron beam.

4.1.3 Choice of secondary electron detector

The Pioneer Two scanning electron microscope from Raith Nanofabrication [106] is equipped with two types of SE detectors: SE2 and InLens. The traditional SE detector, also called Everhart-Thornley detector after its designers, is shown in Figure 4.1. This detector, which we will call the SE2 detector, is positioned outside the lens system and is positively biased to attract secondary electrons when the electron beam interacts with the sample. The second type of SE detector, called InLens detector, is placed on top of the SEM chamber, between the anode and the electromagnetic condensor lenses (not drawn in Figure 4.1). The InLens detector favors the use of low energy primary electrons to increase the quality of the SEM images. At first, the primary electron beam is decelerated by an electrostatic lens. Then the secondary electrons scattered in the vicinity of the incident beam are accelerated back into the lens on a helical path [107].

When the electron beam interacts with the sample, a large number of secondary electrons are generated. Low energy secondary electrons, called SE1, are scattered in the upper range of the electron-sample interaction volume (drawn in yellow in Figure 4.2), near the impact point of the electron beam. Because they contain information about the sample surface only, high contrast images can be created when these electrons are collected by the InLens detector. The SE2 detector detects electrons emitted further away from the incident beam and emerging after several collisions in the material. As they carry depth information as well as surface morphology information, images generated with this type of detector show a lesser degree of detail, contrast, and resolution.

Problems with the InLens detector are encountered when the sample to be imaged is not conductive enough. During SEM imaging, the number of electrons absorbed by the sample may be larger than the amount of ejected electrons, leading to a net charge buildup. If the sample and part of the sample holder are conductive, electrons can flow away. Yet, if the sample is insulating (or weakly conductive), a negative charge buildup can distort the electron beam and affect image resolution. Solutions to avoid this effect are reducing the acceleration voltage to lower the energy of the primary electrons, reducing the magnification, and reducing the imaging time.

However, taking these precautions is sometimes not sufficient when the InLens detector is used. When a charge buildup occurs, SE1 are strongly affected by the electric field because they have a low kinetic energy. By consequence, they are easily deflected from their path towards the InLens detector. SE2 electrons, which are emitted further away from where the charge build up occurs and which carry a higher kinetic energy, are less deviated from their trajectory to the SE2 detector.

4.2 Electrical characterization

A two-point resistance measurement is the simplest method to assess the conductivity of a sample. A test current is forced through the sample and the multimeter measures the voltage drop between the two terminals. The problem of this method is that the resistance of the wires and the contact resistance at the terminals are included in this measurement. Therefore to assess the resistance of thin film, it is preferable to rely on a four-point resistance measurement.

4.2.1 Collinear four-point resistance measurement

The resistivity of a thin film can be performed by means of four collinear contact points. At first, a known DC current I is applied between the two outer probes. Then, the voltage V between the two inner probes is measured. Finally, the resistivity is calculated from

$$\rho = F\frac{V}{I}, \tag{4.1}$$

where F [m] is a geometric correction factor depending on the geometric arrangement of the probes, the thickness of the sample, the finite size of the sample, and the position of the probes with respect to the sample edge [108]. The main advantage of a four-point resistance measurement is the elimination of contact resistances at the positions of the probes, considering that voltage probes have a high electrical impedance.

It can be shown that for an infinite 2D sheet of uniform thickness t, probed by four collinear and equally spaced contact points (Figure 4.3), the resistivity is given by

$$\rho = F_0\frac{V}{I} \quad \text{with} \quad F_0 = \frac{\pi t}{\ln 2}. \tag{4.2}$$

This relationship is demonstrated on the next page.

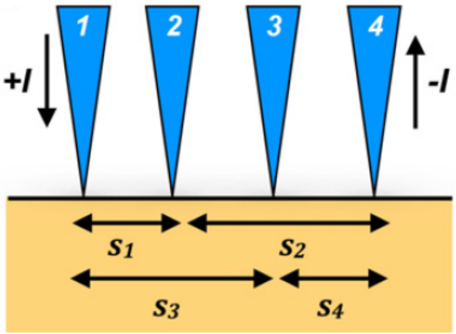

Figure 4.3: Schematic of 4-point collinear probe measurement [108]. While the current is injected by electrode 1 and extracted by electrode 2, the potential drop is measured between electrodes 2 and 3. The distance between the probes is assumed to be constant, i.e $s_1 = s_4 = s$ and $s_2 = s_3 = 2s$.

Proof. When the sample thickness is much smaller than the spacing between the probes ($t \ll s$ [m]), the current emanating from the outer probes can be assumed to spread cylindrically (instead of spherically as it is the case for 3D bulk materials). Therefore, the expression for the area through which the current flows is $S = 2\pi rt$, where r [m] is the distance from the probe injecting the current. Starting from Ohm's law ($J = E/\rho$) and the fact that the electric field derives from a potential ($E = -dV/dr$), the voltage at a distance r from the probe injecting a current $+I$ can be found as follows:

$$\begin{aligned} -\frac{dV}{dr} &= \rho J \\ \Leftrightarrow dV &= -\frac{\rho I}{2\pi t}\frac{dr}{r} \\ \Leftrightarrow \int_0^V dV &= -\frac{\rho I}{2\pi t}\int_0^r \frac{dr}{r} \\ \Leftrightarrow V &= -\frac{\rho I}{2\pi t}\ln r \end{aligned}$$

Considering the particular case shown in Figure 4.3, where a current $+I$ is injected by electrode 1 and a current $-I$ is extracted by electrode 2, the voltage drop measured between electrodes 2 and 3 writes

$$\begin{aligned} V = V_2 - V_3 &= \frac{\rho I}{2\pi t}\Big[-\ln s_1 + \ln s_2 + \ln s_3 - \ln s_4\Big] \\ &= \frac{\rho I}{2\pi t}\ln\Big(\frac{s_2 s_3}{s_1 s_4}\Big) \\ &= \frac{\ln 2}{\pi t}\rho I, \end{aligned}$$

since the spacing between the probes is assumed to be uniform ($s_1 = s_4 = s$ and $s_2 = s_3 = 2s$). □

In practice, nevertheless, samples have a finite size. Consequently, due to boundary effects, which limit the possible current paths in the sample, correction factors are required to ensure accurate results. Considering the four-point probe measurement of a sample of finite size L and thickness t where the probes are spaced by an equal distance s, the correction factors depend on the thickness of the sample ($F_1(t/s)$); the distance of the nearest probe with respect to the sample edge ($F_2(d/s)$); and the finite size of the sample ($F_3(L/s)$). The resistivity can therefore be expressed as:

$$\rho = F\frac{V}{I} \quad \text{where} \quad F = F_0 F_1 F_2 F_3.$$

It has been shown in previous studies [108] that the correction factor can be neglected provided the sample is sufficiently large so that the probes can be sufficiently spaced:

$$\begin{aligned} F_1 &\approx 1 \quad \text{if} \quad s > 5t, \\ F_2 &\approx 1 \quad \text{if} \quad d > 4s, \\ F_3 &\approx 1 \quad \text{if} \quad L > 25s. \end{aligned} \tag{4.3}$$

4.2.2 Van der Pauw four-point resistance measurement

An alternative to the collinear four-point resistance measurement is the Van der Pauw method. This method also uses four contacts to determine the electrical resistivity of a thin film while avoiding contact resistance. The difference is that the probes are applied at the corners of the sample. As illustrated in Figure 4.4, two contact points apply a well known current to the material (in red), the other two measure the voltage across the material (in green).

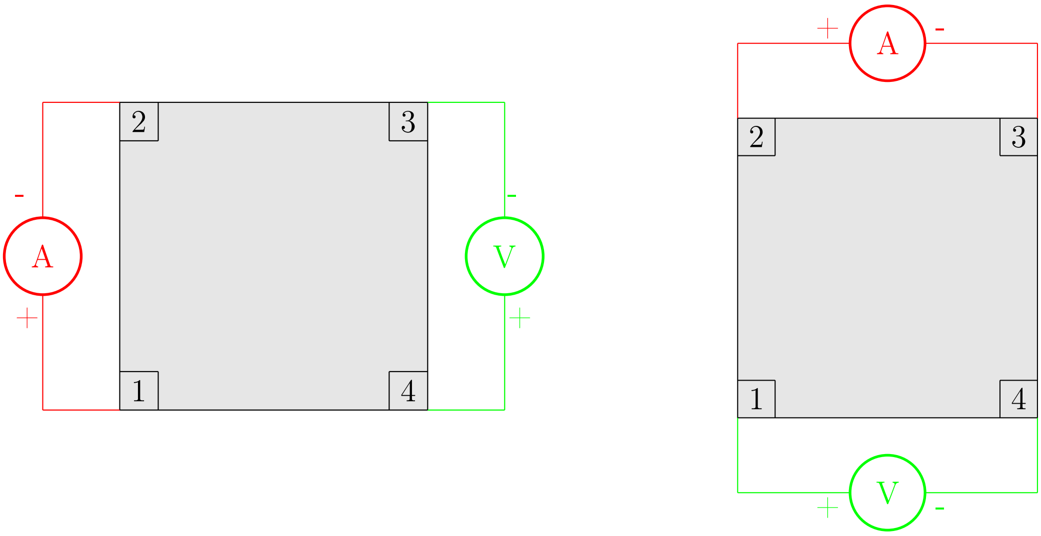

(a) $R_{12,43} = V_{43}/I_{12}$ (b) $R_{23,14} = V_{14}/I_{23}$

Figure 4.4: Schematization of the Van der Pauw characterization method to determine the electrical resistance. While a current is injected between two contact points, the voltage across the other two contact points is measured. The corresponding resistance is obtained with Ohm's law.

Van der Pauw's papers (1958) explain how to extract the resistivity ρ of a sample through a four-point measurement [109], [110]. He proved that the following relation holds for a sample of arbitrary shape and uniform thickness t with sufficiently small electrical contacts 1,2,3,4 at the periphery:

$$\exp\left(\frac{-\pi t R_{12,43}}{\rho}\right) + \exp\left(\frac{-\pi t R_{23,14}}{\rho}\right) = 1, \tag{4.4}$$

where $R_{12,43} = V_{43}/I_{12}$ is the measured resistance when a current is injected between the contacts 1 and 2 and the potential difference is measured between the contacts 4 and 3 (Figure 4.4a). A similar notation is used for $R_{23,14} = V_{14}/I_{23}$ (Figure 4.4b). In order to obtain a direct expression for the resistivity ρ, (4.4) can be rewritten as:

$$\rho = \frac{\pi t}{2\ln 2}(R_{12,43} + R_{23,14}) f(r), \tag{4.5}$$

with f [-] a function of the ratio $r = R_{12,43}/R_{23,14}$ only. In the particular case where $R_{12,43}$ and $R_{23,14}$ are equal, i.e. if the contacts are perfectly symmetric, $f(r)$ is equal to 1. We then recover the same expression as for a linear four-point configuration (4.2).

When performing a Van der Pauw measurement with the PhysTech RH2035 system of our laboratory, equation (4.5) is used to determine the resistivity of the sample [111]. However, the expression of the function f is simplified by an approximation when $R_{12,43}$ and $R_{23,14}$ are almost, but not perfectly equal[1]. Consequently, to reduce the error when computing the electrical resistivity, the contacts must be symmetric; in other words, the sample must be square. Besides, since the contacts were assumed to be infinitesimal and situated at the circumference of the sample, it is essential to make the contact points as small as possible and to place them as close as possible to the edges. Finally, as (4.5) requires the sample thickness t to determine the resistivity ρ, the thickness must be uniform and known before conducting the Van der Pauw measurement.

4.2.3 Two-point network resistance measurement

When silver nanowires are deposited randomly on a substrate, different phenomena can occur. A non-exhaustive list of examples is illustrated in Figure 4.5. In the first situation (I), the nanowires do not overlap. We say that the network is non-percolating. In the second case (II), some groups of nanowires are connected together, the network exhibits percolating clusters. In the last example (III), the network is said to be percolating because the nanowires make the link between the bottom and the top electrode of the sample. To reach the percolation threshold, a minimum number of nanowires must be connected to establish a conduction path between both electrodes, but this does not mean that the whole network must be conductive.

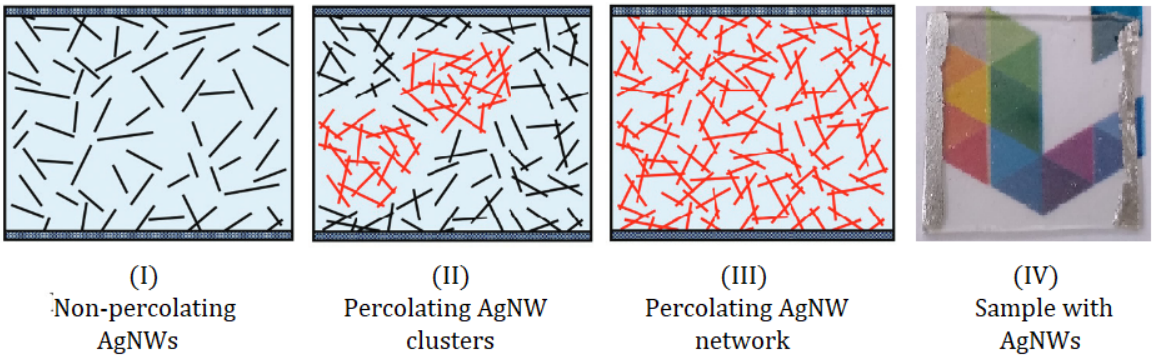

Figure 4.5: Illustration of the notion of percolation and the metallic contacts used to perform the electrical characterization of silver nanowire networks. Adapted from [112].

To gauge the conductivity of the silver nanowire networks, a two-point resistance measurement is conducted with a multimeter in Ohm mode. The conductive terminals are fabricated on two parallel sides of the sample using silver paste, deposited by hand with a toothpick. A photograph of a glass sample covered by silver nanowires and equipped with metallic contacts is shown on the right in Figure 4.5 (IV).

---

[1] The relation that the function f has to satisfy, and an approximation of this function when $R_{12,43}$ and $R_{23,14}$ are almost equal, is mentioned in Van der Pauw's paper [110].

The resistance that we measure is thus the resistance of the sample from one side of the network to the opposite side. To read a finite resistance, it suffices to have one percolating path from one electrode to the other. If the distribution of silver nanowires is homogeneous, the resistance measured between the bottom and top electrodes should be the same as the resistance between the left and right electrodes. Therefore, it does not matter on which sides of the sample the silver paste is added.

Previously, we said that it was more accurate to measure the resistance of a thin film with a four-point method instead of two-point, because this allows to exclude the resistance of the lead wires and the contact points between the sample and the probe. However, this method is only suited to measure the resistance of uniformly distributed silver nanowire networks and deviates from the definition of the percolation threshold. In Section 2.3, we defined the percolation threshold as the critical density to have a continuous percolating pathway from one end of the lattice to the other. If a four-point resistance measure is used, the percolation threshold may not be detected. This situation occurs when the whole network is conducting, except at the edge of one of the four probes. By contrast to the four-point method, measuring the resistance between two electrodes, as shown in Figure 4.5, enables us to directly relate the conductivity of the network to the percolation threshold, because the resistance will change as soon as one conduction path is established between both electrodes.

After all, if the network is as dense as in Figure 4.5, measuring the conductivity of the network with a two-point or a four-point method should give the same result, provided the sample is a perfect square and the instrumental resistance of the multimeter can be neglected. For example, Madaria et al. [113] measured the sheet resistance of silver nanowire networks using a four-probe technique by depositing silver paint at the corners in a square shape, while Lagrange et al. [42] relied on a two-point method.

4.3 Optical Characterization

The spectral transmittance T of a sample at a specified wavelength λ is given by

$$T(\lambda) = \frac{\Phi_T(\lambda)}{\Phi_0(\lambda)}, \tag{4.6}$$

where Φ_0 is the light intensity of the incident beam, and Φ_T is the light intensity obtained when the incident beam has passed through the sample. This measurement can be performed directly with the Shimdazu UV-3600 spectrophotometer [114].

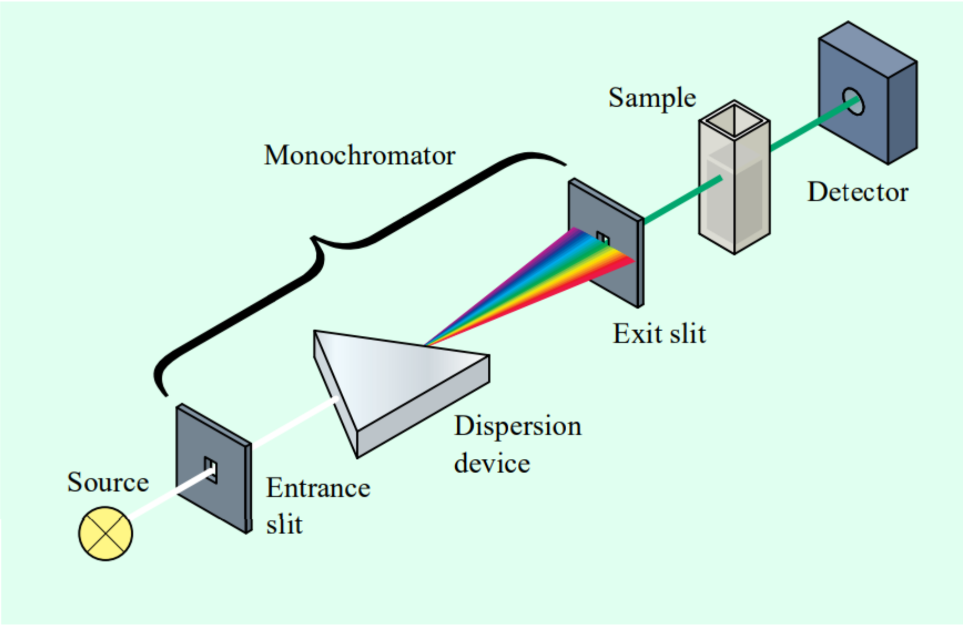

Figure 4.6: Schematic of a spectrophotometer. [115]

As illustrated in Figure 4.6, a spectrophotometer consists of a light source, a monochrometer, a sample compartment, and a detector. To better understand how the transmittance spectrum of a sample can be measured, the function of each component is briefly described.

Light Source To produce a bright light beam across a wavelength range of 185 to 3300 nm, the UV-3600 spectrophotometer automatically switches around 310 nm between a deuterium lamp and a halogen lamp by rotating a reflector. Whereas ultraviolet light is generated by the deuterium lamp, the halogen lamp produces visible and near-infrared light.

Monochromator The monochromator is firstly composed of an entrance slit to select a narrow band of light. Then, a diffraction grating is used as dispersion device to separate polychromatic light into its constituent wavelengths. Finally, to select the desired monochromatic light at the exit slit, the diffraction grating can be rotated. A change in grating occurs around 870 nm.

The resolution of the target wavelength is limited by the slit width and the resolution of the diffraction grating, which depends on the size and number of gratings. Reducing the slit width provides a better resolution since it allows to select a smaller wavelength band, but it also decreases the light intensity. Typically, the slit width is set to achieve a resolution of 2 nm. However, when an integrating sphere is used, the slit width is set to 32 nm to reduce noise due to light losses in the integrating sphere.

Detector Light passing through the exit slit and then through the sample is collected by a detector. To ensure high sensitivity and low noise across the entire wavelength range, the UV-3600 spectrophotometer uses three types of detectors: a Photomultiplier Tube (PMT), an InGaAs photodiode, and a PbS photodiode. They have the same goal, namely converting the light signal into an electrical signal, but their working principle is different. Moreover, their range of sensitivity depends on the materials used to fabricate them.

In a PMT, incident light causes the extraction of electrons at the photocathode by the photoelectric effect. These electrons are accelerated by a high voltage difference applied between the cathode and a series of sequentially arranged dynodes. Striking of highly energetic electrons on these electrodes causes the emission of additional electrons, resulting in a large electrical signal at the end of the photomultiplier tube. By contrast, when light strikes the photodiode, electron hole pairs are created. Consequently, the electrical conductivity of the material is increased and an extra photocurrent is generated.

As summarized in Figure 4.7, a PMT is used for the ultraviolet and visible regions, a cooled PbS photodiode is used for the near-infrared region, and an InGaAs photodiode is used to cover the gap of wavelengths which cannot be captured by the previous detectors. By default, the switching between the photomultiplier detector and the InGaAs detector occurs at 830 nm, and the switching between the InGaAs detector and the PbS detector occurs at 1650 nm. The switch between detectors at these wavelengths can lead to a jump in the measured transmittance.

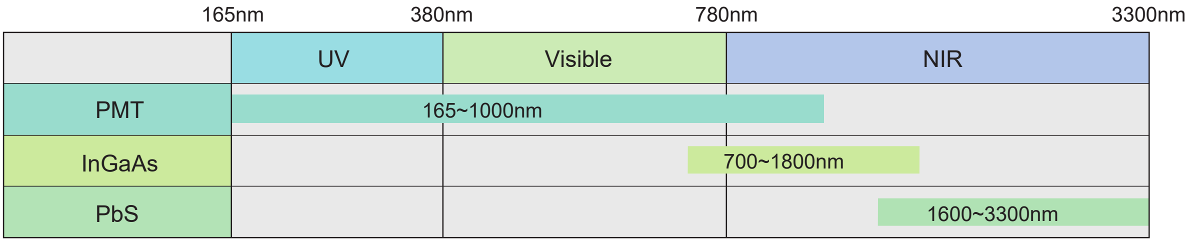

Figure 4.7: Sensitivity range for different types of detectors. [114]

The light transmitted through a sample of finite thickness can be decomposed into two parts: linear transmitted light and diffuse transmitted light. In order to capture both components, an integrating sphere is placed between the sample compartment and the detector [116]. Because light does not directly strike the detector anymore, the light intensity received by the detector is decreased by one order of magnitude. To counteract this effect, the entrance and exit slit are widened.

A coating with a reflectance higher than 90% has been deposited on the inner walls of the integrating sphere to minimize losses. Nevertheless, because reflectance values can change if the surface becomes contaminated, if it deteriorates over time, or depending on variations in the material during production, it is important to perform a baseline correction (a transmittance measurement when no sample is placed in the sample holder) [117]. This ensures that differences in reflectance of the coating will not affect transmittance measurements.

The scan speed (fast, medium, slow, and very slow) determines the number of measurements that are performed at each wavelength. A slow scan speed provides transmittance spectra with lower noise, but the data acquisition time is much longer. Medium speed is a good compromise between reduced noise and acquisition time. Finally, the wavelength step is the step used to sweep the desired range of wavelengths. It is generally set to 1 or 2 nm.

Concluding remarks

To characterize specimens it is essential to understand the working principle of the measuring instrument in order to perceive how the parameters affect the measurement. When using the SEM to examine the morphology of the silver nanowire networks, we will have to make the good choice of detector, depending on the conductivity of the sample. A two-point resistance measurement between two sides of the sample and a transmittance measurement will be exploited to assess the performance of the silver nanowire network.

For the electrical characterization of the Cu_2O films, we will rely on the Van der Pauw method, since the four point collinear probe station is equipped with very sharp tips that could pierce the thin film. It is important to point out that the contact points should be as small as possible and as close as possible to the edges of the squared sample to measure a valid sheet resistance. The thickness of the sample, that is needed to deduce the resistivity, will be determined from SEM cross section images. A measure of the transmittance of the specimen allows to determine the absorption coefficient as a function of the photon energy, which will be used to compute the band gap and the Urbach energy of the Cu_2O films.

Chapter 5

AgNW on glass

In Section 2.2, we saw that parameters affecting the properties of spin coated films are, for instance, the rotation speed, the amount of dispensed solution, the drying time, and the dispensing method. Although the theory presented in that section has been inspired from Newtonian fluid dynamics, we may consider that a solution of silver nanowires belongs to this category provided that the solution is sufficiently diluted. Moreover, in Section 2.4, we noticed that the nanowire size and density influence the optoelectric properties of the network. Because all these parameters affect the final quality of the spin coated silver nanowire network, it is essential to fix some of them in order to optimize specific parts of the deposition process.

The parameters concerning spin coating of silver nanowires that have been studied the most in the literature are the rotation speed, the nanowire size, and the density of the deposited nanowire network. By contrast, little information has been published about the dispensing rate, or whether a dynamic or static dispensing should be preferred. Therefore, we decided to fix the rotation speed, the nanowire size, the concentration, and the total volume of the dispensed nanowire solution, while the parameters of interest are the dispensing rate and whether it is better to deposit the silver nanowire solution on a rotating or fixed substrate.

To optimize the deposition process of silver nanowire networks, we investigated the optical, electrical, and geometrical properties of silver nanowire networks deposited on clean glass. While the optical characterization was conducted with a spectrophotometer, the electrical characterization was performed with a multimeter, and the analysis of the geometry and density of the silver nanowire networks was based on SEM images. Regardless of the varied parameter, the goal was to find the spin coating process that provided the best compromise between conductivity and transparency of the network. Furthermore, an image analysis software (ImageJ) was used to compute the density of nanowires, since electrical and optical properties are directly related to the number of nanowires deposited on the substrate. Specific attention was devoted to thermal annealing because it has been shown that this post-deposition process greatly enhances the conductivity of the silver nanowire networks, without affecting their transparency. We conclude this chapter by comparing the performance of our transparent electrodes to results found in the literature.

Contents

5.1 Fabrication of silver nanowire networks

This section aims at explaining how the silver nanowire networks have been fabricated by spin coating. The values of the fixed parameters are detailed and have been inspired by previous studies found in the literature [118].

Silver nanowire solution Firstly, we purchased a solution of polyol synthesized silver nanowires stabilized in isopropanol (5 g/L) from the company PlasmaChem[1]. The solution should contain silver nanowires with a diameter of 200 ± 4 nm and a length varying between 0.5 and 100 μm. Because too low a concentration of silver nanowires alters transmittance, whereas too high a concentration does not yield a conductive silver nanowire network, we diluted this solution in a 1:2 ratio (1 part silver nanowire suspension to 2 parts isopropanol) [119]. The final solution is shaken vigorously and drawn into a clean syringe.

Glass substrate cleaning Before the use of flexible substrates or the integration of silver nanowire networks in optoelectronic devices, glass is a good material to optimize the deposition process. The first benefit of glass is its high transmittance. Figure 5.1 shows that the 1.5 mm thick corning glass samples from our laboratory exhibit a transmittance between 90 % and 91.6% for wavelengths above 375 nm. This transmittance measurement is in accordance with theoretical predictions expecting a reflectance of 8%, hence a transmittance of 92% if absorption is neglected. Indeed, when a light beam passes through a piece of glass, the electromagnetic waves encounters two air/glass interfaces. Moreover, according to the reflectance expression given in (1.17), 4% of the incident light beam should be reflected at each interface, since the refractive index of air is $n_0 = 1$ and the refractive index of glass is $n = 1.5$ in the visible range. The small bump at 870 nm is due to the change in detector of the spectrophotometer. The sharp drop below 375 nm is caused by the absorption of photons with an energy larger than the band gap of glass. The second advantage of glass is its stability at high temperatures. This avoids degradation of the substrate during thermal annealing, a post treatment that will be used to increase the conductivity of the silver nanowire networks.

Prior to silver nanowire or thin-film deposition, the glass substrates of dimension 1 to 2 cm^2 are cleaned to remove residues like dust and fingerprints. A VWR ultrasound bath [120] is used to ensure reproducible cleaning results without manual effort and damage risk. The samples are rinsed successively with acetone and isopropanol, and dried with a nitrogen gun.

Spin coating procedure M. Lagrange [118] tested several silver nanowire deposition conditions to determine which rotation speed provided the best trade-off. The one offering the best coverage with a limited radial orientation was 1500 rpm. Thus, we decided to fix the rotation speed of our Laurell spin coater at this value [121].

For both the static and the dynamic deposition method, the solution is deposited droplet by droplet using a syringe. In the static mode, droplets are deposited when the substrate is at rest. Then, the substrate is brought into rotation at 1500 rpm with an acceleration of 200 rpm/s.

---

[1] `www.plasmachem.com`

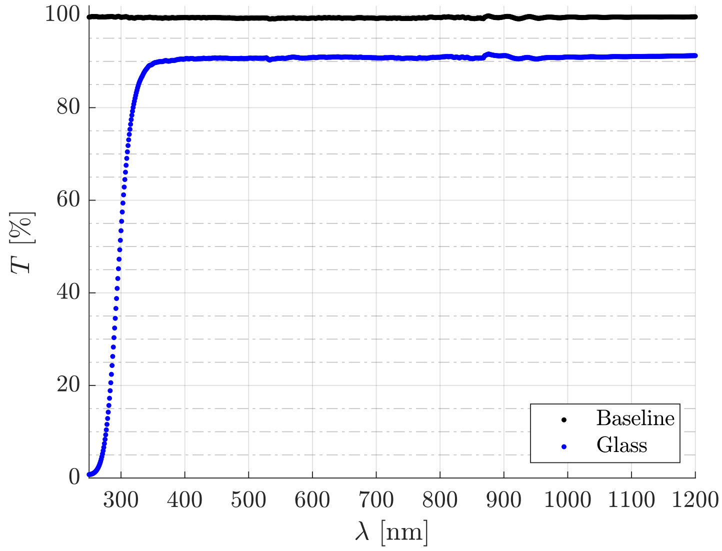

Figure 5.1: Transmittance measurement of a glass substrate from our laboratory. A baseline is performed with an empty sample-holder to take imperfections of the integrating sphere and changes in detector into account. The parameters of the Shimadzu are a slit width of 32 nm, a medium scan speed, and a wavelength sampling rate of 1 nm.

By contrast, in the dynamic mode, droplets are released while the substrate is rotating at 1500 rpm. To assess the influence of the dispensing rate on the quality of the silver nanowire networks, we investigated whether releasing 6 passes of 5 droplets could provide a more uniform coating than releasing 3 passes of 10 droplets, while waiting 30 seconds between each pass.

From a practical point of view, a vertical syringe holder is used to release the drops at the center of the substrate, perpendicularly to the substrate, and always from the same height. About 1 second is taken to form a droplet, so that, on average, 30 droplets correspond to a volume of 0.5 mL. Finally, when realizing a series of samples, the syringe should not be refilled to prevent the extraction of a different concentration of silver nanowires. The solution is also shaken regularly to avoid sedimentation. An automated dispenser and stirrer would be less prone to variations in droplet size, dispensing rate, and silver nanowire concentration than a manual dispenser.

Thermal annealing After spin coating, the nanowire networks are subjected to thermal annealing on a hot plate [122], since it has been shown that this post-deposition process greatly enhances the conductivity of the silver nanowire networks. Once the silver nanowires have been deposited, all substrates are heated on a hot plate at 75°C during 5 min. Then, based on F. Balty's findings (Figure 2.9), the samples are further annealed at 250°C during 10 min. To go from 75°C to 250°C, no thermal ramp has been imposed, but the intrinsic thermal ramp linked to the limited response time of the hot plate is 30°C/min. The total annealing time of the networks is thus about 16 min. The first annealing is meant to evaporate the PVP layer and isopropanol, whereas the second annealing should allow junction formation between nanowires. Thermal annealing also improves the adherence between the nanowires and the substrate.

5.2 Optical characterization

The optical characterization of the samples is performed with the Shimdazu UV-3600 spectrophotometer [114]. To measure the transmission characteristics of the silver nanowire network, first a baseline correction is fulfilled without any sample, then a transmittance measurement is carried out on clear glass, and finally a transmittance measurement is conducted on the glass substrate covered by silver nanowires. The parameters of the Shimadzu have been set to a slit width of 32 nm, a medium scan speed, and a wavelength sampling rate of 2 nm. The same parameters will be used in future transmittance measurements. Using a sampling rate of 1 nm may avoid the small bump observed at 310 nm, which is due to the light source change (Figure 5.2).

As the transmittance measurements of silver nanowire networks deposited on glass and annealed at 75°C/250°C showed identical results, and since a thermal annealing is essential to achieve a decent conductivity for application as electrode, we only present the transmittance measurements for the samples annealed at 250°C. The results are shown in Figure 5.2 and detailed in Table 5.1 by taking the center of the visible range as reference wavelength, i.e. 550 nm. The percentage decrease in transmittance is defined by

$$\frac{T_{\text{glass}} - T_{\text{AgNW}}}{T_{\text{glass}}} \times 100, \tag{5.1}$$

where T_{glass} is the transmittance of the bare substrate, and T_{AgNW} is the transmittance of the glass substrate on which silver nanowires have been deposited.

Deposition method	**Transmittance [%]**	**Decrease in [%]**
Glass	90.64	/
Static 3 × 10	83.93	7.40
Static 6 × 5	81.54	10.04
Dynamic 3 × 10	79.07	12.76
Dynamic 6 × 5	77.33	14.68
	78.62	13.26
	79.07	12.76

Table 5.1: Transmittance (at 550 nm) of silver nanowire networks deposited on glass and annealed at 250°C as a function of the fabrication technique. Three different samples have been tested for the dynamic 6 × 5 method.

While the static deposition technique decreases the transmittance by 7% to 10% with respect to a clean glass substrate, the dynamic deposition technique reduces the transmittance by 13% to 15%. The static method provides thus a larger transmittance than the dynamic method. Besides, the transmittance is a bit higher for the 3 × 10 method than for the 6 × 5 method. The evolution of the transmittance as a function of the deposition method will be justified in Section 5.5, following the presentation of the SEM images which enables a direct analysis of the nanowire network.

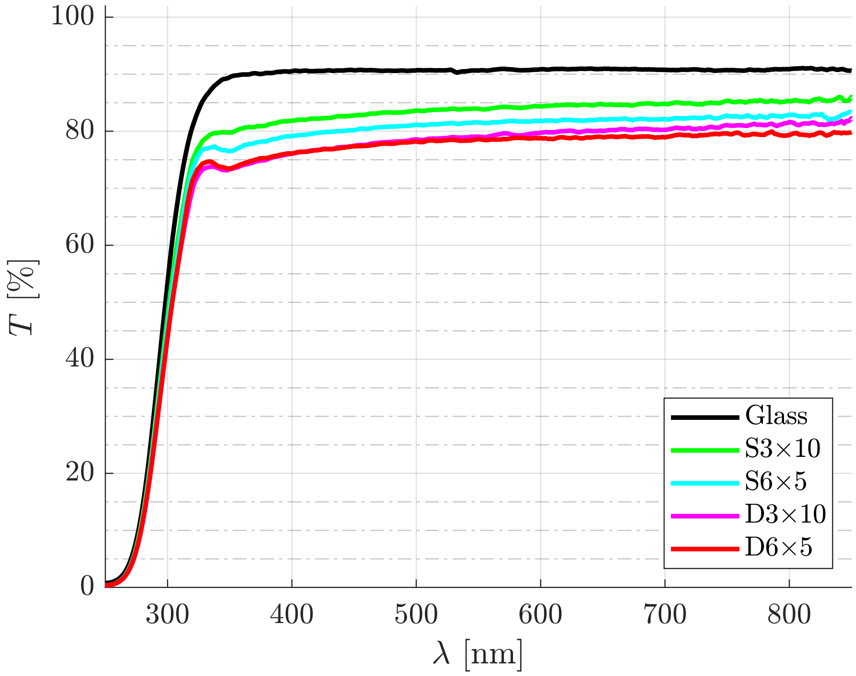

Figure 5.2: Transmittance of silver nanowire networks, annealed at 250°C, for different deposition methods and wavelengths between 250 and 850 nm. S stands for static, while D stands for dynamic.

5.3 Electrical characterization

The electrical results, obtained with a two-point measurement, for the different samples are summarized in Table 5.2. While the resistance of the samples employing the static method generally stays above 1 MΩ, the resistance of the samples using the dynamic dispense is of the order of the kΩ after annealing at 75°C, and below 100 Ω after annealing at 250°C. The static and dynamic deposition methods with 6 × 5 drops and annealed at 250°C have been tested multiple times to confirm the remarkable difference between the static and dynamic technique. While the static preparation process resulted two times in more than 1 MΩ and once in 207 Ω, the dynamic method resulted in 18 Ω, 27 Ω, and 80 Ω.

Method	**3×10 at 75 °C**	**3×10 at 250 °C**	**6×5 at 75 °C**	**6×5 at 250 °C**
Static	$> 10^6\,\Omega$	$> 10^6\,\Omega$	$> 10^6\,\Omega$	$> 10^6\,\Omega$ $> 10^6\,\Omega$ $207\,\Omega$
Dynamic	$52 \times 10^3\,\Omega$	$85\,\Omega$	$22 \times 10^3\,\Omega$	$18\,\Omega$ $27\,\Omega$ $80\,\Omega$

Table 5.2: Electrical resistance of silver nanowire networks deposited on glass as a function of the deposition method and the annealing procedure.

This electrical characterization clearly indicates that the deposition technique has an impact on the electrical properties of the silver nanowire network. The density of silver nanowires obtained with the dynamic deposition method is probably larger than the one obtained with the static dispense. This will be confirmed by the geometrical characterization exploiting SEM images. The good conductivity (207 Ω) that has been observed once with the static deposition method is probably a stroke of luck. An electrical measurement between the two other parallel sides of the specimen should have been performed to verify whether the transverse resistance of the network (top and bottom electrodes) was as low as the longitudinal resistance (left and right electrodes).

It is important to notice that a thermal annealing at 250°C is required to achieve resistances below 100 Ω. For the dynamic method, the post-deposition treatment provides a striking resistance drop by 3 orders of magnitude thanks to welding at nanowire connections. Nevertheless, we observe that thermal annealing is not able to effectively reduce the electrical resistance for the static deposition method. The reason is that, when the initial nanowire density is small, the number of overlapping nanowires is small, hence welding of these connections cannot occur to reduce the global resistance of the silver nanowire network. The initially bad conductivity cannot be enhanced because there are not enough percolation paths to reach the percolation limit above which the silver nanowire network becomes conductive.

5.4 Geometrical characterization

To characterize the geometry of the silver nanowire networks depending on the deposition method, SEM images of several samples have been examined. All SEM images presented in this work have been realized with the PIONEER Two imaging tool [106]. To prevent charge build-up on the insulating glass substrate, we stuck the substrate on the sample holder with double sided conductive carbon tape. Besides, because silver nanowires are conductive, small voltages are enough to characterize their shapes. This avoids the detrimental liberation of a large number of electrons, increasing noise and limiting image resolution.

The specimens have been observed with voltages between 1 and 2 kV, at a working distance between 4 and 5 mm for the InLens detector, and with a voltage of 5 kV and a working distance of 15 mm for the SE2 detector. Because of their different positions in the vacuum chamber, the In-Lens detector gives a better image when approaching the specimen closer to the detector since this maximizes the SE1 collection angle, whereas the optimal working condition for the SE2 detector is at a longer working distance. Different magnifications between 500 and 45 000 × have been used to characterize the microstructures at various length scales. Of course, the measures are performed in vacuum (10^{-4} Pa) to avoid interactions with particles before the electron beam reaches the sample.

To gain a better insight on the area fraction occupied by the silver nanowires, SEM images are post-processed with ImageJ. As illustrated in Figure 5.3, the original images are converted to binary black-and-white images by imposing a user-defined threshold. Every pixel less than that value becomes white, while every pixel greater than that value becomes black.

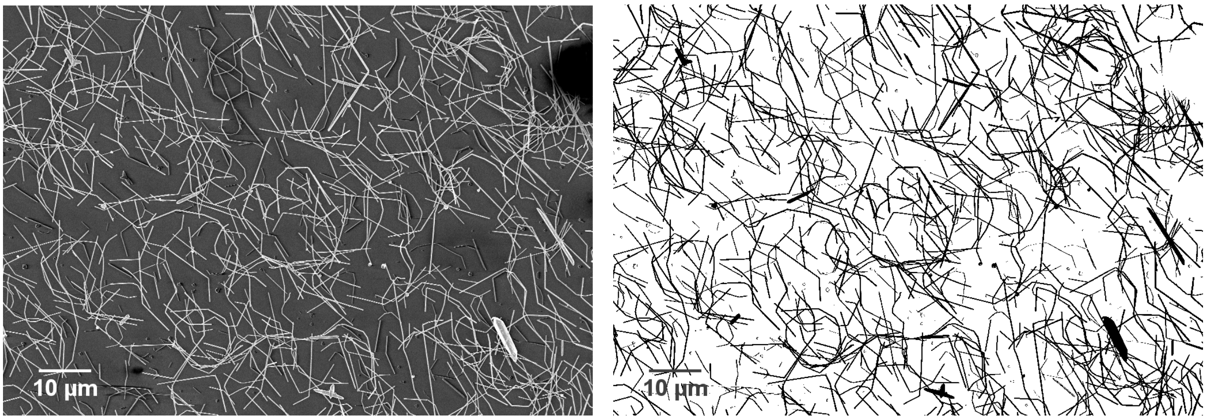

(a) Dynamic 6 × 5, 250°C (InLens) (b) ImageJ

Figure 5.3: Post-processing of an original SEM image to assess the area fraction occupied by silver nanowires.

SEM images for the static and dynamic dispense are shown in Figure 5.4, and the area fraction of nanowires computed with ImageJ for different deposition methods is reported in Table 5.3. SEM images with the same magnification (1000×) and the same detector (InLens) have been exploited to compute these area fractions, except for the static deposition of 3×10 drops (SE2). The SEM images and area fraction results show that the dynamic method provides a much denser nanowire network than the static method: the nanowire network density is doubled when performing a dynamic deposition. We also notice a slight improvement in the area covered by silver nanowires when the droplets are deposited in smaller amounts, namely in 6×5 drops. However, more measures should be performed to confirm this trend, since the difference is relatively small.

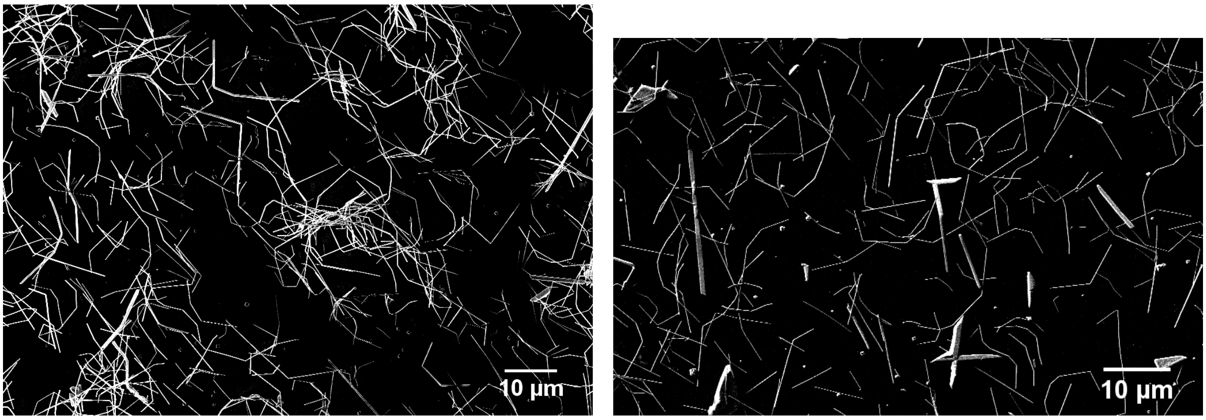

(a) Static 6 × 5, 75°C (InLens) (b) Static 3 × 10, 250°C (SE2)

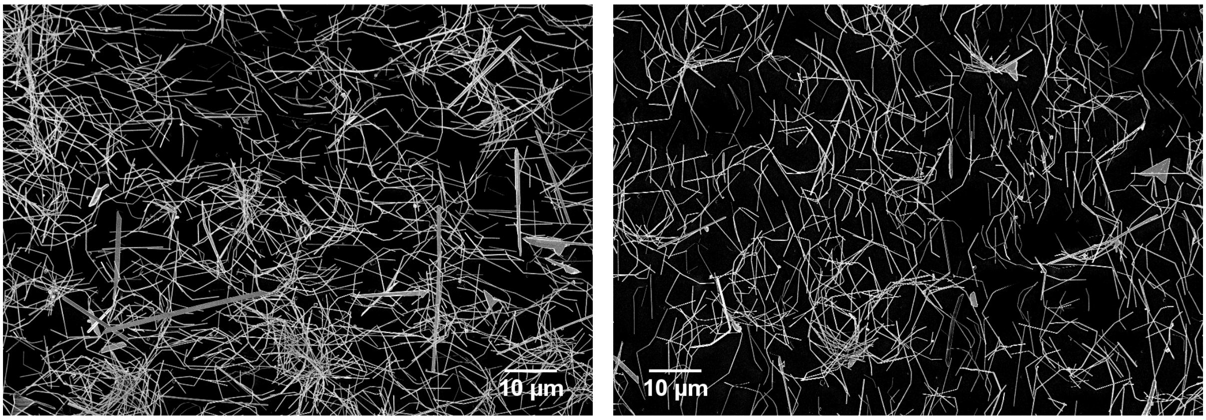

(c) Dynamic 6 × 5, 75°C (InLens) (d) Dynamic 3 × 10, 250°C (InLens)

Figure 5.4: SEM image comparison between static and dynamic deposition. The contrast has been enhanced to better see the silver nanowires.

Method	**3×10 at 250 °C**	**6×5 at 75 °C**	**6×5 at 250 °C**
Static	7 %	11 %	9 %
Dynamic	17 %	23 %	18 %

Table 5.3: Area fraction of silver nanowires deposited on glass as a function of the deposition method and the annealing procedure.

The area fraction covered by silver nanowires for the static 3×10 method may be underestimated, because the silver nanowires appear thinner. To obtain this image, the InLens detector has been replaced by the SE2 detector, since the network was not conductive enough. As explained in Section 4.1.3, when the sample exhibits a bad conductivity, charge buildup prevents the formation of a clear image with the InLens detector. In that case, the SE2 detector becomes the better choice. In view of Figures 5.4a and 5.4b, the area fraction for the static 3×10 method should not exceed 11% if we take into account bigger nanowires. Hence, we can clearly state that the dynamic method provides a denser and more uniform network than the static method.

One of the main issues for a static dispense is that the solvent in the coating solution has time to evaporate before the substrate reaches its final spinning speed [123]. Because isopropanol is a volatile solvent, a significant part can evaporate before the nanowires have time to spread uniformly over the substrate. This may be the reason why the distribution of silver nanowires is less uniform when using the static deposition method.

To achieve the desired nanowire network density, we preferred to deposit a diluted solution of nanowires in several coatings than using a concentrated solution in one coating because a diluted solution spreads more easily. The explanation why a dispense of 6×5 drops should provide a better distribution of nanowires than a dispense of 3×10 drops is that by releasing a smaller number of droplets per pass, the amount of solution ejected during spinning is reduced, and hence the final nanowire density is larger. Besides, as Equation (2.1) indicates, a thick layer thins faster than a thin one, hence a thick layer has a larger probability to not spread uniformly. To reduce the amount of solution ejected during spinning and to obtain a denser coating, it is thus better to deposit the solution in smaller amounts. This is why we introduced a drying stage of 30 seconds between each series of droplets.

Regarding Figure 5.4, thermal annealing of the samples up to 250°C does not seem to affect the global geometry of the as-deposited networks. There are no signs of Plateau-Raygleigh instability. The nanosphere particles, that can for example be observed in Figure 5.4b, were already present before thermal annealing. They originate from the solution of silver nanowires: during the polyol synthesis of silver nanowires, the formation of silver nanoparticles is unavoidable. The difference in area fraction before and after annealing at 250°C, observed in Table 5.3, is not due to the thermal annealing process, but due to the fact that the SEM images are not taken from the same sample or at the same position in the sample. A transmittance measurement of silver nanowires deposited on glass before and after annealing showed identical results. We must bare in mind that spin coating of silver nanowires is a random process, which can lead to different results even if the process is exactly the same.

When the nanowires are observed at a higher magnification (Figures 5.6 and 5.5), we notice that while silver nanowires only overlap at 75°C, junction welding becomes visible at 250°C. This junction welding between overlapping nanowires is responsible for a resistance drop of three orders of magnitude in the case of a dynamic deposition (Table 5.2). In the case of a static deposition, junction formation occurs too, but its influence on the resistance of the network is not measured electrically because the percolating nanowire clusters remain disconnected, as the nanowire network density is too small.

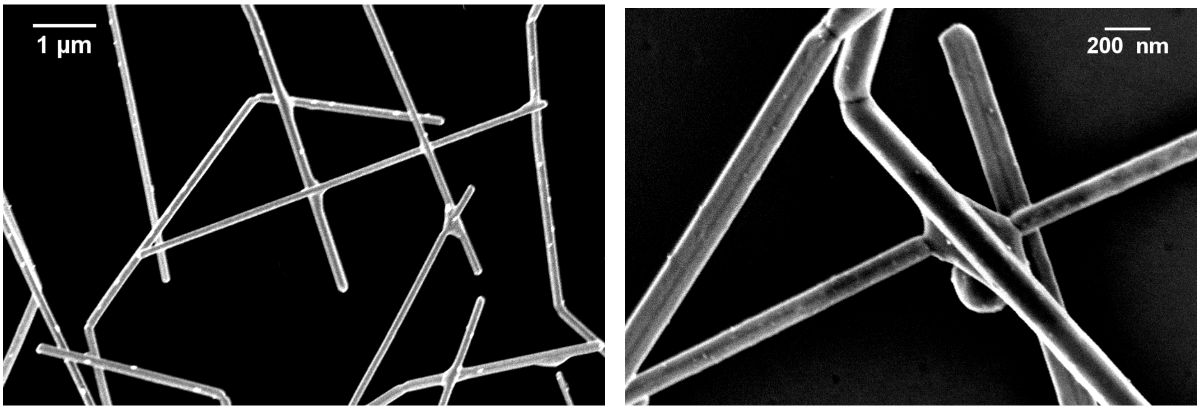

(a) 3 × 5 drops, 250°C

(b) 6 × 5 drops, 250°C

Figure 5.5: SEM image (InLens) showing the welding of silver nanowires, after a dynamic spin coating and an annealing at 250°C. The background was darkened to produce the best possible image.

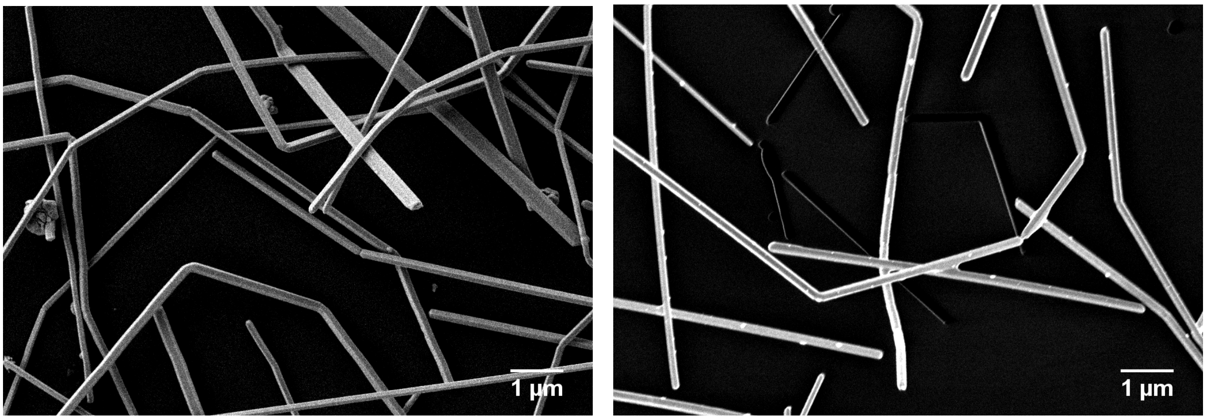

(a) Annealing at 75°C (SE2)

(b) Annealing at 250°C (In Lens)

Figure 5.6: Comparison of the nanowire junctions between a dynamic sample of 6 × 5 drops annealed at 75°C and 250°C respectively. Junction welding only appears after annealing at 250°C. The contrast has been enhanced by making the background darker. Some nanowires in (b) appear black because they are disconnected from the rest of the network.

The black nanowires that can be observed in Figure 5.6b is an illustration of nanowires disconnected from the rest of the network. They appear black since they offer only a very short conducting path compared to the other nanowires that have been connected by thermal welding. Hence, charge buildup will occur faster in these stand-alone nanowires. This image is a proof that nanowire welding is a crucial part of the fabrication process to increase the conductivity of the network.

To end the geometrical characterization of the silver nanowire networks, it should be mentioned that we observed the presence of unexpected agglomerates (Figure 5.7). The nature and origin of these objects of various shapes and sizes is unclear. Even though a chemical analysis should be conducted to determine the composition of the agglomerates and exclude the presence of contaminants, we expect that the agglomerates are made of silver atoms since distinct planes, preventing isotropic growth, can be identified.

A question that remains unanswered is their origin. The first hypothesis is to presume that these silver agglomerates were already present in the solution of silver nanowires. Although the polyol synthesis of silver nanowires offers numerous advantages, it still has some drawbacks. After a period of time, the silver nanowires dispersed in isopropanol may settle down at the bottom of the flask and form irreversible clumps [81]. Moreover, controlling the shape and size during polyol synthesis remains a challenge. The formation of nanoparticles, that can be observed in Figure 5.7, is unavoidable. Other non-spherical shapes, like rods, tetrahedrons, and triangular plates, are formed by anisotropic growth when the growth rate is different in certain directions [62].

The silver agglomerates may also originate from the deposition process. Indeed, their number and size was more significant after a static than a dynamic deposition method. Finally, since in other SEM images the concentration of agglomerates is low when compared to the concentration of silver nanowires, we will overlook their influence on the percolation threshold, the electrical resistance and the optical transmittance of the nanowire networks.

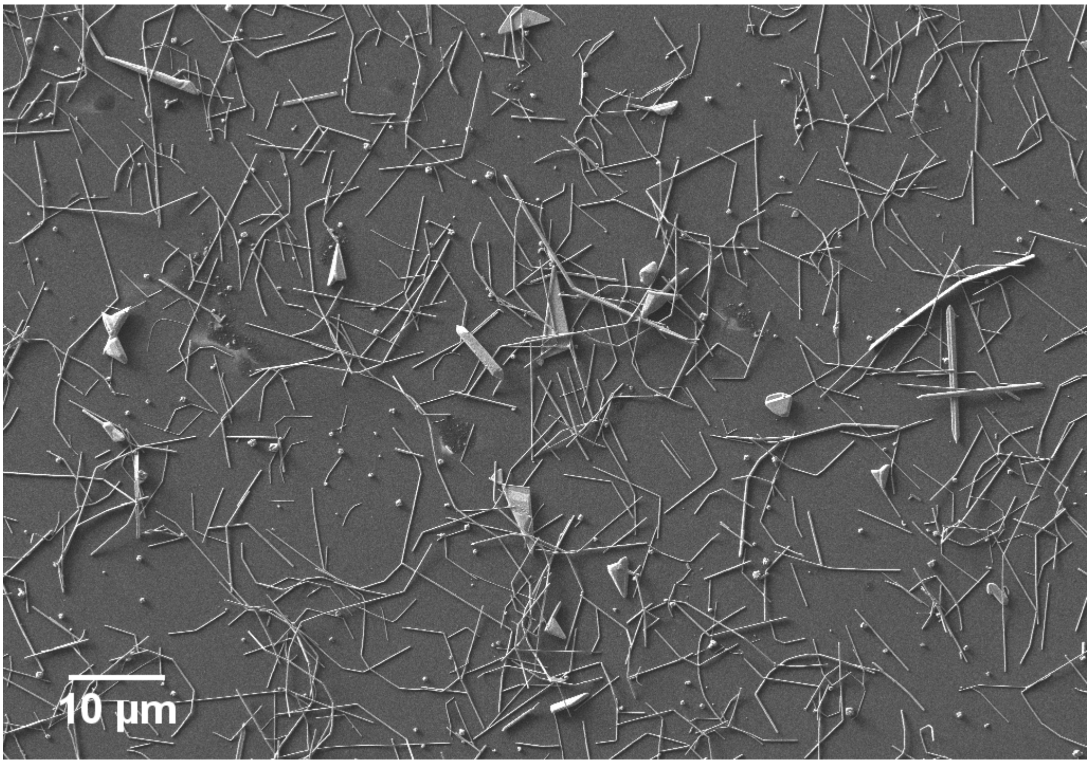

Figure 5.7: SEM image (SE2) showing agglomerates after a static deposition of 6 × 5 drops, taken after thermal annealing at 250° C. However, the agglomerates were already present after annealing at 75°C.

5.5 Conclusion and remarks

The purpose of spin coating silver nanowires on glass was to investigate which deposition method (static/dynamic) provided the best network quality. Now, we can conclude that a dynamic deposition technique offers the best results in terms of uniformity, nanowire network density, and electrical conductivity at the expense of transmittance. Indeed, while the resistance in the dynamic mode decreases by almost 100% (R≃100Ω) with respect to the static method (R≃1MΩ), the transmittance (D6×5 on average: T=78.34%) is reduced by only 3.92% (S6×5: T=81.54%). Moreover, even if the difference is relatively small, it seems that releasing 6×5 drops provides a better network density than releasing 3×10 drops. We also noticed that thermal annealing at 250°C was necessary to achieve a resistance below 100 Ω.

Regarding Figure 5.4, it is clear that the static deposition method (a,b) should render a better transmittance than the dynamic one (c,d), since the area covered by silver nanowires blocks incident light. The transmittance results are thus in accordance with the geometrical and electrical characterization: a smaller density of nanowires resulting from the static deposition provides a better transmittance but a lower conductivity. This conclusion is also in agreement with (2.9) and (2.3) for a fixed nanowire diameter D_{NW}, nanowire length L_{NW}, and critical density n_c.

Knowing the area fraction f covered by silver nanowires (approximately 20% for a dynamic deposition of 6×5 drops), the nanowire diameter (200 nm), and the nanowire length (50 μm), we can deduce the nanowire network density,

$$n = \frac{f}{L_{\text{NW}} D_{\text{NW}}} = 0.02\ \mu\text{m}^2 = 10 \times n_c, \tag{5.2}$$

with

$$n_c = \frac{5.64}{L_{\text{NW}}^2} = 0.002\,\mu\text{m}^2, \tag{5.3}$$

the fitting parameter

$$\alpha = 5.64\,\frac{D_{\text{NW}}}{L_{\text{NW}}} = 0.02256, \tag{5.4}$$

and the network density that should maximize Haacke's FoM (Section 2.4.1),

$$n_{\max} = \frac{1}{17}\left(\frac{2}{\alpha} + 15\right) n_c = 6 \times n_c. \tag{5.5}$$

To compute Haacke's FoM (1.22) for the dynamic 6×5 networks annealed at 250°C, we use the two-point resistance measurement instead of the 4-point sheet resistance measurement that is usually obtained for thin films. Although we may call into question the validity of replacing the sheet resistance of a uniform thin film by the resistance of a percolating network, Haacke's relationship remains an efficient tool to assess the trade-off between electrical conductivity and optical transmittance. The results are shown in Table 5.4 and compared to other silver nanowire networks obtained by spin coating or spray coating in Figure 5.8. The nanowire networks found in the literature were either annealed [42], [124], or plasma treated [16], [113], [125].

Sample	$\boldsymbol{T}$ **[-]**	$\boldsymbol{R}$ **[Ω]**	**FoM$_\mathbf{H}$ [$\mathbf{10^{-3} \times \Omega^{-1}}$]**
1	0.7733	18	4.2
2	0.7862	27	3.3
3	0.7907	80	1.2

Table 5.4: Transmittance at 550 nm with the contribution of the glass substrate, two-point resistance of the network, and Haacke's figure of merit for a dynamic spin coating of 6 × 5 drop and a post-deposition annealing at 250°C.

We notice that our silver nanowire networks (red dots) exhibit a lower figure of merit than other examples found in the literature, yet the order of magnitude is the same when compared to the spray coating method (blue dots). The examples of spin coated nanowire networks (green dots) present a figure of merit that is larger than our experimental values. According to the nanowire network density that should maximize Haacke's FoM ($n = 6 \times n_c$), our nanowire networks are probably too dense ($n = 10 \times n_c$).

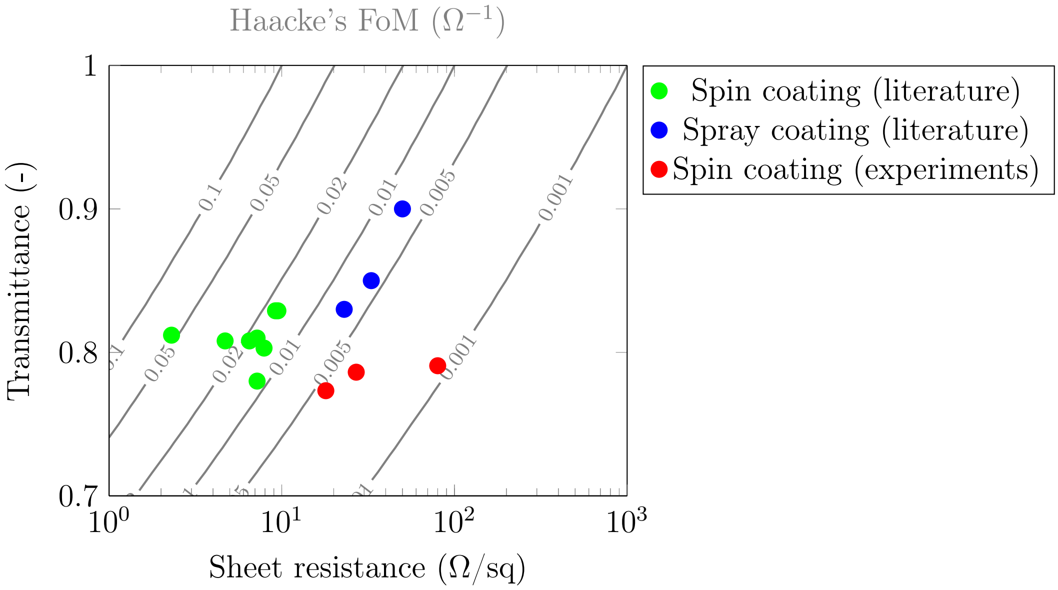

Figure 5.8: Plot of the "sheet resistance", transmittance, and Haacke's figure of merit for different nanowire fabrication methods. The blue dots (spray coating) and green dots (spin coating) are results found in the literature, while the red dots are the experimental values obtained in this work by dynamically spin coating 6 × 5 drops of silver nanowires and performing a thermal annealing at 250°C.

Finally, since silver nanowires are deposited randomly and junction formation occurs arbitrarily during thermal annealing, the electrical resistance and transmittance measurements can vary significantly from time to time. Nevertheless, the probability of obtaining good conductivity results can be increased by using the dynamic method with 6 passes of 5 drops and annealing at 250°C. Consequently, it is interesting to investigate if this method, offering an electrical resistance as low as 18 Ω and a transmittance of nearly 80% when taking into account the glass substrate, is suited to the implementation of a transparent conducting electrode in real devices.

Chapter 6

AgNW on Cu_2O and Cu_2O:Mg

In order to examine the possibility of integrating silver nanowire-based transparent conductive electrodes in electronic devices, the purpose of this chapter is to study the interdependence of silver nanowire networks and their underlying layer made of Cu_2O or Cu_2O:Mg. The aim of these experiments is to investigate whether the deposition and post-treatment methods exploited to deposit silver nanowire networks on glass are also compatible with this type of semiconducting thin film.

The first part of this chapter is devoted to the deposition of silver nanowires on Cu_2O. Then, almost the same procedure is repeated on Cu_2O:Mg. In both cases, the sputtering parameters are specified, and a characterization of the virgin cuprous films is performed to assess their quality. To fabricate the silver nanowire networks, we use a dynamic deposition of 6×5 drops, because this method provided the best compromise between electrical conductivity and optical transparency on glass substrates. The specific parameters for the post-deposition annealing treatment will be specified in due time, since the procedure has been varied from sample to sample. Finally, an optical, electrical, and morphological characterization will reveal whether cuprous oxide thin films are compatible with the deposition of silver nanowires.

Contents

6.1 Silver nanowire networks on Cu_2O

The Cu_2O films were deposited by RF magnetron sputtering with a fixed series of parameters. These parameters have been inspired from theoretical considerations explained in Chapter 3, scientific papers, and previous depositions performed at the SPIN Lab. The choice of these parameters is important as they influence the structural, optical and electrical characteristics of the Cu_2O thin film.

Then, we investigated whether a thermal ramp and the annealing time influence the final electrical and optical characteristics of the silver nanowire networks deposited on Cu_2O. Finally, a morphological characterization of the networks was performed to better understand the interactions between the nanowires and the underlying cuprous film.

6.1.1 Fabrication of cuprous oxide

Before deposition, the chamber must be evacuated to reach high or ultra high vacuum in order to ensure that the mean free path of the sputtered atoms is large enough to reach the substrate. Performing the deposition under high vacuum also limits the number of contaminants that could affect the quality of the thin film. The purity of the deposited film depends on the level of impurities initially present in the target and impurities originating from residual gases like H_2O, CO_2, CO, O_2, and N_2. Because the deposition rate and residual gas pressure determine the oxygen level that can be incorporated into thin films, it is important to deposit at high rates while maintaining a very low base pressure. In practice, a rotary pump is connected to a turbopump. The former is used to quickly achieve rough vacuum, while the latter is employed to pump the chamber pressure down to 10^{-7} Torr. Moreover, a pure Cu_2O target (99.99% purity) is used to avoid undesired impurities.

A descent argon flow rate and argon pressure are required to sustain the plasma, but too large a number of argon atoms may embed on the substrate as impurities. Moreover, if the argon concentration is too high, sputtered atoms will loose their kinetic energy due to scattering. A good compromise is the set the argon pressure at 15 mTorr and to fix the argon flow rate at 20 sccm.

The higher the sputter voltage (2 to 5 kV) or power (150 W), the higher the sputtering yield (0.1 to 10) and ejected atom energy (10 to 20 eV). The sputtering yield is defined by how many atoms can be sputtered/ejected from the target per incident ion and strongly depends on the incident ion energy. Because a higher sputtering yield leads to a higher deposition rate, using a higher sputtering power allows one to reach the target thickness faster and improve the film quality (by preventing incorporation of oxygen). Moreover, increasing the power allows sputtered atoms to gain enough kinetic energy to rearrange themselves during growth.

The maximum power that can be reached using the Nexdep PVD platform [126] from Angstrom Engineering is 300 W. Nevertheless, when using a pure Cu_2O target (2-inches in diameter), we are limited to a power of 66 W. The reason is that the target is welded with indium on a copper plate to allow a better charge evacuation. When power is increased, the local temperature melts the indium solder, which damages the target and the system. Using a power of 66 W still allows us to achieve a decent deposition rate of 0.04 nm/s.

During the deposition, the glass substrate is kept at room temperature (30°C). An interesting alternative would be to heat the substrate during the deposition process to increase the crystallinity and decrease the porosity of the thin film. As shown in Figure 6.1, many glass substrates have been displayed on the substrate holder, resulting in a large area exposed to the sputtered gas. To ensure that enough cuprous atoms would deposit on the substrate and to obtain a more uniform film deposition, the sample holder has been brought into rotation (2.5 rpm) and the target thickness has been set to 250 nm.

Within our laboratory, we keep track of our samples by giving them an identification number (ID). Yet, for easier identification, we will use shorter sample numbers, varying between S1 and S8. Initially, all these glass substrates of 2 cm^2 have been subjected to the same Cu_2O deposition. Unfortunately, some samples received more Cu_2O than others: the samples on the left-hand side in Figure 6.2 look darker than the ones on the right-hand side having a yellowish color. Differences in film thickness have been confirmed by SEM cross section images. These results are summarized in Table 6.1 and show that the effective thicknesses (172 nm, 137 nm, and 129 nm for S1, S2, and S8 respectively) are far from the target thickness (250 nm) measured by the quartz crystal.

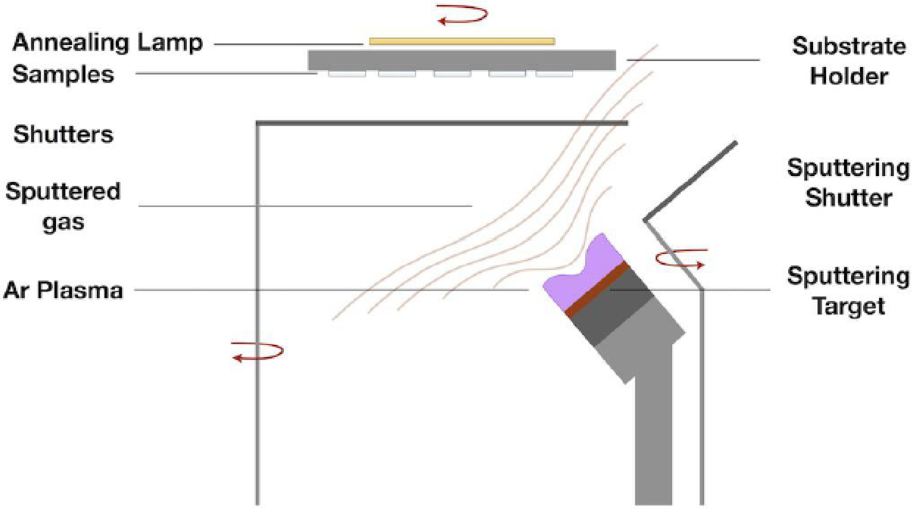

Figure 6.1: Schematic illustration of the sputtering chamber [17]. The red arrows indicate that the shutters and the substrate holder can be rotated. While the plasma and the target deposition rate are initiated by ramping up the power, the substrate shutter is closed. The sputtering shutter is already open before the deposition takes place to clean the target. Once the deposition rate is stabilized, the reading from the quartz crystal is zeroed, the substrate shutter is opened, and the deposition begins.

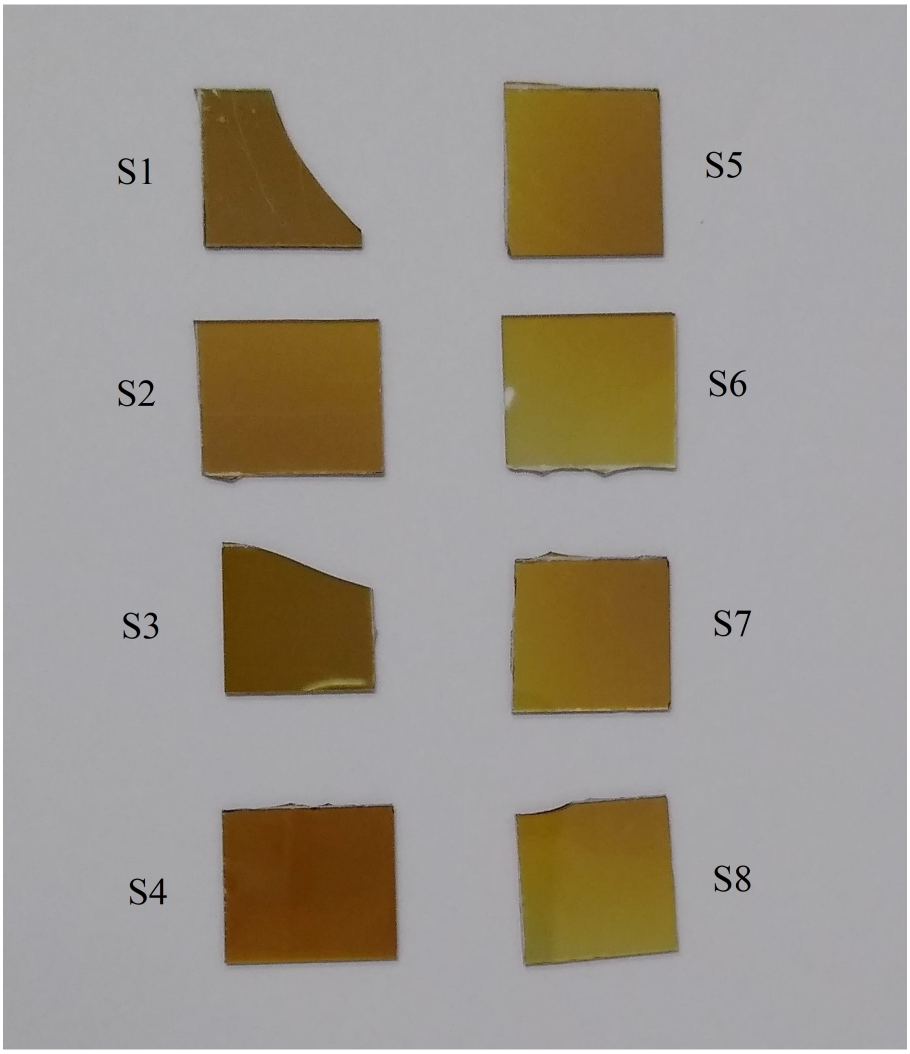

Figure 6.2: Cu_2O thin films deposited by RF magnetron sputtering on glass substrates of about 2 cm^2. The sample numbers are used in this work to differentiate the samples, because some of them received different post-deposition treatments.

ID	**Type of sample**	**Sample number**	**Thickness [nm]**
982	Cu_2O on glass	S1	172
977	Cu_2O on glass	S2	137
981	Cu_2O on glass	S8	129

Table 6.1: Thickness and identification number of Cu_2O samples.

The differences in thickness are probably due to the inclination angle between the sputtering target and the substrate holder, as illustrated in Figure 6.1. Indeed, the deposition varies with the geometric orientation of the substrate and with the source-substrate distance. In order to optimize the film uniformity over a large area, we brought the substrate into rotation, but this measure did not allow to solve the anisotropic film growth. Since the deposition was not uniform, the Cu_2O samples may exhibit different electrical and optical characteristics.

Optical characterization Like for the optical characterization of the silver nanowire networks, we used the Shimadzu UV-3600 spectrophotometer to measure the transmittance of the Cu_2O samples. The reflectance and absorption coefficient are computed by means of (1.17) and (1.20). We consider the refractive index of Cu_2O to be constant ($n = 3.3$), because its values vary less between 400 and 600 nm (2 and 3 eV) [127]. This approximation should not alter the value of the band gap, since we will perform the linear regression in this range.

Figure 6.3 depicts the transmittance and absorption coefficient of the Cu_2O samples for which the effective film thickness has been determined. The transmittance is the total transmittance of the sample, when taking the glass substrate and the Cu_2O film into account. We notice that the transmittance in the middle of the visible range (550 nm) is higher for thinner films (S8). This is in accordance with naked eye observations, where we noticed that the thicker films (S1 & S2) appeared darker. S8 looks more yellowish than S1 and S2 because the characteristic wavelength associated to yellow, i.e. 580 nm, is less absorbed by sample S8 than samples S1 and S2. The decrease in transmittance with increasing film thickness is also predicted by Beer-Lambert law (1.19). Moreover, the reduced transparency in the visible range for thicker films goes hand in hand with a decrease in band gap (Table 6.2). Photons with an energy higher than the band gap are absorbed, and thus not transmitted. When extrapolating the linear regression of the linear part of the $\alpha^2(E = h\nu)$ curves towards the x-axis intercept, we find that the band gaps of S1, S2, and S8 are 2.33 eV, 2.41 eV, and 2.54 eV respectively.

The exponential increase in absorption below the band gap energy is due to band tailing. As explained in Section 1.3.3, the origin of these band tails is related to structural defects: atoms in the sputtered Cu_2O film deviate from the periodic arrangement in a perfect crystal. The larger the presence of Cu_2O amorphous phase, dislocations, and defects, the larger the band tails. Copper vacancies are for example responsible for point defects, generating defect levels within the band gap. By plotting $\ln \alpha$ as a function of $E = h\nu$, we can determine the Urbach energy, which gives an estimate of the disorder in the film. The graphs are shown in Figure 6.3c and the Urbach energies for the different specimens are summarized in Table 6.2. We find that the Urbach energies for the S1, S2, and S8 samples are 268 meV, 232 meV, and 249 meV respectively. These results suggest that the S2 film exhibits the best quality: because the tails expand less in the band gap, we notice a sharper transition in the absorption edge.

The transmittance may also be affected by diffuse reflection. SEM images showed that the crystalline structure of the Cu_2O films consisted in thin reversed shark tooth shaped columns separated by voids. By consequence, the film surface presents a porous nature and a certain roughness. AFM images should be performed to gain a better insight into the surface roughness and the grain size.

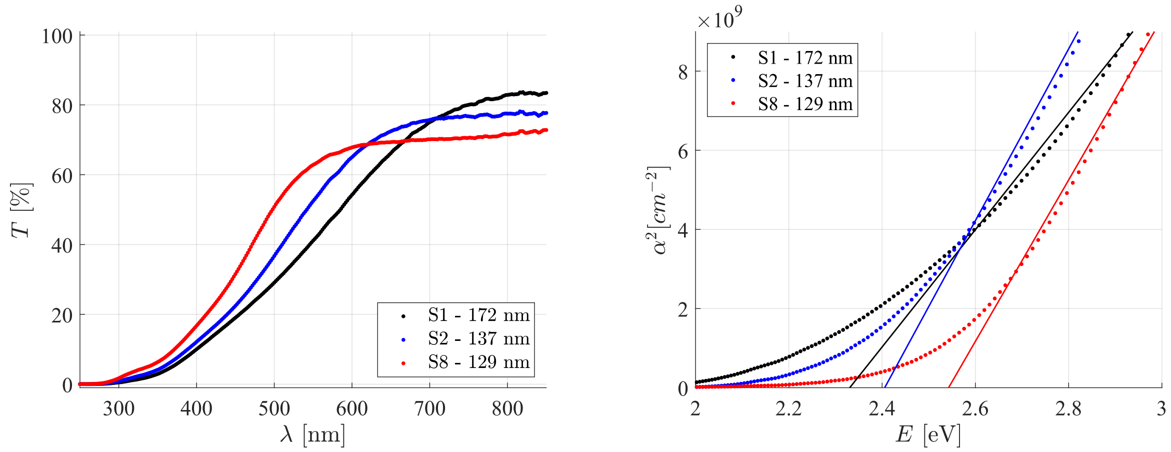

(a) Transmittance

(b) Absorption coefficient

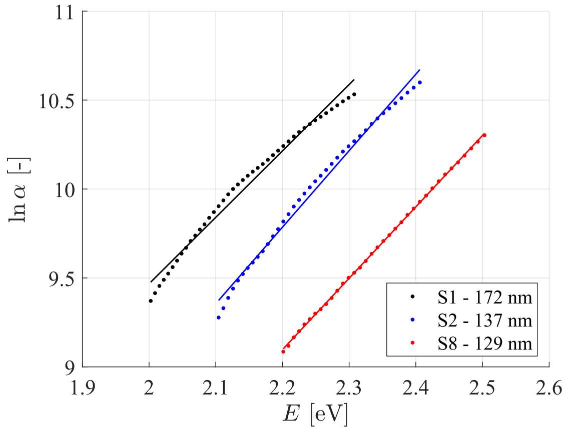

(c) Urbach energy fit

Figure 6.3: Transmittance, absorption coefficient, and Urbach energy fit of virgin Cu_2O samples. By performing a linear regression in (b), we find that the band gap of the S1, S2, and S8 samples are 2.33 eV, 2.41 eV, and 2.54 eV respectively. Similarly, by performing a linear regression in (c) and taking the inverse of the slope, we find that the Urbach energy of the S1, S2, and S8 samples are 268 meV, 232 meV, and 249 meV respectively.

ID	**Thickness [nm]**	**T [%]**	$\boldsymbol{E_g}$ **[eV]**	$\boldsymbol{E_u}$ **[meV]**	$\boldsymbol{R_s}$ **[MΩ/sq]**	$\boldsymbol{\rho}$ **[Ωcm]**
S1	172	51.41	2.33	268	/	/
S2	137	55.81	2.41	232	2.3	143
S8	129	58.43	2.54	249	3.5	205

Table 6.2: Thickness, average transmittance T between 400 nm and 800 nm, band gap energy E_g, Urbach energy E_u, sheet resistance R_s, and resistivity ρ of some Cu_2O samples. The transmittance is the total transmittance of the sample, when taking the glass substrate and the Cu_2O film into account.

Electrical characterization To measure the sheet resistance and to deduce the resistivity of the Cu_2O thin films, we firstly used the MPS150 system from Cascade Microtech [128], a manual probe station relying on the four collinear contact points method. A microscope mounted above the sample holder has been employed to place the probe tips onto the desired locations of the sample. After performing several measurements on the same specimen by raising the probe tips and moving them to the next location, we concluded that this method was not suited to assess the conductivity of the Cu_2O films. The measures varied too much from time to time. The sharp pins may have pierced the thin film, resulting in a measure of the resistance of the glass substrate instead of the Cu_2O film.

To address this problem, we performed Van der Pauw measurements with the RH2035 system from PhysTech [129]. Since the conventional probes provided by PhysTech are considerable and do no not make very good contact, four droplets of silver paste, already dried on the connection pads of the sample holder, are used to connect the thin film to the measurement circuit. Unfortunately, by clamping the sample between the sample holder and a cushion, sample S1 has been broken (as can be seen in Figure 6.2). Because the Van der Pauw measurement requires that the samples have a square shape, the sheet resistance of S1 could therefore not be determined. By simply depositing the sample on the connection pads, without clamping system, we were able to measure the sheet resistances of S2 (2.3 $M\Omega/sq$) and S8 (3.5 $M\Omega/sq$) and determine their resistivity (143 Ωcm for S2 and 205 Ωcm for S8). The advantage of this method, by contrast to wire bonding for example, is that the sample can still be used for future transmittance and SEM measurements.

The smaller resistivity of S2 compared to S8 is probably due to a larger film thickness and a better film quality (predicted by the lower Urbach energy). The fact that an increase in film thickness generally goes together with an increase in the grain size, hence a decrease in grain boundary scattering, may also explain why the resistivity is lower for S2 than for S8. To offer a better performance in real devices, the conductivity of the Cu_2O films could be further enhanced by annealing them.

6.1.2 Deposition and annealing of silver nanowires on Cu_2O

Considering the results obtained on a glass substrate, the spin coating of silver nanowires on Cu_2O was performed using the dynamic deposition method. 6×5 drops, with a waiting time of 30 seconds between each series of drops, have been dispensed while the substrate was rotating continuously at 1500 rpm. Then, the samples have been subjected to two different types of thermal annealing. While two samples (S2 & S6) have been annealed at 75°C during 5 min, then subjected to a thermal ramp of 13.5°C/min, and finally annealed at 250°C during 10 min, two other samples (S4 & S8) have been annealed at 75°C during 5 min, then removed from the hot plate, and lastly annealed at 250°C during 10 min. A graphical representation of the two annealing processes is shown in Figure 6.4. The goal of this comparison (annealing with/without thermal ramp) is to determine whether the annealing rate and time influences the properties of the silver nanowire networks.

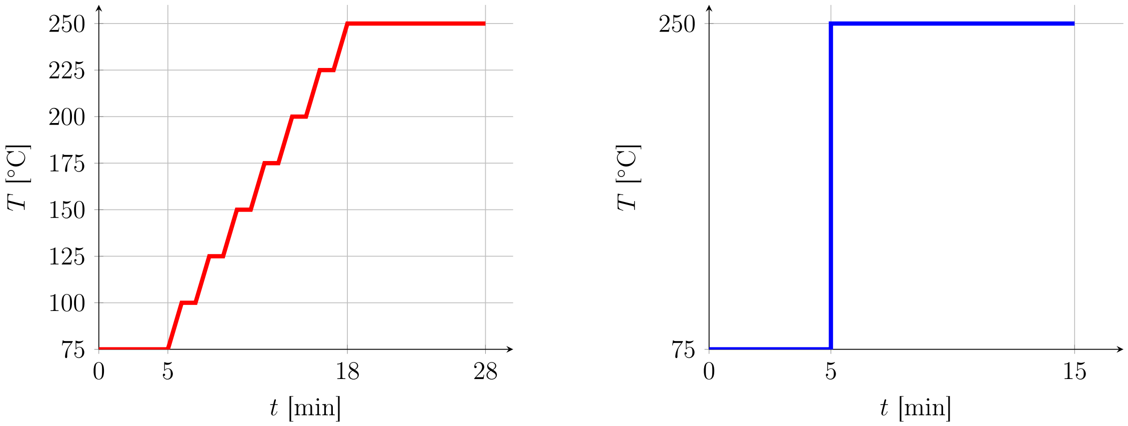

(a) With thermal ramp (S2 & S6) (b) Without thermal ramp (S4 & S8)

Figure 6.4: Annealing processes of silver nanowires deposited on Cu_2O thin films.

6.1.3 Optical characterization

Figure 6.5 shows that a color change occurs when Cu_2O is heated up to 250°C. Sample S1 became even darker when the temperature was increased to 280°C. The exact temperature at which the color change occurs has not been identified, since it is expected that the color variation occurs smoothly. Based on a visual observation of the samples, we conclude that using a thermal ramp has no influence on the final color; what matters is the final temperature at which the sample is heated and maybe the initial color of the sample. By looking more carefully to the annealed samples, we notice a whitish coloring, indicating the presence of silver nanowires and/or PVP residues. Their distribution does not appear to be uniform. This will be confirmed later, when looking at SEM images. We also observe a hole in the middle of the film. This phenomenon occurs when the silver nanowire solution is not dispensed in the middle of the substrate. Since the centripetal force during spin coating makes the solution flow to the edges of the sample, the middle is not coated. This can be avoided by dispensing the silver nanowire solution closer to the center of the substrate.

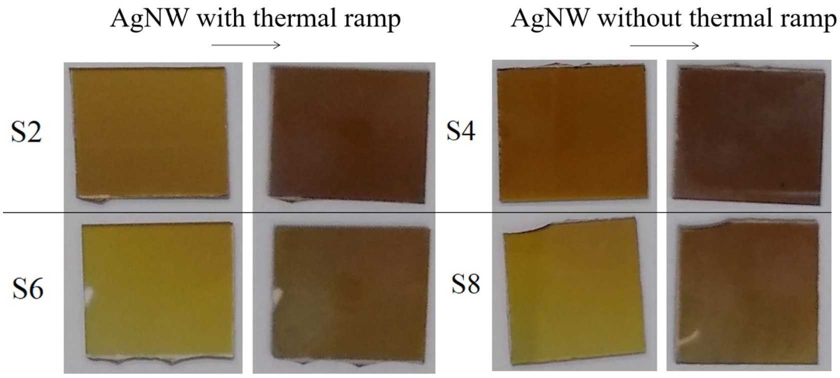

Figure 6.5: Color comparison of virgin Cu_2O samples and Cu_2O samples coated with silver nanowires and annealed up to 250°C, when using a thermal ramp and without thermal ramp.

To examine the impact of the silver nanowires on the transmittance of the Cu_2O films, we performed a transmittance measurement after spin coating and thermal annealing. To assess the transmittance of the silver nanowire networks deposited on glass, we considered the transmittance at 550 nm because this is the reference wavelength that is often mentioned in the literature. Moreover, because the transmittance of the networks is nearly constant between 400 nm and 800 nm, taking the transmittance at 550 nm or the average transmittance only differs by 1%. This reasoning is no longer valid when the silver nanowires are deposited on Cu_2O. Therefore, to assess the transmittance in the visible range of the networks deposited on Cu_2O, we take the average transmittance between 400 nm and 800 nm.

Since the samples turned brown after annealing at 250°C, the transmittance is affected by both the Cu_2O color change and the deposition of silver nanowires. The transmittance decrease in percentage, given by

$$\frac{T_{\mathrm{Cu_2O}} - T_{\mathrm{AgNW}}}{T_{\mathrm{Cu_2O}}} \times 100, \tag{6.1}$$

is thus expected to be larger than when spin coating and annealing the nanowires on glass (Table 5.1). This prediction is confirmed by the average transmittance measurements between 400 nm and 800 nm reported in Table 6.3. While the transmittance decrease for nanowires deposited on glass varied between 10% and 16%, the percentage decrease for nanowires deposited on Cu_2O is on average 30%. If we assume that the impact of the silver nanowires on Cu_2O is the same as on glass, we deduce that the annealing is responsible for a transmittance decrease of 14% to 20%. The thin film color change may have a larger impact on the transmittance if the density of silver nanowires on Cu_2O is smaller than the one on glass.

ID	**Virgin Cu_2O [%]**	**Cu_2O + AgNW [%]**	**Decrease in [%]**
S2	55.81	39.71	28.67
S6	58.19	40.56	30.30
S4	52.62	37.99	27.80
S8	58.43	39.71	32.04

Table 6.3: Average transmittance between 400 nm and 800 nm of silver nanowire networks deposited on Cu_2O and annealed at 250°C with thermal ramp (S2 & S6) or without thermal ramp (S4 & S8). The transmittance takes the contribution of the glass substrate into account.

Figure 6.6 shows the change in transmittance when silver nanowires are spin coated on a Cu_2O thin film, which is itself deposited on a glass substrate. The resulting samples have been annealed at 250°C with thermal ramp (S2) or without thermal ramp (S8). Like in Table 6.3 and in Figure 6.5, performing the annealing with or without thermal ramp does not seem to affect the transmittance differently. Moreover, the impact of the silver nanowires can be assumed to be the same for both samples.

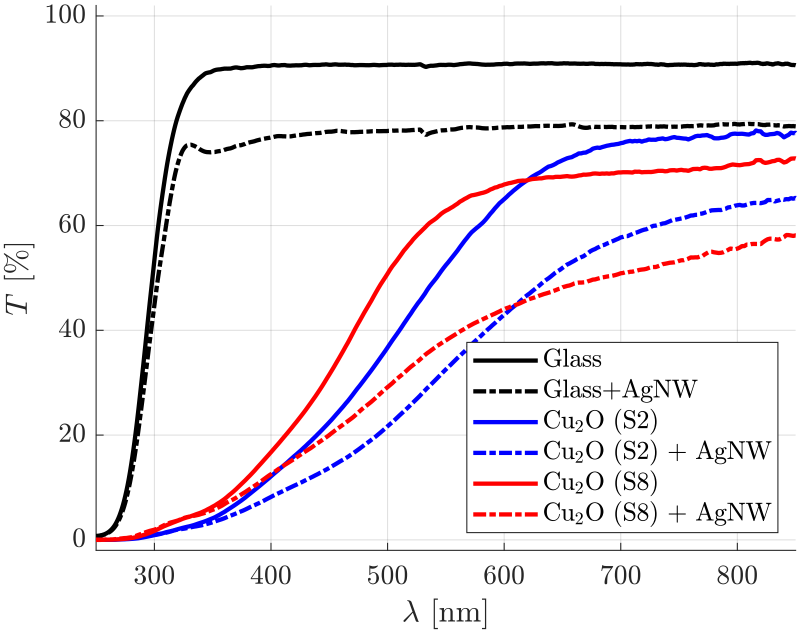

Figure 6.6: Transmittance measurements of Cu_2O samples before and after AgNW deposition and thermal annealing up to 250°C.

The most reasonable hypothesis to explain the brown color shift when annealing the Cu_2O film is to assume that a phase change occurs, resulting in a Cu_2O polycrystalline film with traces of CuO. XRD or X-ray Reflectivity (XRR) should be performed to confirm the presence of CuO. By contrast to XRD, XRR is suited to the analysis of amorphous phases, which may be present in our thin films.

6.1.4 Electrical characterization

Like for the silver nanowires deposited on glass, we added silver paste on two opposite sides of the Cu_2O samples to perform a 2-point measurement in order to measure the resistance of the silver nanowire networks. The electrical results are reported in Table 6.4 against the sheet resistance of the virgin Cu_2O samples.

ID	**Annealing**	$\boldsymbol{\rho}(\mathbf{Cu_2O})$	$\boldsymbol{R_s}(\mathbf{Cu_2O})$	$\boldsymbol{R}(\mathbf{AgNW})$
S2	Ramp to 250°C	143 Ωcm	2.3 MΩ	24 kΩ
S6	Ramp to 250°C	/	3.6 MΩ	21 kΩ
S4	No ramp to 250°C	/	2.1 MΩ	24.9 kΩ
S8	No ramp to 250°C	205 Ωcm	3.5 MΩ	10.4 kΩ

Table 6.4: Electrical characterization of AgNW deposited on Cu_2O. Because the film thicknesses of S4 and S6 are unknown, we cannot determine their resistivity.

Even if comparing the sheet resistance of a thin film and the resistance of a silver nanowire network may be considered like dealing with apples and oranges, we notice that the resistance of the sample is reduced after the deposition of silver nanowires. However, the final resistance, which is larger than 10 kΩ, is unsatisfactory: these samples cannot be used as electrodes. The holes in the middle of the network, that can be observed in Figure 6.5 certainly disrupt the conductivity of the network. This is confirmed by the data reported in Table 6.4, where we notice that the samples S2 and S6, showing a pronounced hole at the center of the substrate, exhibit a large electrical resistance than sample S8 for which the whole is less noticeable. To better understand why the dynamic spin coating of silver nanowires on Cu_2O does not provide an electrical conductivity as good as for silver nanowires deposited on glass ($R < 100\,\Omega$), we will discuss the SEM images taken from samples S1, S2, and S8 in the next section.

6.1.5 Morphological characterization

SEM images of the silver nanowire networks spin coated on Cu_2O help us to understand why the resistance of the network is more than 10 kΩ, whereas a resistance below 100 Ω has been achieved with nanowires deposited on glass. A striking observation when looking at Figure 6.7 and Figure 6.11 is that the nanowire density is low, although a dynamic spin coating of 6×5 drops has been used. Converting these SEM images with ImageJ to binary images, shows that the area fraction covered by silver nanowires is 9 to 11% (Table 6.5). When comparing these values to the one obtained by depositing silver nanowires on glass in Table 5.3, we notice that this coincides with the area fraction computed for the static spin coating of 6×5 drops on glass.

ID	**Annealing**	***T*(AgNW) [%]**	***R*(AgNW)**	**Area fraction [%]**
S2	Ramp to 250°C	39.71	24 kΩ	11%
S8	No ramp to 250°C	39.71	10.4 kΩ	9%

Table 6.5: Average transmittance T between 400 nm and 800 nm, electrical resistance R, and area fraction of AgNW deposited on Cu_2O.

Like for the static spin coating of silver nanowires on glass compared to the dynamic method, we are not sure of the reason why the nanowire distribution for a dynamic spin coating is worse on Cu_2O than on glass. Yet, we can speculate on how the nanowires interact with Cu_2O by taking a closer look at the SEM images. Figure 6.7 and the inset in Figure 6.10 show that some nanowires are not in closed contact with the Cu_2O thin film. A first hypothesis is that the larger roughness of the Cu_2O film compared to the glass substrate may be responsible for the worse adhesion of silver nanowires. Due to the porous nature of Cu_2O, some isopropanol is lost in the nanopores and does not aid to the dispersion of the silver nanowires. The origin of the island growth, that can be seen in the inset of Figure 6.10, is found in lattice mismatch: the newly deposited layer is energetically unstable and transforms spontaneously to a more stable configuration by island growth [130].

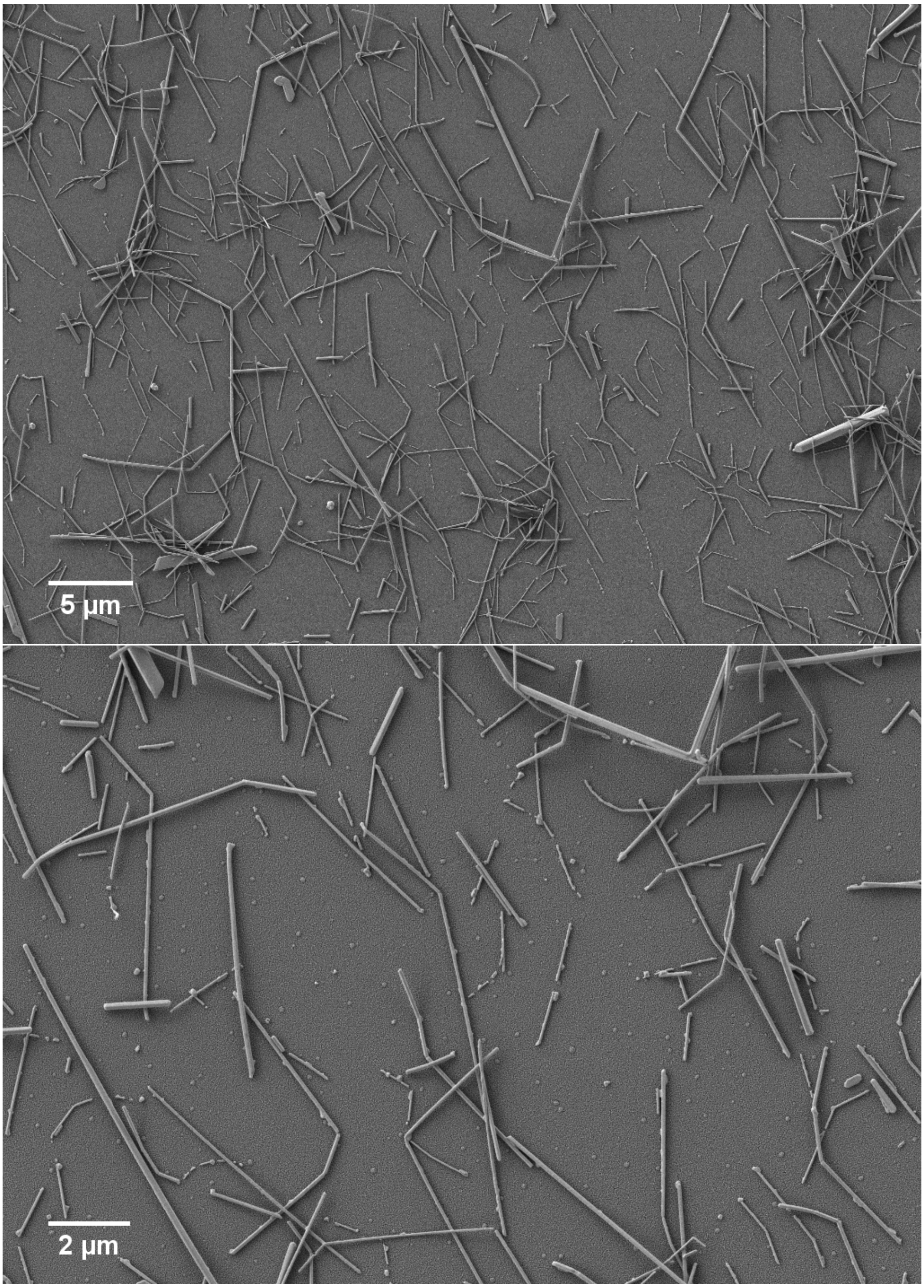

Figure 6.7: SEM images (SE2) at different magnifications of silver nanowires deposited on Cu_2O by a dynamic deposition of 6×5 drops and annealed at 250° C without thermal ramp (sample S8, total annealing time of 15 min). The area fraction covered by silver nanowires is 9% for both magnifications.

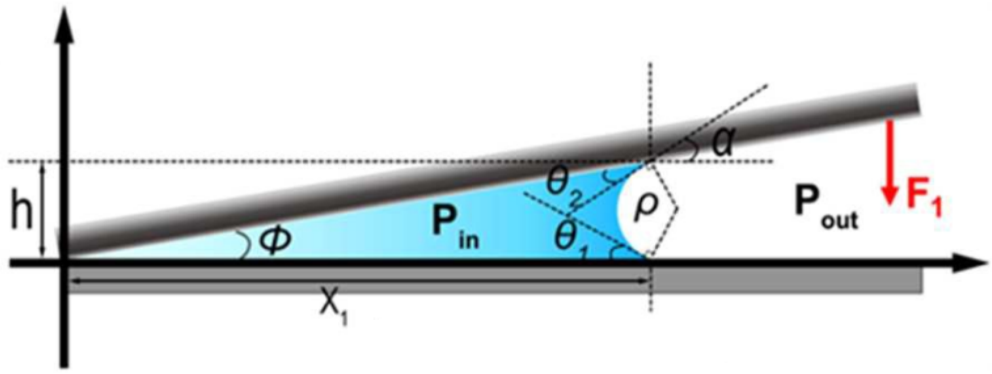

Figure 6.8: Simplified 2D model of the capillary adhesion between a silver nanowire and the substrate. [80]

The connection between crossed nanowires, or between a nanowire and the substrate, is governed by gravity, van der Waals forces, and capillary forces from solvent evaporation. Therefore, the second assumption is that the wettability of isopropanol influences the capillary adhesion force to maintain the silver nanowires in closed contact with the Cu_2O layer. While isopropanol tends to spread spontaneously on glass, this is not the case on a Cu_2O film, which may exhibit a hydrophobic property owing to its different chemical composition and its porous nanostructured surface.

To quantitatively evaluate the capillary force exerted by isopropanol between a nanowire and the substrate, we assume the simplified 2D model illustrated in Figure 6.8. According to Laplace's law, which relates the pressure difference ΔP [Pa] across an interface to the curvature of the meniscus, we have

$$\Delta P = P_{\text{out}} - P_{\text{in}} = \frac{\gamma}{\rho}, \tag{6.2}$$

where ρ [m] is the radius of the meniscus, and γ [$\mathrm{N\,m^{-1}}$] is the surface tension of the liquid. From the notations used in Figure 6.8, the following geometric relationships can be obtained:

$$\alpha = \varphi + \theta_2, \tag{6.3}$$

$$\rho = \frac{h}{\cos\theta_1 + \cos\alpha}, \tag{6.4}$$

where h [m] is the immersion height of the liquid, φ [-] is the inclination angle between the nanowire and the substrate, and θ_1 [-] and θ_2 ['-] are the liquid contacts angles on the substrate and the nanowire respectively. The area of the solid-liquid interface A [m^2] is approximated as the projection of the nanowire with diameter D_{NW} [m] on the substrate plane:

$$A \simeq D_{\text{NW}} x_1 = \frac{D_{\text{NW}} h}{\tan\varphi}. \tag{6.5}$$

The contribution of the Laplace force F_L [N] to the capillary force F_1 [N] is thus given by

$$F_L = \Delta P A = \frac{\gamma D_{\text{NW}}}{\tan\varphi}(\cos\theta_1 + \cos\alpha). \tag{6.6}$$

The contribution of the vertical component of the tensile force F_T [N] at the triple contact line where the liquid, the nanowire, and air meet can be written as[1]

$$F_T = \gamma D_{\mathrm{NW}} \sin\alpha. \tag{6.7}$$

Finally, the resulting capillary force F_1 is twice the unilateral capillary force, because there is also a meniscus on the left-hand side:

$$F_1 = 2(F_L + F_T) = 2D_{\mathrm{NW}}\gamma \left(\frac{\cos\theta_1 + \cos\alpha}{\tan\varphi} + \sin\alpha \right). \tag{6.8}$$

Knowing γ, D_{NW}, φ, and θ_2, the relationship between the capillary force F_1 and the substrate contact angle θ_1 can be plotted by using this equation. This is done in Figure 6.9, where the capillary force has been computed for silver nanowires of 100 nm in diameter, immersed in water (γ = 72 mN/m at 25°C), and deposited on glass ($\theta_1 = 4.5°$) or on PET ($\theta_1 = 84.5°$). The capillary force on glass is found to be 197 nN, while the capillary force on PET is 104 nN. The corresponding pressure exerted on the nanowire is thus estimated to be 25 MPa on glass, and 13 MPa on PET.

This theoretical approach allows to better understand why, in our experiments, the adhesion of silver nanowires on Cu_2O is worse than on glass. In the literature, it is found that isopropanol has a lower surface tension than water (γ = 23 mN/m at 20°C), while exhibiting a negligible contact angle when deposited on glass ($\theta_1 = 0$). Isopropanol will therefore spread more easily on glass than water. When isopropanol is deposited on RF magnetron sputtered Cu_2O, θ_1 is predicted to vary between 60° and 110°, depending on the roughness and the phase composition of the film [131]. This means that isopropanol is less likely to spread on Cu_2O than on glass. Hence, a similar drop in capillary adhesion force as shown in Figure 6.9 is expected when the glass substrate is replaced by a Cu_2O thin film. Taking into account that isopropanol has a high evaporation rate, this reasoning may also explain why a dynamic dispense allows to fabricate denser networks than with the static method. In the latter method, even if isopropanol spreads easily on glass, the solvent has time to evaporate before the silver nanowires are spread and stuck on the substrate.

The loose adhesion of nanowires is a problem because the substrate is rotated at 1500 rpm during the deposition. By consequence, as shown in Figure 6.10, the nanowires accumulate at the borders of the sample, instead of being dispersed over the substrate. It is unclear why the nanowires are not ejected from the sample, as it was the case during the deposition of silver nanowires on glass.

---

[1] The vertical component of the tensile force at the triple contact line where the liquid, the substrate and air meet is assumed to be compensated by the fixed substrate.

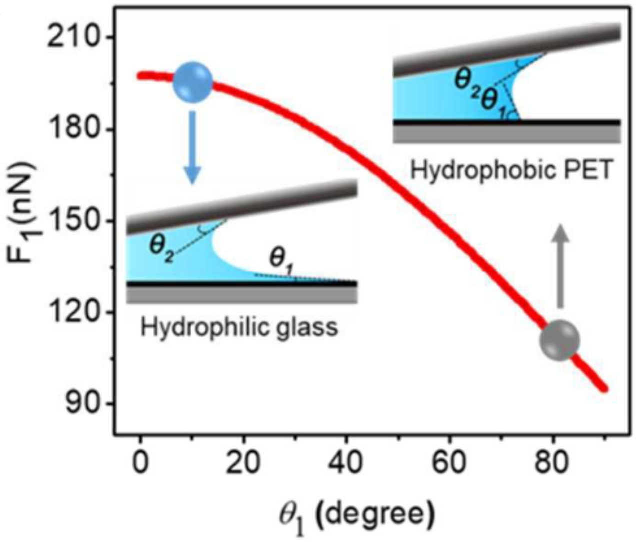

Figure 6.9: Plot of the capillary force F_1 as a function of the contact angle with the substrate θ_1. The capillary adhesion force depends on the wetting properties of the solid: if the substrate is hydrophilic, the liquid will easily spread on the substrate, and the adhesion force will be strain. The opposite phenomenon is observed when the substrate is hydrophobic.

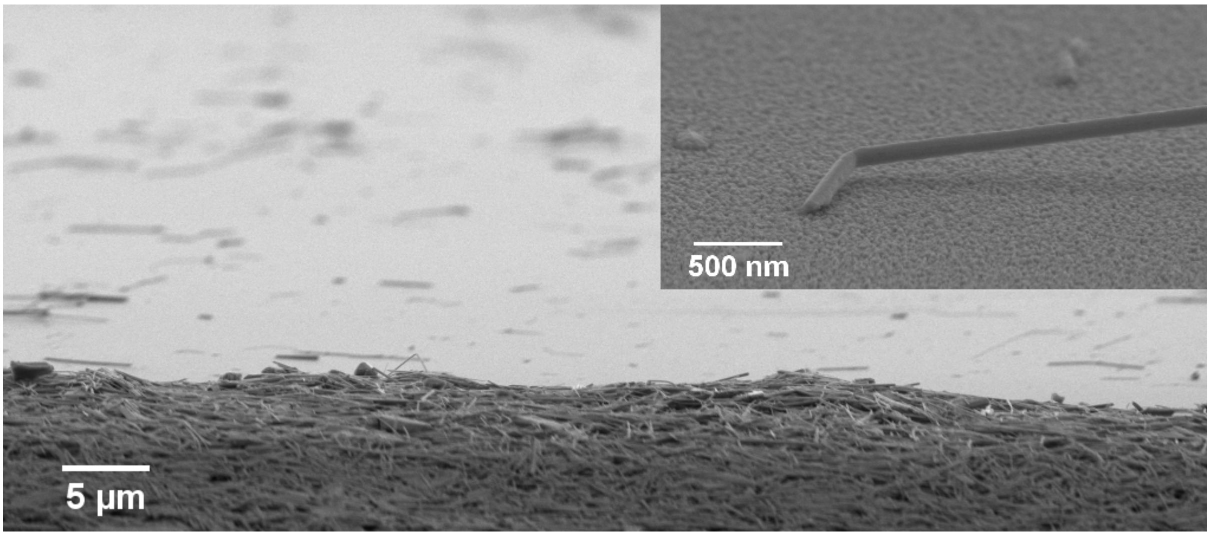

Figure 6.10: SEM images (SE2) of silver nanowires deposited on Cu_2O by a dynamic deposition of 6×5 drops and annealed up to 280° C with thermal ramp (sample S1). The large figure shows that silver nanowires accumulate at the borders of the sample, while the inset illustrates the loose adhesion of silver nanowires with the underlying Cu_2O thin film.

To remove isopropanol and PVP residues, to weaken the junction resistance between nanowires, and to improve the adhesion between the nanowires and the substrate once isopropanol has evaporated, the specimens are annealed. However, an issue that is encountered when the silver nanowire networks are fabricated on Cu_2O is the thermal decomposition of the nanowires when the substrate is annealed at 250°C. In Figure 6.7 (bottom image) and Figure 6.11, we notice that the thinnest nanowires ($D_{\mathrm{NW}} < 100$ nm) have been decomposed into smaller pieces, that are still aligned at the original position of the silver nanowires. The number of spheroidized nanowires in the second image is larger because the annealing time was longer: the nanowires in Figure 6.7 have been annealed without thermal ramp for a total time of 15 min, while the nanowires in Figure 6.11 have been annealed with a thermal ramp for a total time of 28 min.

According to the Rayleigh-Plateau instability and the Gibbs-Thomson effect described in Section 2.5, it is not surprising that only the thinnest nanowires spheroidize. Nevertheless, it was unexpected to already observe this phenomenon at 250°C for nanowires of 70 to 90 nm when compared to the spheroidization temperature presented by Langley et al. (Figure 2.8 with a thermal ramp of 2°C per minute) [77]. Furthermore, this instability has not been observed for the silver nanowires deposited on glass. Like the wetting properties of isopropanol depend on the nature of the substrate, the threshold to reach the Rayleigh-Plateau instability may also vary from substrate to substrate. A larger surface roughness may favor the appearance of instabilities. Instabilities also start at structural defects where the nanowires are locally thinner.

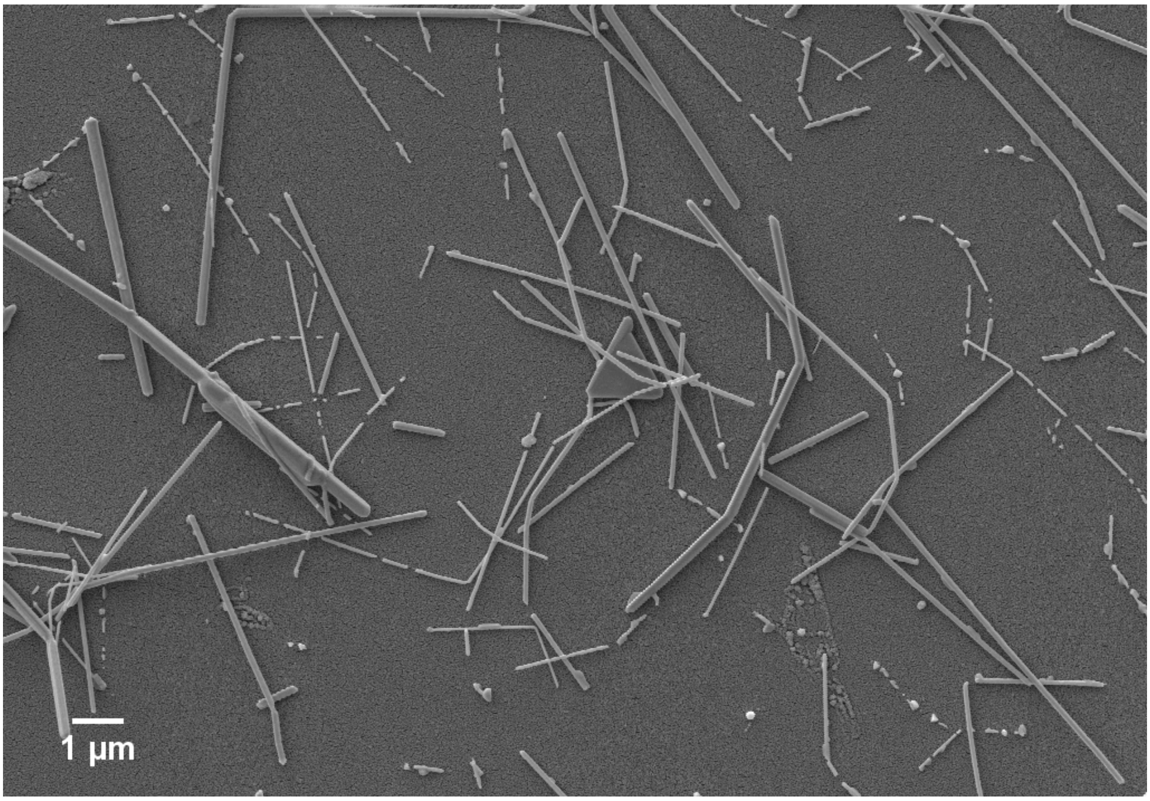

Figure 6.11: SEM image (SE2) of the thermal decomposition of silver nanowires deposited on Cu_2O by a dynamic deposition of 6×5 drops and annealed up to 250° C with thermal ramp (sample S2, total annealing time of 28 min). The area fraction covered by silver nanowires is 11%.

6.1.6 Conclusion and remarks

The optical and electrical characteristics of the sputtered Cu_2O films, exhibiting a resistivity between 143 and 205 Ω cm, a band gap in the range of 2.33 and 2.54 eV, and a peak transmittance between 72% and 84%, are in accordance with results found in the literature. Depending on the sputtering power, pressure, and oxygen flow rate, researchers reported resistivities between 11 and 3700 Ω cm, a band gap between 2.04 and 2.51 eV, and a peak transmittance ranging from 69% to 88% [101], [102], [132].

The goal of depositing silver nanowires on Cu_2O was to investigate whether we could obtain silver nanowire networks with electrical and optical characteristics similar to the one deposited on glass. Unfortunately, we conclude that the silver nanowire networks on Cu_2O have an electrical conductivity of the order of 20 kΩ and an optical transmittance of 34%, while the silver nanowire networks on glass had an electrical conductivity down to 18 Ω and an optical transmittance of almost 80%.

SEM images showed a low network density, explaining the bad conductivity of the networks. The non-uniform distribution of the networks is due to a loose adhesion between the silver nanowires and the Cu_2O thin film, which can be attributed to the hydrophobic behavior of Cu_2O. The contact angle of isopropanol on the Cu_2O films should be investigated, as it is strongly dependent on the roughness, the porosity, and the phase composition of the film. The dramatic decrease in transmittance is due to the color change of Cu_2O when it is annealed up to 250°C. This change in color is probably linked to a phase change of Cu_2O into CuO, but should be verified with an XRD and/or XRR analysis. Finally, nanowires with a diameter smaller than 100 nm spheroidized at 250°C, whereas this was not the case for silver nanowires deposited on glass. The type of substrate and its roughness may influence the threshold before this instability occurs.

6.2 Silver nanowire networks on Cu_2O:Mg

The successful implementation of n-type oxides in transparent electronic devices has motivated the interest in p-type oxides, the counterpart of n-type oxides in solar cells, light-emitting diodes, and transistors. Until now, p-type oxides showed inferior properties when compared to n-type oxides, since none of them combined high conductivity and high transparency. Even the best p-type TCO present larger resistivities than non-optimized n-type TCO.

In the previous section, we studied cuprous oxide (Cu_2O) because this semiconductor exhibits good electrical characteristics within the family of p-type oxides, i.e. a resistivity around 100 Ωcm and a mobility around 100 $cm^2V^{-1}s^{-1}$ [4]. Other advantages are the non-toxicity and high availability of copper and oxygen, and the easiness and low cost of Cu_2O synthesis. However, due to its relatively small band gap (between 2.1 and 2.6 eV depending on the film thickness), we saw that the transmittance in the visible part of the spectrum is low compared to what can be achieved with n-type TCO.

By doping Cu_2O with substitutional cations, we mentioned that it was possible to improve both the optical transparency and the electrical conductivity of this material (Section 1.3.1). Given those benefits, and the fact that the deposition conditions of Cu_2O:Mg are comparable to that of Cu_2O, we chose to use Mg as substitutional dopant.

In this section, we study whether the dynamic spin coating of silver nanowires on a thin film of Cu_2O:Mg works better than on Cu_2O. Firstly, we refer to two authors to justify the choice of the sputtering deposition parameters in order to obtain the best possible film in terms of electrical conductivity and optical transparency. We also detail the annealing process after the dynamic deposition of silver nanowires. Then, we analyze the optical and electrical properties of the Cu_2O:Mg film and the fabricated silver nanowire network. To conclude, we compare these properties to the ones obtained with Cu_2O and glass.

6.2.1 Fabrication of magnesium doped cuprous oxide

Within the SPIN lab, Y. Malier [133] studied the benefits of doping Cu_2O with magnesium. The presence of Mg ions seemed to favor the Cu_2O phase at the expense of the CuO phase, hence the Cu_2O:Mg films appeared more transparent. J. Resende also reported an increase in transmittance upon Mg doping of Cu_2O [4]. The average transmittance in the visible range was 51% and the band gap was 2.4 eV for a doping concentration of 17%, resulting in an increase in band gap of 0.2 eV with respect to the intrinsic/undoped film. Moreover, Cu_2O:Mg films also benefited from a better conductivity. The resistivity dropped from 202 Ωcm to 6.6 Ωcm in the 17% Cu_2O:Mg film. A post-deposition thermal annealing at 250°C allowed to improve the transparency and conductivity even more by increasing the grain size.

T. Ratz [17] analyzed the influence of RF magnetron sputtering parameters on the electrical, optical, and structural properties of Cu_2O:Mg thin films. He found that the lowest resistivity was obtained by keeping the substrate at room temperature, but that the best transmittance was achieved by heating the substrate. Moreover, he noticed an increase in island-shaped structures at the surface of the film with increasing substrate temperature. Using a figure of merit, which balances the optical and electrical properties of the film, he concluded that the best fabrication process was to keep the substrate at room temperature.

Based on these findings and in accordance with the fabrication of undoped cuprous oxide films, we were able to fix the parameters for the RF magnetron sputtering of Cu_2O:Mg on glass. The substrate is kept at room temperature (i.e. 30°C) and the Ar flow rate is set to 20 sccm. The target used for the deposition of Cu_2O:Mg is a Cu_2O target containing 17% per weight of Mg (99.99% purity). The sputtering power, the argon pressure, and the deposition rate are set to 73.5 W, 3 mTorr, and 0.05 nm/s respectively. The target thickness was set to 150 nm and seemed to be the real thickness of the film. Finally, aiming at improving the conductivity of Cu_2O:Mg, the thin film has been annealed at 250°C during 1 hour.

Optical characterization The results of the optical characterization of the Cu_2O:Mg film are reported in Figure 6.3, and compared to the S2 Cu_2O film that we already characterized. We chose to take sample S2 as reference for the Cu_2O films because its thickness (137 nm) is the closest to the thickness of the Cu_2O:Mg film (150 nm). An increase in average transmittance in the visible range is not observed upon doping the Cu_2O film (Figure 6.3a). This is probably because the Cu_2O:Mg film is thicker than the Cu_2O film, resulting in a smaller transmittance according to Beer-Lambert law. Figure 6.3b presents the squared absorption coefficient as a function of the photon energy to determine the band gap by extrapolating the linear region of the curve towards the x-axis intercept. We notice that, as desired, the band gap of Cu_2O:Mg (2.48 eV) is larger than the band gap of intrinsic Cu_2O (2.41 eV). This red shift towards higher energies is in accordance with the transmittance spectrum in Figure 6.3a. When the band gap increases, absorption occurs for photons carrying more energy, hence for photons with a smaller wavelength. This is why, in Figure 6.3a, the transmittance becomes non-zero at higher wavelengths. The Urbach energy fit, displayed in Figure 6.3c, confirms the exponential increase in the absorption coefficient below the band gap energy, indicating the presence of band tails extending in the band gap. These band tails seem to be more pronounced in the Cu_2O:Mg film since the Urbach energy, which can be seen as the characteristic width of the band tails, is 316 meV, while the Urbach energy of the Cu_2O film is 232 meV.

Electrical characterization The electrical characterization of the Cu_2O:Mg film, performed with the Van der Pauw 4-point method, shows that, compared to the S2 Cu_2O film, the resistivity has been divided by two (Table 6.6). This decrease in resistivity is owed to a larger concentration of charge carriers upon doping, and an increase in grain size upon post-deposition thermal annealing. The decrease in mobility due to the increased charge carrier concentration is then partly compensated by the reduced grain boundary scattering.

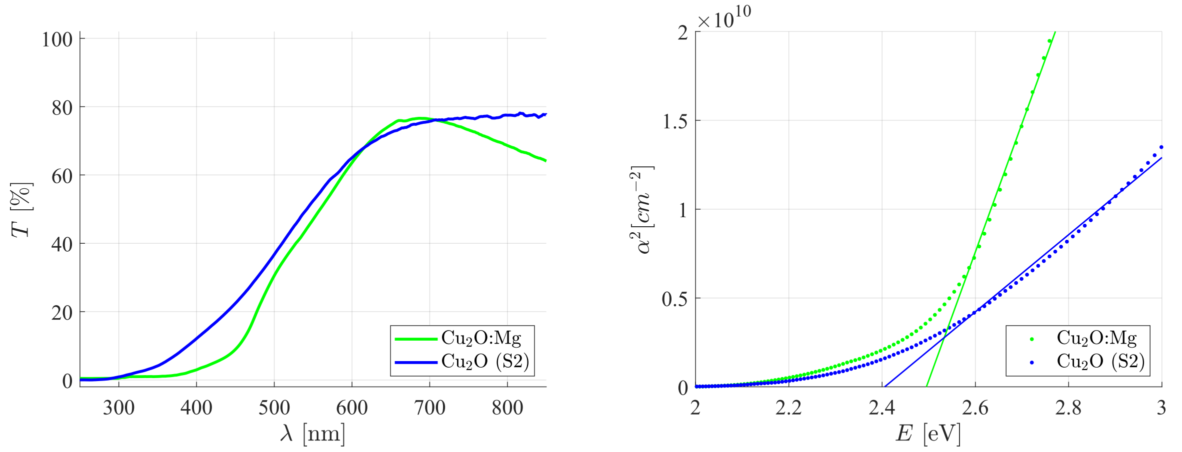

(a) Transmittance (b) Absorption coefficient

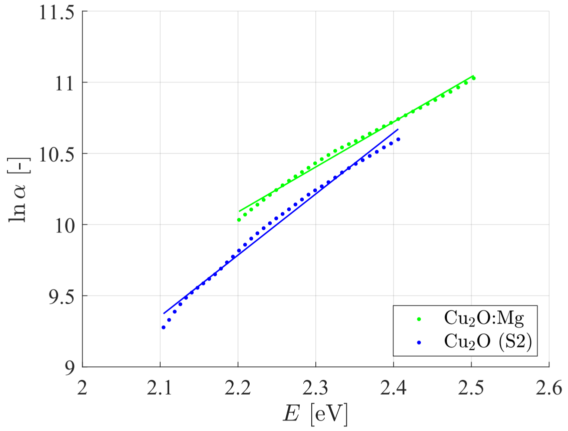

(c) Urbach energy fit

Figure 6.12: Transmittance, absorption coefficient, and Urbach energy fit of a virgin Cu_2O:Mg sample and a virgin Cu_2O sample. By performing a linear regression in (b), we find that the band gap of the Cu_2O:Mg thin film is 2.48 eV. The band gap of the Cu_2O film (S2) was 2.41 eV. Similarly, by performing a linear regression in (c) and taking the inverse of the slope, we find that the Urbach energy of the Cu_2O:Mg sample is 316 meV. The Urbach energy of the Cu_2O sample (S2) was 232 meV.

Sample	**Resistivity**	**Sheet resistance**
Cu_2O:Mg	64.5 Ω.cm	0.94 MΩ
Cu_2O	143 Ω.cm	3.5 MΩ

Table 6.6: Electrical characterization of the Cu_2O:Mg film compared to Cu_2O.

6.2.2 Deposition and annealing of silver nanowires on Cu_2O:Mg

To be consistent with the above experiments, spin coating of the silver nanowires on Cu_2O:Mg is also performed using the dynamic deposition method. Again, 6×5 drops, with a waiting time of 30 seconds between each series of drops, are deposited while the substrate is rotating continuously. Then, to increase the conductivity of the silver nanowire network, the sample has been annealed at 80°C during 3 min, and subjected to a thermal ramp of 15.5°C/min until 250°C, where the temperature has been kept constant for 10 min (Figure 6.13). By contrast to what we observed for the nanowires deposited on Cu_2O, we did not notice any color change of the Cu_2O:Mg thin film. The film presented a yellowish color before and after annealing. The reason is that magnesium doping delays the phase transition from Cu_2O to CuO. According to Resende et al. [134], the oxidation of Cu_2O into CuO in Cu_2O:Mg films occurs at a higher temperature when compared with undoped Cu_2O. The increased stability of Cu_2O:Mg can be explained by the inhibition of the formation of split copper vacancies, which favors CuO nucleation.

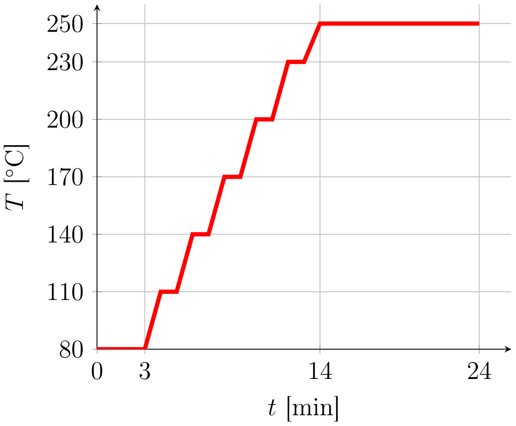

Figure 6.13: Annealing process for the silver nanowires deposited on Cu_2O:Mg.

6.2.3 Optical and electrical characterization

The optical characterization of the Cu_2O:Mg film covered by silver nanowires, shown in Figure 6.14, is very promising. The average decrease in transmittance between 400 nm and 800 nm is only 4.37%, while the decrease in transmittance was 13.6% for silver nanowires deposited on glass, and 28.67% for silver nanowires deposited on Cu_2O (Table 6.7). The main advantage of Cu_2O:Mg is that the film does not darken when the nanowires are annealed, since the transformation of the yellowish Cu_2O into the brown CuO is delayed upon magnesium doping. The reason why the percentage decrease in transmittance between the virgin sample and the sample covered by silver nanowires is lower on Cu_2O:Mg than on glass is probably that the density of the network is smaller. This should be confirmed by SEM images.

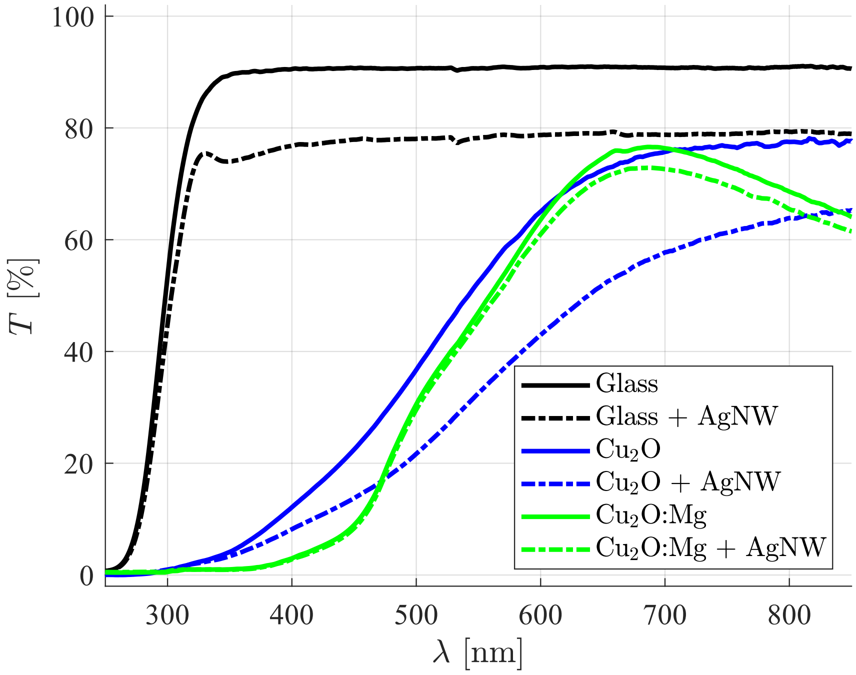

Figure 6.14: Transmittance of silver nanowire networks deposited on Cu_2O:Mg in comparison to glass and Cu_2O. All networks have been obtained by a dynamic deposition of 6 × 5 drops and annealing at 250°C.

Sample	**Virgin [%]**	**With AgNW [%]**	**Decrease [%]**
Glass	90.64	78.34	13.6
Cu_2O	55.81	39.71	28.67
Cu_2O:Mg	51.24	49.00	4.37

Table 6.7: Transmittance of silver nanowire networks deposited on glass, Cu_2O, and Cu_2O:Mg. The transmittance is taken on average between 400 nm and 800 nm. The fabrication method for all substrates is a dynamic deposition of 6 × 5 drops and a thermal annealing at 250°C.

Sample	**Substrate sheet resistance**	**AgNW resistance**
Glass	Overload	42 Ω
Cu_2O	3.5 MΩ	24 kΩ
Cu_2O:Mg	0.94 MΩ	77 Ω

Table 6.8: Electrical characterization of AgNW deposited on Cu_2O:Mg compared to Cu_2O and glass. The fabrication method for all substrates is a dynamic deposition of 6 × 5 drops and a thermal annealing at 250°C.

A two point electrical measurement between two sides of the sample covered by silver paste showed that the electrical resistance of the network was 77 Ω. This value is of the same order of magnitude as the one obtained for nanowires deposited on glass. The drop in resistance is remarkable when comparing the resistance of the silver nanowires fabricated on Cu_2O:Mg and on Cu_2O (Table 6.8). The Cu_2O:Mg substrate, which is more conductive than Cu_2O or glass, may contribute to an enhanced conductivity of the network. However, if the sheet resistance of the Cu_2O:Mg layer is much larger than the resistance of the network, virtually all the current goes through the network. This can be demonstrated by modeling the sample with a simplified electrical circuit. If R_1 denotes the resistance of the silver nanowire network and R_2 represents the resistance of the Cu_2O:Mg film, the equivalent resistance R of both resistances in parallel is given by:

$$\begin{aligned} \frac{1}{R} &= \frac{1}{R_1} + \frac{1}{R_2} \\ \Longleftrightarrow R &= \frac{R_1\,R_2}{R_1 + R_2} = \frac{R_1}{1 + \frac{R_1}{R_2}}. \end{aligned} \tag{6.9}$$

If $R_1 \ll R_2$, we can define the small number $\varepsilon = R_1/R_2 \ll 1$, such that a Maclaurin series development yields:

$$R = \frac{R_1}{1 + \varepsilon} \simeq R_1(1 - \varepsilon) \simeq R_1. \tag{6.10}$$

According to the AgNW resistance and the Cu_2O:Mg sheet resistance mentioned in Table 6.8, we have $R_1 \simeq 100\,\Omega$ and $R_2 \simeq 10^6\,\Omega$, such that $\varepsilon \simeq 10^{-4} \ll 1$. The equivalent resistance of the circuit is thus in good approximation equal to the resistance of the silver nanowire network. In conclusion, almost all the current flows through the silver nanowire network, so that 77 Ω is truly the resistance of the network and not a combination of the network and the Cu_2O:Mg film.

Without SEM images of the networks deposited on Cu_2O:Mg it is difficult to explain the good conductivity of the network. The main hypothesis is that doping the Cu_2O film with magnesium reduces its hydrophobic character, allowing a more uniform distribution of nanowires and a better adhesion to the substrate. Finally, according to the optical and electrical results, the network density should be smaller than for glass, but still large enough to be above the percolation threshold.

6.2.4 Conclusion and remarks

Doping the Cu_2O film with Mg^{2+} cations and performing a post-deposition thermal annealing allows to increase the band gap, the transmittance in the visible range, and the conductivity of the thin film, with respect to undoped Cu_2O films. While the band gap is enlarged by local distortion of the lattice upon doping, the transmittance is improved by preventing the appearance of the dark color CuO phase. The conductivity is enhanced by increasing the hole concentration upon Mg doping and by increasing the mobility of the charge carriers thanks to a larger grain size upon thermal annealing. The electrical and optical properties of the sputtered Cu_2O:Mg film, presenting a resistivity of 64.5 Ωcm, a band gap of 2.48 eV, and a peak transmittance at 77%, shows comparative performances to a Cu_2O:Mg film obtained by CVD and exhibiting a resistivity of 6.6 Ωcm, a band gap of 2.4 eV, and a peak transmittance of 70% [4].

Optical and electrical results demonstrated a promising combination between the Cu_2O:Mg film and the network of silver nanowires. The average transmittance in the visible range of the Cu_2O:Mg film is quite low (51.24%), but has been weakly affected by the deposition of the silver nanowires. The resistance of the network fabricated on Cu_2O:Mg (77 Ω) is similar to the one obtained for nanowires deposited on glass (on average 42 Ω for the dynamic deposition of 6 × 5 drops). This good conductivity and transparency may be attributed to a lower network density, still above the percolation threshold, a decreased hydrophobicity compared to Cu_2O, and an intimate contact between the nanowires and the Cu_2O:Mg film.

Conclusion and future work

The challenge in developing transparent optoelectronic devices is that a compromise must be made between optical transparency and electrical conductivity. Silver nanowire networks demonstrated their potential to replace the widely used but expensive and rare material ITO as transparent electrode. However, many efforts are still needed to better control and/or optimize their fabrication method and implementation on various substrates. P-type Cu_2O showed to be a promising material to the development of transparent optoelectronic components based on pn-junctions. Its conductivity has be enhanced upon magnesium doping and thermal annealing, but a significant increase in band gap, hence transparency, seemed to be more complicated to achieve. Other copper-based oxides with a larger band gap, like $CuCrO_2$, should be studied to investigate whether the transparency of the p-type layer can be increased, without impeding on the electrical resistivity.

The fabrication of oxide pn-junctions can be achieved using two different architectures: the p and n layers can be interchanged. The choice for the order of the pn-layers depends on the fabrication method, i.e. the temperature at which the layers are deposited. As illustrated in the introduction (Figure 2), the Cu_2O layer can be deposited on top of the ZnO layer, but the reverse stacking is also possible. Therefore, besides investigating the interdependence of silver nanowires on Cu_2O, the interaction between silver nanowires and ZnO should also be considered.

For nanowires with a fixed size, we were able to fabricate a network with a silver nanowire network density close to the network density maximizing Haacke's figure of merit. This allowed use to obtain a good compromise between optical transparency and electrical conductivity and to achieve a Haacke's figure of merit comparable to the one obtained by spray coating. A plot of the sheet resistance, transmittance, and Haacke's figure of merit even shows that our networks are able to compete with ITO, FTO, and AZO transparent electrodes. The data points shown in Figure 6.15 are a summary of the scientific articles cited in this work. In comparison to TCO, silver nanowire networks can be integrated in flexible devices and deposited using low-cost, solution-based, methods.

We concluded that a dynamic deposition technique offered the best results in terms of uniformity, nanowire network density, and adherence between the nanowires and the glass substrate. However, as-deposited networks led to samples with high resistances due to organic residues trapped between nanowires.

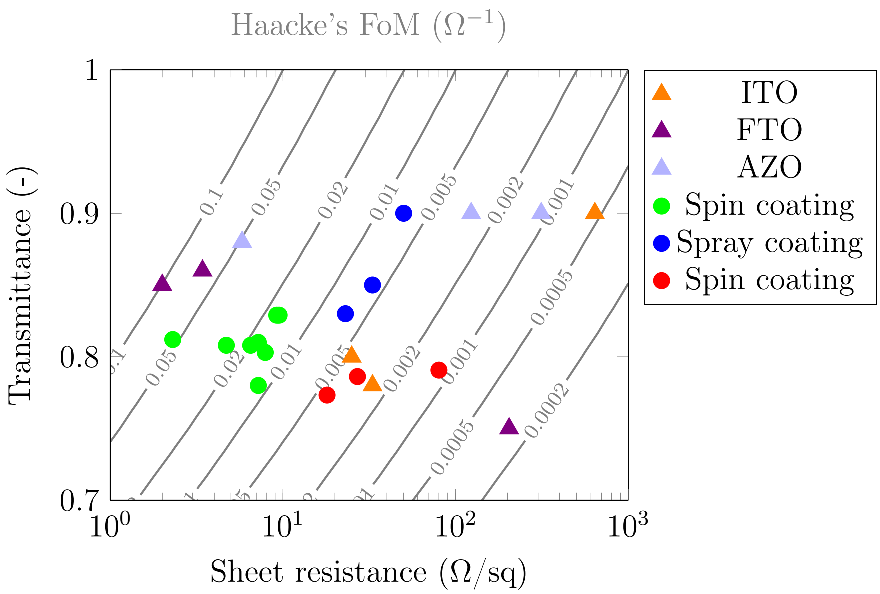

Figure 6.15: Plot of the sheet resistance, transmittance, and Haacke's figure of merit for different types of transparent electrodes. The circular dots correspond to AgNW networks, while the triangles are associated to TCO. A more detailed distinction between various fabrication methods is done based on different colors. The red dots are the experimental values obtained in this work by dynamic spin coating and thermal annealing.

A fast, cheap, and easy method to solve this problem was to perform a thermal annealing. This process allowed a thermal desorption of isopropanol/PVP and junction welding, reducing the junction resistance between overlapping nanowires. The optimization of the spin coating and thermal annealing processes made it possible to achieve a transparent AgNW electrode exhibiting an optical transmittance of 77% and an electrical resistance of 18 Ω.

Among various PVD thin film deposition methods, we found that RF magnetron sputtering was the best suited method to obtain high quality Cu_2O films. The chosen sputtering parameters rendered films with an electrical resistivity down to 143 Ωcm and an average transmittance in the visible range up to 58%. Nevertheless, to be integrated in transparent optoelectronic devices, the electrical conductivity and optical transmittance of the active layers should be as high as possible. Therefore, we doped the Cu_2O film with Mg^{2+} cations and exposed the sputtered film to a thermal annealing process. This allowed to decrease the electrical resistivity by rising the concentration of holes. Unfortunately, the slight widening of the band gap (2.41 eV for Cu_2O and 2.48 eV for Cu_2O:Mg) did not improve the average transmittance in the visible range.

The low conductivity of silver nanowires networks spin coated on Cu_2O proves that further studies should be conducted on the interdependence between the AgNW electrode and the underlying layer. By contrast, the deposition of silver nanowires on Cu_2O:Mg offered a network resistance of 77 Ω, comparable to the one obtained on glass. We suggest that the wetting properties (hydrophilicity/hydrophobicity) influence the adhesion between the nanowires and the substrate. This topic is extremely challenging since the surface tension and contact angle of a liquid depend on the chemical composition, surface roughness, surface defects, and porosity of the substrate.

For hydrophobic substrates, a plasma treatment, laser texturing, or a different type of solvent could be used to increase the wettability of the surface [135]. The development of transferable silver nanowire networks, embedded in a thin PDMS or colorless polyimide layer, is another solution to transfer the network onto hydrophobic and/or flexible substrates [136], [137].

Another struggling point is related to the post-deposition thermal annealing of the silver nanowire network. This process is imperative to decrease the junction resistance between nanowires, hence the global resistance of the network. Problems arise when the substrate is sensitive to heating. This is for example the case for polymer substrates, like PET, but also for Cu_2O which changes color when it is annealed at 250°C. The darkening of the thin film is probably linked to a phase change of Cu_2O into CuO. Moreover, the thermal load that can be applied to the silver nanowire network is dictated by the diameter of the nanowires. We encountered stability problems because the post-deposition thermal treatment was optimized for nanowires with a diameter of 200 nm, while the polyol solution contained a non-negligible nanowire diameter distribution. We noticed the thermal decomposition of nanowires with a diameter smaller than 100 nm. Instabilities also start at structural defects where the nanowires are locally thinner. The type of substrate and its roughness may influence the threshold before the instability occurs. The problem is that the spheroidization of the nanowires leads to a loss of conductivity at high temperatures.

Future work should focus on the thermal and mechanical stability of silver nanowire networks. Thermal annealing parameters, like temperature and duration, must be carefully adapted to optimize the networks without degrading them. To circumvent thermal instabilities, non-thermal nanowire network treatments should be developed. Some alternatives, like plasma treatment, already showed promising results [79]. Another way to improve the thermal stability of nanowires is to form a nanocomposite by embedding the nanowires in a transparent conductive oxide [112]. Encapsulating nanowires in a transparent conductive oxide or polymer should also improve the adhesion and mechanical stability of the network, creating opportunities for their application as transparent flexible electrode. Moreover, this process would also reduce surface roughness together with the possibility of short circuits in device integration.

Although this study only dealt with the fabrication of the networks, other phenomena must be taken into account in real devices under electrical bias. Like the spheroidization temperature, the maximum current density that a metallic nanowire can be subjected to before failure depends on its diameter [43]. Since the electrical resistivity of a nanowire is inversely proportional to its diameter, local heating due to the Joule effect will be larger in thinner nanowires. Finally, efficient AgNW fabrication methods with reproducible properties at industrial scales and rates should also be developed, since spin coating is not scalable. While silver exhibits the highest bulk electrical conductivity among all metals, it may be replaced by less expensive materials like copper. Nevertheless, growth and stability of copper nanowires appear more problematic at present.

In conclusion, we showed that is was possible to fabricate transparent and conductive silver nanowire networks. The integration of this type of electrode on top of wide band gap semiconducting junctions should be further explored, as the nature of the underlying layer impinges on its performances.

Bibliography

[1] A. Glass, *Smart windows*, 2020. [Online]. Available: `https://www.agc-glass.eu/en/products/functions-glass` (visited on 04/30/2020).

[2] Z. Ma and D. Liu, *Inorganic Flexible Optoelectronics: Materials and Applications.* Wiley, 2019.

[3] H. Ohta and H. Hosono, "Transparent oxide optoelectronics," *Materials Today*, vol. 7, no. 6, pp. 42–51, 2004.

[4] J. Resende, C. Jiménez, N. D. Nguyen, and J. Deschanvres, "Magnesium-doped cuprous oxide (Mg:Cu2O) thin films as a transparent p-type semiconductor," *physica status solidi (a)*, vol. 213, no. 9, pp. 2296–2302, 2016.

[5] L.-C. Chen, C.-C. Wang, and S.-W. Lu, "Annealing Effects of Sputtered Cu2O Nanocolumns on ZnO-Coated Glass Substrate for Solar Cell Applications," *Journal of Nanomaterials*, vol. 2013, pp. 1–6, 2013.

[6] R. A. Serway and J. W. Jewett, *Physics for Scientists and Engineers with Modern Physics*, C. Learning, Ed. 2013.

[7] V. H. Nguyen, U. Gottlieb, A. Valla, D. Muñoz, D. Bellet, and D. Muñoz-Rojas, "Electron tunneling through grain boundaries in transparent conductive oxides and implications for electrical conductivity: the case of ZnO:Al thin films," *Materials Horizons*, vol. 5, no. 4, pp. 715–726, 2018.

[8] N. D. Nguyen, *Lectures on Physics of Semiconductors*, Université de Liège, 2020.

[9] B. Streetman and S. Banerjee, *Solid State Electronic Devices.* Pearson, 2015.

[10] J. I. Pankove, *Optical Processes in Semiconductors.* Dover Publications, Inc., 2010.

[11] J. Werner and M. Peisl, "Exponential band tails in polycrystalline semiconductor films," vol. 31, no. 10, 1985.

[12] V. R. Akshay, B. Arun, G. Mandal, and M. Vasundhara, "Visible range optical absorption, Urbach energy estimation and paramagnetic response in Cr-doped TiO2 nanocrystals derived by a sol-gel method.," *Physical chemistry chemical physics : PCCP*, vol. 21, no. 24, pp. 12 991–13 004, 2019.

[13] K. Ellmer, "Past achievements and future challenges in the development of optically transparent electrodes," *Nature Photonics*, vol. 6, no. 12, pp. 809–817, 2012.

[14] G. Haacke, "New figure of merit for transparent conductors," *Journal of Applied Physics*, vol. 47, no. 9, pp. 4086–4089, 1976.

[15] V. K. Jain and A. P. Kulshreshtha, "Indium-Tin-Oxide transparent conducting coatings on silicon solar cells and their "figure of merit"," *Solar Energy Materials*, vol. 4, no. 2, pp. 151–158, 1981.

[16] T. M. Barnes, M. O. Reese, J. D. Bergeson, B. A. Larsen, J. L. Blackburn, M. C. Beard, J. Bult, and J. v. d. Lagemaat, "Comparing the Fundamental Physics and Device Performance of Transparent, Conductive Nanostructured Networks with Conventional Transparent Conducting Oxides," *Advanced Energy Materials*, vol. 2, no. 3, pp. 353–360, 2012.

[17] T. Ratz, "Electrical and optical characterization of AZO/Cu2O:Mg transparent semiconducting heterojunctions grown by RF magnetron sputtering," Master's thesis, Université de Liège, 2018.

[18] J.-Y. Noh, H. Kim, H.-H. Nahm, Y.-S. Kim, D. H. Kim, B.-D. Ahn, J.-H. Lim, G. H. Kim, J.-H. Lee, and J. Song, "Cation composition effects on electronic structures of In-Sn-Zn-O amorphous semiconductors," *Journal of Applied Physics*, vol. 113, no. 18, p. 183 706, 2013.

[19] G. Hautier, A. Miglio, D. Waroquiers, G.-M. Rignanese, and X. Gonze, "How Does Chemistry Influence Electron Effective Mass in Oxides? A High-Throughput Computational Analysis," *Chemistry of Materials*, vol. 26, no. 19, pp. 5447–5458, 2014.

[20] S. C. Dixon, D. O. Scanlon, C. J. Carmalt, and I. P. Parkin, "n-Type doped transparent conducting binary oxides: an overview," *Journal of Materials Chemistry C*, vol. 4, no. 29, pp. 6946–6961, 2016.

[21] K. Kardarian, D. Nunes, P. M. Sberna, A. Ginsburg, D. A. Keller, J. V. Pinto, J. Deuermeier, A. Y. Anderson, A. Zaban, R. Martins, and E. Fortunato, "Effect of Mg doping on Cu 2 O thin films and their behavior on the TiO 2 /Cu 2 O heterojunction solar cells," *Solar Energy Materials and Solar Cells*, vol. 147, pp. 27–36, 2016.

[22] L. Y. Isseroff and E. A. Carter, "Electronic Structure of Pure and Doped Cuprous Oxide with Copper Vacancies: Suppression of Trap States," *Chemistry of Materials*, vol. 25, no. 3, pp. 253–265, 2013.

[23] M. Nolan and S. D. Elliott, "Tuning the Transparency of Cu2O with Substitutional Cation Doping," *Chemistry of Materials*, vol. 20, no. 17, pp. 5522–5531, 2008.

[24] R. G. Gordon, "Criteria for Choosing Transparent Conductors," *MRS Bulletin*, vol. 25, no. 8, pp. 52–57, 2000.

[25] J. Jimenez and J. W. Tomm, *Spectroscopic Analysis of Optoelectronic Semiconductors*. Springer, 2016.

[26] G. Rey, "Etude d'oxydes métalliques nanostructurés (ZnO, SnO2) pour applications photovoltaïques notamment oxydes transparents conducteurs et cellules solaires à coloran," PhD thesis, 2012.

[27] N. P. Armitage, "Electrodynamics of correlated electron systems," *arXiv*, 2009.

[28] O. Bierwagen, "Indium oxide—a transparent, wide-band gap semiconductor for (opto)electronic applications," *Semiconductor Science and Technology*, vol. 30, no. 2, p. 024 001, 2015.

[29] A. M. Ganose and D. O. Scanlon, “Band gap and work function tailoring of SnO 2 for improved transparent conducting ability in photovoltaics,” *Journal of Materials Chemistry C*, vol. 4, no. 7, pp. 1467–1475, 2016.

[30] A. Sharmin, S. Tabassum, M. S. Bashar, and Z. H. Mahmood, “Depositions and characterization of sol–gel processed Al-doped ZnO (AZO) as transparent conducting oxide (TCO) for solar cell application,” *Journal of Theoretical and Applied Physics*, vol. 13, no. 2, pp. 123–132, 2019.

[31] A. I. Hofmann, E. Cloutet, and G. Hadziioannou, “Materials for Transparent Electrodes: From Metal Oxides to Organic Alternatives,” *Advanced Electronic Materials*, vol. 4, no. 10, p. 1 700 412, 2018.

[32] D. S. Ginley and D. C. Paine, *Handbook of Transparent Conductors*. Springer, 2010.

[33] U. Betz, M. K. Olsson, J. Marthy, M. Escolá, and F. Atamny, “Thin films engineering of indium tin oxide: Large area flat panel displays application,” *Surface and Coatings Technology*, vol. 200, no. 20-21, pp. 5751–5759, 2006.

[34] D. S. Bhachu, M. R. Waugh, K. Zeissler, W. R. Branford, and I. P. Parkin, “Textured Fluorine-Doped Tin Dioxide Films formed by Chemical Vapour Deposition,” *Chemistry - A European Journal*, vol. 17, no. 41, pp. 11 613–11 621, 2011.

[35] H. Agura, A. Suzuki, T. Matsushita, T. Aoki, and M. Okuda, “Low resistivity transparent conducting Al-doped ZnO films prepared by pulsed laser deposition,” *Thin Solid Films*, vol. 445, no. 2, pp. 263–267, 2003.

[36] T. Minami, H. Nanto, and S. Takata, “Highly Conductive and Transparent Aluminum Doped Zinc Oxide Thin Films Prepared by RF Magnetron Sputtering,” *Japanese Journal of Applied Physics*, vol. 23, no. 1, pp. L280–L282, 1984.

[37] A. Axelevitch, B. Gorenstein, and G. Golan, “Investigation of Optical Transmission in Thin Metal Films,” *Physics Procedia*, vol. 32, pp. 1–13, 2012.

[38] Y. Liu, C.-F. Guo, S. Huang, T. Sun, Y. Wang, and Z. Ren, “A new method for fabricating ultrathin metal films as scratch-resistant flexible transparent electrodes,” *Journal of Materiomics*, vol. 1, no. 1, pp. 52–59, 2015.

[39] M. Barati and E. Sadeghi, “Study of the ordinary size effect in the electrical conductivity of Bi nanowires,” *Nanotechnology*, vol. 12, p. 277, 2001.

[40] F. Lacy, “Developing a theoretical relationship between electrical resistivity, temperature, and film thickness for conductors,” *Nanoscale Research Letters*, vol. 6, no. 636, 2011.

[41] D. Gall, “Electron mean free path in elemental metals,” *Journal of Applied Physics*, vol. 119, no. 8, p. 085 101, 2016.

[42] M. Lagrange, D. P. Langley, G. Giusti, C. Jiménez, Y. Bréchet, and D. Bellet, “Optimization of silver nanowire-based transparent electrodes: effects of density, size and thermal annealing,” *Nanoscale*, vol. 7, no. 41, pp. 17 410–23, 2015.

[43] D. Bellet, M. Lagrange, T. Sannicolo, S. Aghazadehchors, V. Nguyen, D. Langley, D. Muñoz-Rojas, C. Jiménez, Y. Bréchet, and N. Nguyen, “Transparent Electrodes Based on Silver Nanowire Networks: From Physical Considerations towards Device Integration,” *Materials*, vol. 10, no. 6, p. 570, 2017.

[44] Y.-J. Noh, S.-S. Kim, T.-W. Kim, and S.-I. Na, “Cost-effective ITO-free organic solar cells with silver nanowire–PEDOT:PSS composite electrodes via a one-step spray deposition method,” *Solar Energy Materials and Solar Cells*, vol. 120, pp. 226–230, 2014.

[45] D. Angmo, T. R. Andersen, J. J. Bentzen, M. Helgesen, R. R. Søndergaard, M. Jørgensen, J. E. Carlé, E. Bundgaard, and F. C. Krebs, “Roll-to-Roll Printed Silver Nanowire Semitransparent Electrodes for Fully Ambient Solution-Processed Tandem Polymer Solar Cells,” *Advanced Functional Materials*, vol. 25, no. 28, pp. 4539–4547, 2015.

[46] J.-W. Lim, D.-Y. Cho, K. Eun, S.-H. Choa, S.-I. Na, J. Kim, and H.-K. Kim, “Mechanical integrity of flexible Ag nanowire network electrodes coated on colorless PI substrates for flexible organic solar cells,” *Solar Energy Materials and Solar Cells*, vol. 105, pp. 69–76, 2012.

[47] C. Preston, Y. Xu, X. Han, J. N. Munday, and L. Hu, “Optical haze of transparent and conductive silver nanowire films,” *Nano Research*, vol. 6, no. 7, pp. 461–468, 2013.

[48] Z. Yu, Q. Zhang, L. Li, Q. Chen, X. Niu, J. Liu, and Q. Pei, “Highly Flexible Silver Nanowire Electrodes for Shape-Memory Polymer Light-Emitting Diodes,” *Advanced Materials*, vol. 23, no. 5, pp. 664–668, 2010.

[49] W. Gaynor, S. Hofmann, M. G. Christoforo, C. Sachse, S. Mehra, A. Salleo, M. D. McGehee, M. C. Gather, B. Lüssem, L. Müller-Meskamp, P. Peumans, and K. Leo, “Color in the Corners: ITO-Free White OLEDs with Angular Color Stability,” *Advanced Materials*, vol. 25, no. 29, pp. 4006–4013, 2013.

[50] K.-H. Ok, J. Kim, S.-R. Park, Y. Kim, C.-J. Lee, S.-J. Hong, M.-G. Kwak, N. Kim, C. J. Han, and J.-W. Kim, “Ultra-thin and smooth transparent electrode for flexible and leakage-free organic light-emitting diodes,” *Scientific Reports*, vol. 5, no. 1, p. 9464, 2015.

[51] G.-J. Jeong, J.-H. Lee, S.-H. Han, W.-Y. Jin, J.-W. Kang, and S.-N. Lee, “Silver nanowires for transparent conductive electrode to GaN-based light-emitting diodes,” *Applied Physics Letters*, vol. 106, no. 3, p. 031 118, 2015.

[52] T. Sannicolo, M. Lagrange, A. Cabos, C. Celle, J. Simonato, and D. Bellet, “Metallic Nanowire-Based Transparent Electrodes for Next Generation Flexible Devices: a Review,” *Small*, vol. 12, no. 44, pp. 6052–6075, 2016.

[53] T. Kim, Y. W. Kim, H. S. Lee, H. Kim, W. S. Yang, and K. S. Suh, “Uniformly Interconnected Silver-Nanowire Networks for Transparent Film Heaters,” *Advanced Functional Materials*, vol. 23, no. 10, pp. 1250–1255, 2012.

[54] R. Gupta, K. D. M. Rao, S. Kiruthika, and G. U. Kulkarni, “Visibly Transparent Heaters,” *ACS Applied Materials & Interfaces*, vol. 8, no. 20, pp. 12 559–12 575, 2016.

[55] S. Hong, H. Lee, J. Lee, J. Kwon, S. Han, Y. D. Suh, H. Cho, J. Shin, J. Yeo, and S. H. Ko, “Highly Stretchable and Transparent Metal Nanowire Heater for Wearable Electronics Applications,” *Advanced Materials*, vol. 27, no. 32, pp. 4744–4751, 2015.

[56] X. He, A. Liu, X. Hu, M. Song, F. Duan, Q. Lan, J. Xiao, J. Liu, M. Zhang, Y. Chen, and Q. Zeng, “Temperature-controlled transparent-film heater based on silver nanowire–PMMA composite film,” *Nanotechnology*, vol. 27, no. 47, p. 475 709, 2016.

[57] J. Park, D. Han, S. Choi, Y. Kim, and J. Kwak, “Flexible transparent film heaters using a ternary composite of silver nanowire, conducting polymer, and conductive oxide,” *RSC Advances*, vol. 9, no. 10, pp. 5731–5737, 2019.

[58] C. Lee, Y. Oh, I. S. Yoon, S. H. Kim, B.-K. Ju, and J.-M. Hong, “Flash-induced nanowelding of silver nanowire networks for transparent stretchable electrochromic devices,” *Scientific Reports*, vol. 8, no. 1, p. 2763, 2018.

[59] H. H. Khaligh, K. Liew, Y. Han, N. M. Abukhdeir, and I. A. Goldthorpe, “Silver nanowire transparent electrodes for liquid crystal-based smart windows,” *Solar Energy Materials and Solar Cells*, vol. 132, pp. 337–341, 2015.

[60] S. Fahad, H. Yu, L. Wang, Zain-ul-Abdin, M. Haroon, R. S. Ullah, A. Nazir, K.-R. Naveed, T. Elshaarani, and A. Khan, “Recent progress in the synthesis of silver nanowires and their role as conducting materials,” *Journal of Materials Science*, vol. 54, no. 2, pp. 997–1035, 2018.

[61] Y. Shi, L. He, Q. Deng, Q. Liu, L. Li, W. Wang, Z. Xin, and R. Liu, “Synthesis and Applications of Silver Nanowires for Transparent Conductive Films,” *Micromachines*, vol. 10, no. 5, p. 330, 2019.

[62] P. Zhang, I. Wyman, J. Hu, S. Lin, Z. Zhong, Y. Tu, Z. Huang, and Y. Wei, “Silver nanowires: Synthesis technologies, growth mechanism and multifunctional applications,” *Materials Science and Engineering: B*, vol. 223, pp. 1–23, 2017.

[63] A. Nekahi, S. Marashi, and D. H. Fatmesari, “High yield polyol synthesis of round- and sharp-end silver nanowires with high aspect ratio,” *Materials Chemistry and Physics*, vol. 184, pp. 130–137, 2016.

[64] Y. Gao, P. Jiang, D. Liu, H. Yuan, X. Yan, Z. Zhou, J. Wang, L. Song, L. Liu, W. Zhou, G. Wang, C. Wang, and S. Xie, “Synthesis, characterization and self-assembly of silver nanowires,” *Chemical Physics Letters*, vol. 380, pp. 146–149, 2003.

[65] N. Sahu, B. Parija, and S. Panigrahi, “Fundamental understanding and modeling of spin coating process: A review,” *Indian Journal of Physics*, vol. 83, no. 4, pp. 493–502, 2009.

[66] N. Vandewalle, *Lectures on Statistical Physics*, Université de Liège, 2018.

[67] K. Christensen, *Percolation Theory*, Imperial College London, 2002.

[68] T. Gebele, “Site percolation threshold for square lattice,” *Journal of Physics A: Mathematical and General*, vol. 17, no. 2, pp. L51–L54, 1984.

[69] D. Langley, “Silver nanowires networks : Effects of percolation and thermal annealing on physical properties,” PhD thesis, 2015.

[70] J. Li and S.-L. Zhang, “Finite-size scaling in stick percolation,” *Physical Review E*, vol. 80, no. 4, p. 40 104, 2009.

[71] G. Kaur, R. Adhikari, P. Cass, M. Bown, and P. Gunatillake, “Electrically conductive polymers and composites for biomedical applications,” *RSC Advances*, vol. 5, no. 47, pp. 37 553–37 567, 2015.

[72] S. De and J. N. Coleman, “The effects of percolation in nanostructured transparent conductors,” *MRS Bulletin*, vol. 36, no. 10, pp. 774–781, 2011.

[73] S. M. Bergin, Y.-H. Chen, A. R. Rathmell, P. Charbonneau, Z.-Y. Li, and B. J. Wiley, “The effect of nanowire length and diameter on the properties of transparent, conducting nanowire films,” *Nanoscale*, vol. 4, no. 6, pp. 1996–2004, 2012.

[74] A. Bid, A. Bora, and A. K. Raychaudhuri, “Temperature dependence of the resistance of metallic nanowires: Applicability of Bloch-Gruneisen theorem,” *Physical Review B*, vol. 74, no. 3, p. 35 426, 2006.

[75] L. J. Andrés, M. F. Menéndez, D. Gómez, A. L. Martínez, N. Bristow, J. P. Kettle, A. Menéndez, and B. Ruiz, “Rapid synthesis of ultra-long silver nanowires for tailor-made transparent conductive electrodes: proof of concept in organic solar cells,” *Nanotechnology*, vol. 26, no. 26, p. 265 201, 2015.

[76] H. Yang, T. Chen, H. Wang, S. Bai, and X. Guo, “One-pot rapid synthesis of high aspect ratio silver nanowires for transparent conductive electrodes,” *Materials Research Bulletin*, vol. 102, pp. 79–85, 2018.

[77] D. P. Langley, M. Lagrange, G. Giusti, C. Jiménez, Y. Bréchet, N. D. Nguyen, and D. Bellet, “Metallic nanowire networks: effects of thermal annealing on electrical resistance,” *Nanoscale*, vol. 6, no. 22, pp. 13 535–13 543, 2014.

[78] R. Zhang and M. Engholm, “Recent Progress on the Fabrication and Properties of Silver Nanowire-Based Transparent Electrodes.,” *Nanomaterials (Basel, Switzerland)*, vol. 8, no. 8, p. 628, 2018.

[79] J. Li, Y. Tao, S. Chen, H. Li, P. Chen, M.-z. Wei, H. Wang, K. Li, M. Mazzeo, and Y. Duan, “A flexible plasma-treated silver-nanowire electrode for organic light-emitting devices,” *Scientific Reports*, vol. 7, no. 1, p. 16 468, 2017.

[80] K. Zhang, J. Li, Y. Fang, B. Luo, Y. Zhang, Y. Li, J. Zhou, and B. Hu, “Unraveling the solvent induced welding of silver nanowires for high performance flexible transparent electrodes,” *Nanoscale*, vol. 10, no. 27, pp. 12 981–12 990, 2018.

[81] L. Hu, H. S. Kim, J.-Y. Lee, P. Peumans, and Y. Cui, “Scalable Coating and Properties of Transparent, Flexible, Silver Nanowire Electrodes,” *ACS Nano*, vol. 4, no. 5, pp. 2955–2963, 2010.

[82] S. Shengbo, L. Lihua, J. Aoqun, D. Qianqian, J. Jianlong, Z. Qiang, and Z. Wendong, “Highly sensitive wearable strain sensor based on silver nanowires and nanoparticles,” *Nanotechnology*, vol. 29, no. 25, p. 255 202, 2018.

[83] C. Gommes, *Lectures on Physical Chemistry of Interfaces*, Université de Liège, 2019.

[84] T. K. S. Wong, S. Zhuk, S. Masudy-Panah, and G. K. Dalapati, “Current Status and Future Prospects of Copper Oxide Heterojunction Solar Cells,” *Materials*, vol. 9, no. 4, p. 271, 2016.

[85] A. H. Shukor, H. A. Alhattab, and I. Takano, “Electrical and optical properties of copper oxide thin films prepared by DC magnetron sputtering,” *Journal of Vacuum Science and Technology B*, vol. 38, no. 1, p. 012 803, 2020.

[86] J. Pan, C. Yang, and Y. Gao, “Investigations of Cuprous Oxide and Cupric Oxide Thin Films by Controlling the Deposition Atmosphere in the Reactive Sputtering Method,” *Sensors and Materials*, vol. 28, no. 7, 2016.

[87] W. Andrew, *Handbook of Sputtering Technology.* Elsevier Inc., 2012.

[88] A. R. Barron, *Chemistry of Electronic Materials.* Connexions, 2011.

[89] M. Ohring, *Materials Science of Thin Films.* Academic Press, 2002.

[90] P. Vanderbemden, *Lectures on Sensors, Microsensors and Instrumentation*, Université de Liège, 2020.

[91] A. Engineering, *Electron Beam Evaporation.* [Online]. Available: `https://angstromengineering` `com/tech/electron-beam-evaporation/` (visited on 09/26/2019).

[92] G. Luo, X. Cheng, Z. He, H. Wu, and Y. Cao, “High-performance inverted polymer solar cells based on thin copper film,” *Journal of Photonics for Energy*, vol. 5, no. 1, p. 057 206, 2014.

[93] H. Lüth, “Solid Surfaces, Interfaces and Thin Films,” 2015.

[94] D. L. Smith, *Thin-Film Deposition: Principles and Practice.* McGraw-Hill, 1995.

[95] N. D. Nguyen, *Lectures on Nanofabrication: Principles and Techniques*, Université de Liège, 2020.

[96] A. Engineering, *Magnetron Sputtering Overview.* [Online]. Available: `https://angstromengineering.com/tech/magnetron-sputtering/` (visited on 09/26/2019).

[97] Č. I. Belić, K. Đ. Stanković, M. M. Pejović, and P. V. Osmokrović, “The Influence of the Magnetic Field on DC and the Impulse Breakdown of Noble Gases,” *Materials*, vol. 12, no. 5, p. 752, 2019.

[98] A. S. Reddy, P. S. Reddy, S. Uthanna, G. V. Rao, and A. Klein, “Effect of substrate temperature on the physical properties of dc magnetron sputtered Cu2O films,” *physica status solidi (a)*, vol. 203, no. 5, pp. 844–853, 2006.

[99] L. Whenhao, “Synthesis of cuprous oxide thin films by rf-magnetron sputtering,” *Surface Review and Letters*, vol. 25, no. 02, p. 1 850 051, 2018.

[100] S. Ishizuka and Akimoto, Takahiro Maruyama and Katsuhiro, “Thin-Film Deposition of Cu2O by Reactive Radio-Frequency Magnetron Sputtering,” *The Japan Society of Applied Physics*, vol. 39, 2000.

[101] A. S. Reddy, H.-H. Park, V. S. Reddy, K. Reddy, N. Sarma, S. Kaleemulla, S. Uthanna, and P. S. Reddy, “Effect of sputtering power on the physical properties of dc magnetron sputtered copper oxide thin films,” *Materials Chemistry and Physics*, vol. 110, no. 2-3, pp. 397–401, 2008.

[102] A. S. Reddy, S. Uthanna, and P. S. Reddy, “Properties of dc magnetron sputtered Cu2O films prepared at different sputtering pressures,” *Applied Surface Science*, vol. 253, no. 12, pp. 5287–5292, 2007.

[103] H.-C. Lu, C.-L. Chu, C.-Y. Lai, and Y.-H. Wang, “Property variations of direct-current reactive magnetron sputtered copper oxide thin films deposited at different oxygen partial pressures,” *Thin Solid Films*, vol. 517, no. 15, pp. 4408–4412, 2009.

[104] Y. Liu, J. Zhang, W. Zhang, W. Liang, B. Yu, and J. Xue, “Effects of annealing temperature on the properties of copper films prepared by magnetron sputtering,” *Journal of Wuhan University of Technology-Mater. Sci. Ed.*, vol. 30, no. 1, pp. 92–96, 2015.

[105] B. J. Inkson, “Materials Characterization Using Nondestructive Evaluation (NDE) Methods,” pp. 17–43, 2016.

[106] R. Nanofabrication, *Pioneer Two.* [Online]. Available: `https://www.raith.com/files/PDF%5C%20Downloads/brochure-pioneer-two.pdf` (visited on 05/28/2020).

[107] W. C. H. Kuo, M. Briceno, and D. Ozkaya, “Final Analysis: Characterisation of Catalysts Using Secondary and Backscattered Electron In-lens Detectors,” *Platinum Metals Review*, vol. 58, no. 2, pp. 106–110, 2014.

[108] I. Miccoli, F. Edler, H. Pfnür, and C. Tegenkamp, “The 100th Anniversary of the Four-point Probe Technique: the Role of Probe Geometries in Isotropic and Anisotropic Systems,” *Journal of Physics: Condensed Matter*, 2015. [Online]. Available: `https://iopscience.iop.org/article/10.1088/0953-8984/27/22/223201/pdf`.

[109] L. J. V. d. Pauw, “A Method of Measuring the Resistivity and Hall Coefficient on Lamellae of Arbitrary Shape,” *Philips Technical Review*, 1958.

[110] ——, “A Method of Measuring Specific Resistivity and Hall Effect of Discs of Arbitrary Shape,” *Philips Research Reports*, 1958.

[111] PhysTech, “Hall Measurement System RH 2010,” [Online]. Available: `http://www.phystech.de/products/hall/hlappli.pdf` (visited on 10/17/2019).

[112] V. H. Nguyen, J. Resende, D. T. Papanastasiou, N. Fontanals, C. Jiménez, D. Muñoz-Rojas, and D. Bellet, “Low-cost fabrication of flexible transparent electrodes based on Al doped ZnO and silver nanowire nanocomposites: impact of the network density,” *Nanoscale*, vol. 11, no. 25, 2019.

[113] A. R. Madaria, A. Kumar, and C. Zhou, “Large scale, highly conductive and patterned transparent films of silver nanowires on arbitrary substrates and their application in touch screens,” *Nanotechnology*, vol. 22, no. 24, p. 245 201, 2011.

[114] Shimadzu, *UV-3600: Shimadzu UV-VIS-NIR Spectrophotometer.* [Online]. Available: `https://www.upc.edu/sct/documents%5C_equipament/d%5C_85%5C_id-406.pdf` (visited on 11/14/2019).

[115] T. Owen, *Fundamentals of UV-visible spectroscopy.* 2000.

[116] E. Ikeda, “Integrating Spheres,” *UV Talk Letter*, vol. 5, pp. 2–4, 2010.

[117] T. Hiramatsu, “How to Choose Integrating Spheres and White Reference Plates,” *UV Talk Letter*, vol. 12, pp. 8–11, 2013.

[118] M. Lagrange, “Physical analysis of percolating silver nanowire networks used as transparent electrodes for flexible applications,” PhD thesis, 2015.

[119] V. Froidart, “Fabrication of a transparent conducting material using metallic nanostructures,” Université de Liège, Tech. Rep., 2019.

[120] *VWR ultrasound cleaning machines.* [Online]. Available: `https://hiltoninstruments.com/uploads/pdfs/USC%5C_ultrasonic%5C_baths.pdf` (visited on 03/19/2020).

[121] *WS-650-23 Laurell Spin Coater.* [Online]. Available: `http://www.laurell.com/spin-coater/?model=WS-650-23` (visited on 03/19/2020).

[122] *UniTemp HPP-155 Hot plate.* [Online]. Available: `https://unitemp.de/EN/hot-plates/hp-series/hpp-155/?id=46` (visited on 03/22/2020).

[123] *Spin Coating Theory*, 2013. [Online]. Available: `https://louisville.edu/micronano/files/documents/standard-operating-procedures/SpinCoatingInfo.pdf` (visited on 11/25/2019).

[124] D. P. Langley, G. Giusti, M. Lagrange, R. Collins, C. Jiménez, Y. Bréchet, and D. Bellet, “Silver nanowire networks: Physical properties and potential integration in solar cells,” *Solar Energy Materials and Solar Cells*, vol. 125, pp. 318–324, 2014.

[125] V. Scardaci, R. Coull, P. E. Lyons, D. Rickard, and J. N. Coleman, “Spray deposition of highly transparent, low-resistance networks of silver nanowires over large areas.,” *Small (Weinheim an der Bergstrasse, Germany)*, vol. 7, no. 18, pp. 2621–8, 2011.

[126] A. Engineering, *Nexdep physical vapor deposition platform.* [Online]. Available: `https://angstromengineering.com/products/nexdep/` (visited on 05/26/2020).

[127] C. Malerba, F. Biccari, C. L. A. Ricardo, M. D’Incau, P. Scardi, and A. Mittiga, “Absorption coefficient of bulk and thin film Cu2O,” *Solar Energy Materials and Solar Cells*, vol. 95, no. 10, pp. 2848–2854, 2011.

[128] FormFactor, *Cascade MPS150 150 mm Manual Probe System.* [Online]. Available: `https://www.formfactor.com/download/mps150-data-sheet/` (visited on 10/19/2019).

[129] PhysTech, *Hall Measurement System RH 2035.* [Online]. Available: `http://www.phystech.de/products/hall/hl2035.pdf` (visited on 10/17/2019).

[130] G. Zhou, L. Luo, L. Li, J. Ciston, E. A. Stach, W. A. Saidi, and J. C. Yang, “In situ atomic-scale visualization of oxide islanding during oxidation of Cu surfaces,” *Chemical Communications*, vol. 49, no. 92, pp. 10 862–10 864, 2013.

[131] A. Ogwu, E. Bouquerel, O. Ademosu, S. Moh, E. Crossan, and F. Placido, “An investigation of the surface energy and optical transmittance of copper oxide thin films prepared by reactive magnetron sputtering,” *Acta Materialia*, vol. 53, no. 19, pp. 5151–5159, 2005.

[132] W. Zheng, Y. Chen, X. Peng, K. Zhong, Y. Lin, and Z. Huang, “The Phase Evolution and Physical Properties of Binary Copper Oxide Thin Films Prepared by Reactive Magnetron Sputtering,” *Materials*, vol. 11, no. 7, p. 1253, 2018.

[133] Y. Malier, “Radio-frequency magnetron deposition of transparent conducting thin films based on ZnO and Cu2O for photovoltaic applications,” Master’s thesis, Université de Liège, 2017.

[134] J. Resende, O. Chaix-Pluchery, M. Rovezzi, Y. Malier, H. Renevier, N. D. Nguyen, J.-L. Deschanvres, and C. Jiménez, “Resilience of Cuprous Oxide under Oxidizing Thermal Treatments via Magnesium Doping,” *The Journal of Physical Chemistry C*, vol. 123, no. 14, pp. 8663–8670, 2019.

[135] A. Popelka, I. Krupa, I. Novák, M. A. S. A. Al-Maadeed, and M. Ouederni, “Improvement of aluminum/polyethylene adhesion through corona discharge,” *Journal of Physics D: Applied Physics*, vol. 50, no. 3, p. 035 204, 2016.

[136] S. Zhu, Y. Gao, B. Hu, J. Li, J. Su, Z. Fan, and J. Zhou, “Transferable self-welding silver nanowire network as high performance transparent flexible electrode,” *Nanotechnology*, vol. 24, no. 33, p. 335 202, 2013.

[137] D.-G. Kim, J. Kim, S.-B. Jung, Y.-S. Kim, and J.-W. Kim, "Electrically and mechanically enhanced Ag nanowires-colorless polyimide composite electrode for flexible capacitive sensor," *Applied Surface Science*, vol. 380, pp. 223–228, 2016.